Scale-resolving simulations of internal combustion engine flows

Skalenauflösende Simulation innermotorischer Strömungen
Zur Erlangung des akademischen Grades Doktor-Ingenieur (Dr.-Ing.)
genehmigte Dissertation von M.Sc. Stefan Buhl aus Marktredwitz
Tag der Einreichung: 27.03.2018, Tag der Prüfung: 13.06.2018
Darmstadt — D 17

1. Gutachten: Prof. Dr.-Ing. Christian Hasse
2. Gutachten: Prof. Dr. rer. nat. habil Andreas Dreizler

TECHNISCHE
UNIVERSITÄT
DARMSTADT

Fachbereich Maschinenbau
Simulation reaktiver Thermo-Fluid
Systeme

Scale-resolving simulations of internal combustion engine flows
Skalenauflösende Simulation innermotorischer Strömungen

Genehmigte Dissertation von M.Sc. Stefan Buhl aus Marktredwitz

1. Gutachten: Prof. Dr.-Ing. Christian Hasse
2. Gutachten: Prof. Dr. rer. nat. habil Andreas Dreizler

Tag der Einreichung: 27.03.2018
Tag der Prüfung: 13.06.2018

Darmstadt, Technische Universität Darmstadt
Jahr der Veröffentlichung der Dissertation auf TUprints: 2018

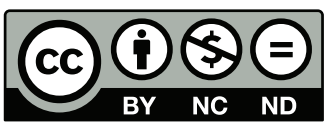

Erklärung zur Dissertation

Hiermit versichere ich, die vorliegende Dissertation ohne Hilfe Dritter nur mit den angegebenen Quellen und Hilfsmitteln angefertigt zu haben. Alle Stellen, die aus Quellen entnommen wurden, sind als solche kenntlich gemacht. Diese Arbeit hat in gleicher oder ähnlicher Form noch keiner Prüfungsbehörde vorgelegen.

Darmstadt, den 18.03.2018

(M.Sc. Stefan Buhl)

Danksagung

Die vorliegende Arbeit ist überwiegend während meiner Zeit als wissenschaftlicher Mitarbeiter am Institut für Energieverfahrenstechnik und Chemieingenieurwesen an der Professur für Numerische Thermofluiddynamik entstanden.
Mein besonderer Dank gilt hierbei meinem Doktorvater Prof. Dr.-Ing. Christian Hasse, der mir die Möglichkeit gegeben hat, mich ausgiebig mit der numerischen Untersuchung von Verbrennungskraftmaschinen zu beschäftigen. Die anregenden und konstruktiven Diskussionen mit ihm sowie seine fortlaufende und geduldige Unterstützung zur Förderung meiner Entwicklung (persönlich und fachlich) haben ein Gelingen dieser Arbeit überhaupt erst ermöglicht. Ich möchte mich an dieser Stelle auch noch einmal ausdrücklich für die Freiheiten bei der Entwicklung der Arbeitsinhalte und das entgegengebrachte Vertrauen bedanken.

Weiterhin möchte ich mich bei all meinen ehemaligen Kollegen für die gute Zusammenarbeit bedanken, welche mir die Arbeit in vielen Bereichen verschönert, erleichtert und ermöglicht hat. Namentlich erwähnen möchte ich Dr.-Ing. Danny Messig und Dr.-Ing. Sandra Hartl, welche mich bei mathematischen Fragen immer hervorragend unterstützt haben. Im Bereich der IT konnten Axel Zschutschke und Dr.-Ing. Felix Dietzsch immer eine Lösung für meine teils sehr komplexen Probleme finden. Florian Gleiß und Dominik Hain unterstützten mich bei den routinemäßigen Arbeitsabläufen und hatten außerdem immer ein offenes Ohr, wenn es um motorische oder „tool-spezifische" Fragestellungen ging.

Mein herausragender Dank gilt meinem früheren Kollegen, „Motorenmitstreiter" und Freund Frank Hartmann. Ich möchte ganz ausdrücklich erwähnen, dass mir deine tatkräftige Unterstützung bei der Bewältigung von diversen Industrieprojekten erst den notwendigen Freiraum gegeben hat, mich auf die eigentliche Forschungsarbeit zu konzentrieren. Die mit dir geführten Gespräche auf persönlicher und fachlicher Ebene waren enorm wichtig und haben massiv zum Gelingen der Arbeit beigetragen.

Weiterhin möchte ich mich bei Mario Köhler, Dr.-Ing. Martin Schild, Prof. Dr. Sebastian Kaiser, Carl-Philipp Ding und Dr.-Ing. Benjamin Böhm für die Bereitstellung der experimentellen Daten und die anregenden Diskussionen bei der Interpretation der Ergebnisse bedanken. An dieser Stelle möchte ich auch meinen Dank gegenüber Dr.-Ing. Wolfgang Bauer und Dr.-Ing. Martin Kuntz ausdrücken, welche mir bei Problemen mit dem CFD-Löser tatkräftig zur Seite standen.

Abschließend bedanke ich mich bei meiner Frau Claudia Buhl. Ohne dich wäre an einen erfolgreichen Abschluss dieser Arbeit überhaupt nicht zu denken gewesen. Aufgrund deiner hervorragenden fachlichen Kompetenzen hast du mir wertvolle Anregungen und Impulse bei herausfordernden Programmieraufgaben geben können. Viel wichtiger noch ist, dass du mich während der ganzen Zeit am Lehrstuhl und darüber hinaus mental unterstützt hast. Du hast es geschafft, mich auch in besonders schwierigen Phasen wieder aufzubauen und zu motivieren. Claudia, vielen Dank für alles!

Abstract

This thesis presents a numerical study of turbulent flows in internal combustion engines (ICEs) with focus on selected modeling and physical aspects. All studies base on a substantial number of consecutive cycles (up to 100) generated for simplified as well as state-of-the-art engine setups. Throughout the work, the results are compared and validated to existing experimental data and results obtained by direct numerical simulation (DNS). One major aspect is to study cycle-to-cycle variations (CCVs).

Appropriate modeling strategies for ICEs are intensively discussed. One example is the most suitable treatment of the intake and the exhaust ports. Here, three different port modeling strategies are applied on a well-known experimental engine setup. Integral quantities are evaluated and the velocity components as well as their fluctuations are compared to existing experimental data.

Furthermore, the accuracy of selected scale-resolving turbulence models and their capability to capture large-scale and small-scale fluctuations are analyzed. For this, three LES models (Smagorinsky, WALE and Sigma), one hybrid model (DES-SST) and one second-generation URANS model (SAS-SST) are applied to a simplified engine setup. The predicted averaged velocities and the resolved fluctuations are compared to each other and to reference data from DNS and experiment. The investigated key aspect is the models' capability to resolve CCVs.

A quasi steady state flow bench configuration is used to analyze the effect of the applied turbulence model and the numerical grid on the flow in the vicinity of the intake valve. For a detailed investigation with regard to the intake jet, the velocity field is transformed into a local jet-adapted coordinate system. Based on this transformation, three characteristic zones within the intake jet are identified.

A simplified engine setup is used to quantify the cyclic variability of large-scale structures within the combustion chamber in a next step. For that purpose, a novel ad-hoc methodology is presented. This methodology (combining proper orthogonal decomposition and conditional averaging) groups the instantaneous flow fields into different subsets and allows a quantification of a large and a small-scale contribution to the total fluctuations.

The generation of the large-scale tumble structure and its interaction to the piston boundary layer during the intake stroke is studied based on an experimental gasoline engine setup with a state-of-the-art cylinder head. The instantaneous and phase-averaged tumble structures within the 3D flow field are visualized. Based on specific values of the dimensionless wall normal distance, the thickness of the piston boundary layer is computed and its interaction with the large-scale tumble structure is studied.

Finally, the tumble development during the compression stroke is considered based on two established experimental engine setups, for which benchmark data was made available. After a general evaluation of the phase-averaged and instantaneous tumble structures, the CCV is quantified. To quantify the kinetic energy stored by the in-cylinder charged motion, the phase-averaged tumble intensity is evaluated. The tumble development during the compression stroke is subdivided into four consecutive phases.

In summary, this thesis offers a significant advance in the evaluation of several modeling strategies. Furthermore, it contributes to a deeper understanding of the in-cylinder flow processes, especially during the intake and compression stroke.

Kurzfassung

Die vorliegende Arbeit präsentiert eine numerische Untersuchung von Strömungen in Verbrennungsmotoren. Der Fokus liegt auf ausgewählten modellierungsspezifischen und physikalischen Aspekten. Als Grundlage dienen sowohl vereinfachte als auch moderne seriennahe Motorkonfigurationen. Die erzeugten Simulationsergebnisse werden mit verschiedenen Referenzergebnissen (Experiment und direkte numerische Simulation) verglichen. Im Rahmen der Arbeit werden ausschließlich skalenauflösende Turbulenzmodelle verwendet, um auch durch zyklische Schwankungen hervorgerufene Effekte zu berücksichtigen.

Ein kritischer und häufig diskutierter Punkt bei der Berechnung von Verbrennungsmotoren stellen die verschiedenen zum Einsatz kommenden Modellierungsansätze dar. Im ersten Schritt wird basierend auf einem experimentellen Versuchsmotor die Handhabung des Rechengebietes analysiert. Dabei kommen drei verschiedene Ansätze zur Behandlung des Ein- bzw. des Auslasskanals zum Einsatz. Die Bewertung erfolgt mittels integraler Größen, Geschwindigkeitskomponenten und deren Fluktuationen. Die so gewonnenen Ergebnisse werden untereinander und mit experimentellen Daten verglichen.
Weiterhin wird auf Basis einer vereinfachten Motorkonfiguration die Genauigkeit ausgewählter Turbulenzmodelle sowie deren Fähigkeit, zyklische, groß- und kleinskalige Schwankungen korrekt wiederzugeben, untersucht. Hier kommen drei LES-Modelle (Smagorinsky, WALE und Sigma), ein hybrides Modell (DES-SST) und ein URANS-Modell der zweiten Generation (SAS-SST) zum Einsatz.

Mit Hilfe eines quasi-stationären Strömungsprüfstandes wird die Sensitivität des Rechenergebnisses hinsichtlich des zum Einsatz kommenden Turbulenzmodells und Rechengitters betrachtet. Der Fokus der Auswertung liegt dabei auf dem Einlassjet in unmittelbarer Nähe zum Einlassventils. Zur weiterführenden Analyse wird das Geschwindigkeitsfeld mittels eines lokal an den Einlassjet angepassten Koordinatensystems transformiert und in drei charakteristische Zonen unterteilt.
Anhand einer vereinfachten Motorkonfiguration werden die zyklischen Schwankungen innerhalb des Brennraums analysiert. Mittels einer neu entwickelten Methode werden die instantanen Geschwindigkeitsfelder in verschiedene Gruppen eingeteilt. Diese Gruppierung geschieht durch eine kombinierte Anwendung der „proper orthogonal decomposition" und einer „konditionierten Mittelung". Anschließend können die Fluktuationen in einen groß- und einen kleinskaligen Anteil zerlegt werden.
Im weiteren Verlauf der Arbeit wird die Ladungsbewegung innerhalb des Brennraums (Tumble) sowie deren Auswirkung auf die Strömungsgrenzschicht auf dem Kolben untersucht. Die instantanen Tumble und deren Phasenmittel werden innerhalb des 3D-Strömungsfeldes visualisiert. Die Dicke der Kolbengrenzschicht wird (anhand spezifischer Werte des dimensionslosen Wandabstandes) ausgewertet und die Verbindung mit der Tumble-Struktur hergestellt.
Zum Abschluss wird der Tumble während der Kompressionsphase bewertet. Die Basis hierfür bilden zwei hochmoderne experimentelle Versuchsmotoren. Die Bewertung des Tumble erfolgt anhand seiner räumlichen Entwicklung, der auftretenden zyklischen Schwankung und der phasen-gemittelten Tumble-Intensität.

Zusammengefasst stellt diese Arbeit einen wesentlichen Fortschritt bei der Bewertung von verschiedenen Modellierungsstrategien dar. Weiterhin leistet sie einen Beitrag zum verbesserten Verständnis der innermotorischen Strömungsphänomene während der Einlass- und Kompressionsphase.

Contents

List of Figures

List of Tables

Nomenclature

Abbreviations

Symbol	*Meaning*
BDC	Bottom dead center
CA	Crank angle
CBLA	Classical boundary layer assumption
CCV	Cycle-to-cycle variation
CEC	Cause-and-effect chain
CFD	Computational fluid dynamics
CFL	Courant-Friedrichs-Lewy
DES	Detached eddy simulation
DNS	Direct numerical simulation
EU	European union
EVO	Exhaust valve open
fTDC	Top dead center at firing
ICE	Internal combustion engine
IVC	Intake valve closed
LES	Large-eddy simulation
LPP	Long ports permantently
NEDC	New european driving cycle
PANS	Partially-averaged Navier-Stokes
PIV	Particle image velocimetry
POD	Poper orthogonal decomposition
PVC	Precessing vortex core

RANS	Reynolds-averaged Navier-Stokes
RDE	Real driving emissions
rms	Root mean square
ROI	Region of interest
SAS	Scale-adaptive simulation
SC	Sigma model on coarse mesh
SF	Sigma model on fine mesh
SG	Spray-guided engine setup
SM	Sigma model on medium mesh
SPP	Short ports permantently
SPT	Short ports temporally
SRS	Scale-resolving simulation
SST	Shear stress transport
TC	Tumble center
TCC	Transparent combustion chamber
TDC	Top dead center
TI	Tumble intensity
URANS	Unsteady Reynolds-averaged Navier-Stokes
WALE	Wall-adaptive local eddy viscosity
WG	Wall-guided engine setup
WLTP	Worldwide harmonized light duty test procedure

SPECIAL CHARACTERS

Symbol	*Meaning*
$\langle\phi\rangle_{T/P/L/A/V/\vartheta}$	Time-/phase-/trajectory-/area-/volume-averaged quantity

$\overline{\phi}$	Averaged/filtered quantity
$\widetilde{\phi}$	Averaged/filtered and density-weighted quantity

Greek symbols

Symbol	*Meaning*	*Unit*
β^*	Model constant	-
Δ	Filter width	m
Δ_i	Cell size in i-direction	m
κ	Kármán constant	-
λ	Thermal conductivity	$\frac{\mathrm{W}}{\mathrm{K\,m}}$
μ	Dynamic viscosity	$\frac{\mathrm{kg}}{\mathrm{m\,s}}$
μ_t	Turbulent viscosity	$\frac{\mathrm{kg}}{\mathrm{m\,s}}$
Ω	Engine speed	$\frac{1}{\mathrm{s}}$
ω	Turbulent frequency	$\frac{1}{\mathrm{s}}$
Ω_{ij}	Component of rotation tensor	$\frac{1}{\mathrm{s}}$
$\mathbf{\Gamma_{3p}}$, $\mathbf{\Gamma 1_{3p}}$	Vectorial quantity to detect the tumble center	-
$\boldsymbol{\omega}$	Vorticity vector	$\frac{1}{\mathrm{s}}$
ρ	Density	$\frac{\mathrm{kg}}{\mathrm{m}^3}$
σ	Singular value	$\frac{1}{\mathrm{s}}$
τ_{ij}	Component of stress tensor	$\frac{\mathrm{kg}}{\mathrm{m\,s}^2}$
ε	Compression ratio	-
ε	Energy dissipation rate	$\frac{\mathrm{m}^2}{\mathrm{s}^2}$
φ	Crank angle	$^\circ$
Ξ	Conditioning vector	-

LATIN SYMBOLS

Symbol	*Meaning*	*Unit*
$\mathbf{e}$	Unit vector	-
$\mathbf{n}$	Normal vector	-
$\mathbf{r}$	Cylindrical coordinate	m
$\mathbf{u}$	Velocity (vectorial)	$\frac{\mathrm{m}}{\mathrm{s}}$
$\mathbf{x}$	Cartesian coordinate	m
Pr	Prandtl number	-
Re	Reynolds number	-
A	Area	m^2
b	Bore	m
c_p	Heat capacity at constant pressure	$\frac{\mathrm{J}}{\mathrm{kg\,K}}$
$c_{m/1/2}$	Model specific constant	-
d	Distance	m
D_m	Model specific differential operator	$\frac{1}{\mathrm{s}}$
H	Total enthalpy	$\frac{\mathrm{J}}{\mathrm{kg}}$
h	Enthalpy	$\frac{\mathrm{J}}{\mathrm{kg}}$
h	Height	m
k	Turbulent kinetic energy	$\frac{\mathrm{m}^2}{\mathrm{s}^2}$
L	Characteristic length scale	m
m	Mass	kg
p	Pressure	Pa
Q	Invariant of velocity gradient tensor	$\frac{1}{\mathrm{s}^2}$
R	Universal gas constant	$\frac{\mathrm{J}}{\mathrm{mol\,K}}$

$r/x/y/z$	Spatial coordinate	m
R_c	Cylinder radius	m
s	Stroke	m
S_{ij}	Strain rate	$\frac{1}{s}$
T	Temperature	K
t	Time	s
TI	Tumble intesity	-
Tu_i	Integral in-cylinder charge motion around axis i	-
V	(Sub-)volume	m^3
W	Molecular weight	$\frac{kg}{mol}$

SUPERSCRIPTS

Symbol	*Meaning*
†	Coherent structure fluctuations
’	Fluctuations component
*	Dimensionless and locally adapted coordinate
*	Subset specific small-scale fluctuations
+	Dimensionless quantities in context of wall distance
mod	Modeled

SUBSCRIPTS

Symbol	*Meaning*
$\phi_{i/j/k}$	i/j/k-component of vector $\boldsymbol{\phi}$
p	Projected
res	Resolved

t	Turbulent

1 Introduction

Despite the growing trend of electrically driven cars, internal combustion engines (ICEs) will continue to play a leading part in the short, medium and long term future [1–3]. This is particularly true for the transport sector (e.g. heavy commercial vehicles and cargo ships), where no adequate alternative currently exists. Engine manufacturers are faced with contradictory requirements. On the one hand, customers often expect a high-performance powertrain [4] and on the other, the legislature sets more and more stringent requirements in terms of emissions and fuel consumption. On September 1st 2017 the Euro 6c standard came into force within the European Union (EU), which bases for the first time on the Worldwide harmonized Light vehicles Test Procedure (WLTP) [5–7]. Compared to the former test cycle (New European Driving Cycle; NEDC), emissions and energy consumption are measured on an extended range of engine speed and load as well as with a stronger focus on transient phases. The measurement of real driving emissions (or a reduction of the currently applied confirmation factors) in the future leads to a further growth in complexity and therefore to a significantly increased effort in development [8, 9]. Up to 2021, the "average specific emissions of CO2", which serve as a standard for fuel consumption, have to be reduced to $95\,\mathrm{g\,km^{-1}}$ for newly registered cars and light commercial vehicles [10, 11]. A notable reduction can only be achieved by a combination of various measures (e.g. hybridization, lightweight design, synthetic fuels) and by further improved engine technology. For modern spark-ignited ICEs, direct injection, down-sizing and supercharging can be considered as standard. In addition, less widespread approaches (e.g. Miller cycle) became more and more popular in the recent years, even for passenger cars [12]. A highly topical issue in research is the field of heat insulation coatings [13–15], which aims to reduce thermal losses and thus increased efficiency (i.e. reduced fuel consumption). The result of a consistent engine development strategy is presented in [16]. By means of a skillful combination of different individual aspects (e.g. optimized gas exchange and piston contour), a gasoline engine with a compression ratio of $\varepsilon = 14$ and a significantly reduced fuel consumption could be presented.

A strongly limiting element for a further increase in efficiency are the so-called cycle-to-cycle variations (CCVs). Several engine parameters (e.g. spark timing and injected fuel mass) are set with regard to a representative averaged cycle. For example, cyclic variations in flame propagation lead to deviations in terms of the desired center of combustion and therefore to efficiency losses or even to critical operating states (e.g. knock). A fundamental problem of these CCVs is that the complex non-linear cause-and-effect chain (CEC), starting from cyclic variations of the intake flow and finally leading to cyclic variations of the combustion process, is not fully understood. Consequently, it is difficult to apply suitable countermeasures. To enable a basic understanding of this CEC, the engine process is divided into the three consecutive phases *intake flow*, *spray formation and mixing* and *combustion*. Each of these phases is characterized by a variety of individual phenomena. The majority of them are highly sensitive towards initial and boundary conditions. The interaction of these phenomena constitutes a complex system where instabilities are amplified and may evolve in space and time. For that reason, at the same crank angle of consecutive cycles different conditions develop (referred as CCVs). Figure 1.1 schematically illustrates the previously mentioned phenomena which occur within the consecutive phases of a spark-ignited 4-stroke gasoline engine with direct injection.

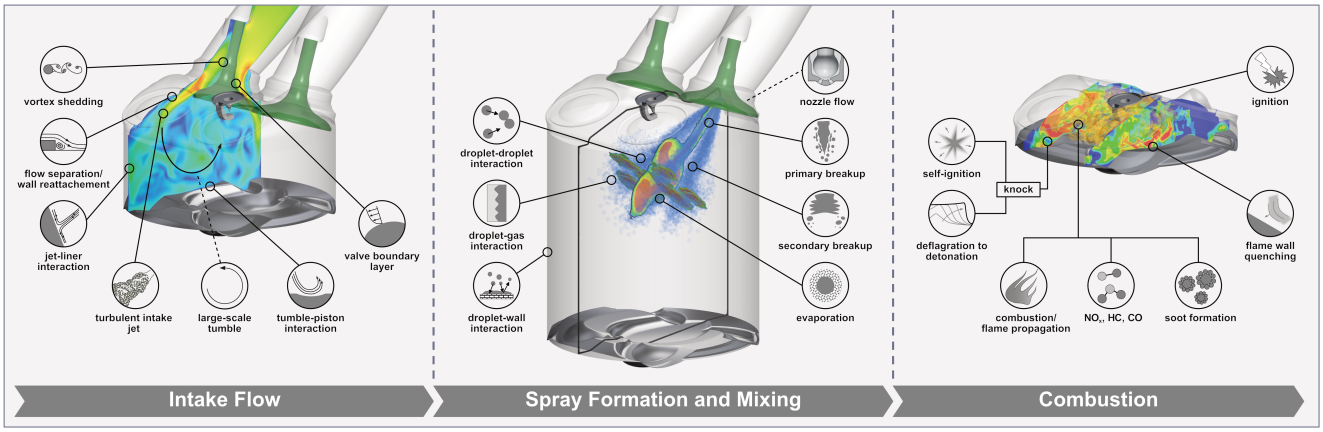

Figure 1.1: The overall engine process is divided into three consecutive phases: intake flow, spray formation and mixing as well as combustion. Within these phases several fundamental phenomena and sub-processes are identified. The progression of each phenomenon/process is highly sensitive towards initial and boundary conditions. The interaction of all processes constitutes a complex system, in which instabilities are amplified and may evolve in space and time (referred as cause-and-effect chain). For that reason, at the same crank angle of successive cycles different (flow) conditions develop. These varying conditions are referred as cycle-to-cycle variations. Picture taken from [17].

During the intake flow, fresh gas enters the combustion chamber, due to the piston motion and the resulting increase of the cylinder volume. Starting at the intake port, the cylindrical valve shaft represents an obstacle where, depending on the actual flow rate, various phenomena can be identified (e.g. vortex shedding, turbulence) [18, 19]. After an acceleration of the fluid caused by the valve gap, a turbulent jet is formed [20–22], while its fundamental position is defined by several factors like the inclination of the intake port/valves as well as the existence and position of machined separation edges. A free turbulent shear layer arises and, with increasing penetration depth, the intake jet is destabilized more and more regarding its position and orientation. Similar to a stagnation point [23–25] the intake jet interacts with the cylinder liner, where it is redirected towards the piston first and along the piston afterwards. The result leads to a large-scale vortical flow structure, the so-called “tumble”, which is an important goal in engine development due to its positive effect on the subsequent fuel-air mixing and combustion. The tumble acts like a storage system for the kinetic energy transported into the combustion chamber during the intake stroke. Ideally, this kinetic energy is released repeatedly and in a well-defined manner shortly before ignition occurs due to the tumble breakdown near to the top dead center at firing (fTDC). The resulting small-scale turbulent fluctuations accelerate the flame front propagation and consequently the combustion process. This helps to increase the efficiency of ICEs. A more detailed overview of the importance of the tumble and its influence on subsequent processes is given in [26, 27]. Another important aspect are the boundary layers [18, 28, 29], which strongly depend on the tumble over wide time periods. It is of particular interest for the entire operating cycle, as the fluid boundary layer is directly coupled to the thermal boundary layer and thus to the heat losses.

In the injection phase, fuel is added to the cylinder charge. The flow within the injector (nozzle flow) is highly complex (key word: cavitation) and investigated by several research teams (e.g. Engine Combustion Network). Starting from the nozzle, the fuel enters the combustion chamber with a high momentum in the form of a liquid jet. Immediately after the entering, it diverges and its surface becomes

unstable, forming ligaments and droplets. This process is typically referred as primary breakup [30–32]. Subsequently, the secondary breakup [30, 33] occurs where the droplets break up into smaller droplets until a critical point is reached (usually determined by the Weber-number). From then on, evaporation is the dominant phenomenon [34, 35]. During the entire period, the droplets interact/collide with the surrounding gas phase, with other ligaments and droplets and with the walls. A profound understanding of these processes is very important for the development of direct-injecting ICEs running in stratified operation conditions, where several development objectives (e.g. minimized engine roughness and pollutant formation) strongly depend on the local fuel-air mixture and the existence of wall films.

In spark-ignited gasoline engines, the combustion process is initiated by an electrical discharge. As a result, a plasma channel occurs, which is strongly deflected and curved by the local flow field. From this plasma channel, radicals and thermal energy are transported into the surrounding fuel-air-mixture and the first self-propagating flame kernels are generated [36, 37]. The propagation speed of this exothermic reaction, the related emissions and the soot formation strongly depend on local conditions like the equivalence ratio, temperature and turbulence intensity [38–40]. Reaching the walls, the reaction zone rapidly cools down and the flame quenches, which can cause problems in terms of pollutant emissions (unburned fuel and carbon monoxide [41–43]). This is especially the case for the piston crevice because of its relatively large volume (depending on the engine design). The ongoing trend of higher specific power densities increases the risk of undesired combustion phenomena, which, in the worst case, can lead to engine damage. One of the most common of these phenomena is knock, which represents a spontaneous ignition of the fuel-air mixture before the arrival of the flame front. These phenomena were intensively investigated in the past [44–46] and still represent a highly topical field of research.

3D computational fluid dynamics (3D-CFD) is a fundamental tool for the investigation of the above described phenomena, their role within the CEC and for preliminary design studies. Considering the industrial engine development process, these topics are frequently done based on unsteady Reynolds-averaged Navier-Stokes (URANS) and other statistical approaches. However, scale-resolving simulations (SRSs), which are well-established in the academic community, are essential for the quantification of CCVs and the detection of sporadically occurring phenomena (e.g. misfire and knock [45, 47]). A recent review of phenomena investigated by means of SRSs is given in [27, 48]. One major drawback of SRSs in ICEs are the computational requirements, which are orders of magnitudes beyond what is needed for URANS [21, 49, 50]. This results from the need of a high spatial and temporal resolution for an individual cycle and the necessity to calculate a statistically relevant number of cycles to obtain meaningful averages. It should be mentioned that the “number of relevant cycles” is currently unknown and still a topic of research. Furthermore, at the moment there is a lack of efficient methods to evaluate a large amount of data which provide a high significance in terms of CCVs of large-scale coherent structures (e.g. the intake jet or the tumble) and therefore new approaches have to be developed. In addition to the previously mentioned issues there are still a number of open questions which have to be answered. These questions concern modeling and physical aspects, such as:

- Where should the boundaries be positioned?
- How to treat the intake and exhaust port while the valves are closed?
- Which turbulence model should be applied?

- How do coherent structure develop during an engine cycle?
- What is the importance of coherent structures with regard to the in-cylinder flow field (e.g. on boundary layers)?
- How to quantify CCVs of coherent structures?

Some of these questions shall be clarified within this thesis.

The first section deals with the treatment of the numerical domain in ICE simulations. For SRSs, the choice of an appropriate numerical domain and the placement of the boundaries is a challenge. On the one side, its spatial extensions have a significant influence on the computational costs and have to be kept as small as possible. On the other, it has to be large enough so that the region of interest is not affected by the modeling approach (e.g. boundary conditions). The literature provides different port modeling strategies for SRSs in ICEs, especially with respect to the extent of the computational domain (boundary close to the flange vs. the entire system up to the plenum) and the numerical treatment of the intake/exhaust when the valves are closed (enabled vs. disabled) [51–60]. To the author's knowledge, there has been no systematic comparative study for these different approaches in the context of ICEs. This work's aim is to identify the requirements for SRSs in terms of the treatment of intake and exhaust ports to obtain accurate statistics (mean and variance) and CCVs.

The next section investigates the suitability of different turbulence models for SRSs at ICE flows, a still unresolved issue in the industrial and academic community. Typically, turbulence models are developed and validated for well-defined generic test cases. It is not clear whether these findings are also valid for flows in complex geometries with spatial and temporal varying Reynolds numbers and moving boundaries, where local flow structures might be significantly different. This is further complicated by flows with several interacting phenomena (see above) which have to be predicted correctly. In previous studies, several turbulence models were applied to engine flows. However, a comparison of these models with regard to ICEs is difficult because of the large number of different engines and numerical approaches [51, 53, 55, 60–68]. The scope of this study is to evaluate different turbulent models in terms of their accuracy and capability to capture fluctuations, local flow structures and CCVs based on a single engine and numerical approach.

Furthermore, the studies are extended by the investigation of physical aspects. In addition to a sensitivity analysis in terms of the numerical mesh, the third section deals with the flow in the vicinity of the intake valve. It constitutes the beginning of the CEC and significantly influences the in-cylinder velocity field. Especially in the upper part of the cylinder a highly complex flow field occurs (indicated in figure 1.1), which results from a multitude of interacting phenomena. The most dominant phenomena are

1) the flow around bluff bodies,

2) turbulent jet,

3) flow separation,

4) wall reattachment and

5) the generation of recirculation zones.

All these phenomena have been analyzed by experiments or direct numerical simulations (DNSs) based on generic test cases. For example, the flow around bluff bodies was considered in [69–71]. Fundamental studies of turbulent jets are presented in [72, 73]. The phenomena **3** to **5** were investigated by means of a backward-facing step [74–76] and a turbulent offset jet [20, 22]. Several studies have shown that SRSs can capture the flow field correctly when only a reduced number of these phenomena in simple geometries are considered [19, 77–80].
Other experimental studies investigated the intake jet within engines on the symmetry plane [81–83]. In [84, 85] magnetic resonance velocimetry was used to analyze the intake flow within the cylinder volume. However, the SRS of a steady-state flow-bench configuration (i.e. intake flow based on non-moving geometry) have revealed noticeable discrepancies between CFD and experimental findings [86]. Due to its importance for the in-cylinder charge motion [51, 87] and the difficulties in terms of simulation, this analysis focuses on the turbulent intake jet. The investigations are done on the valve middle plane of a steady-state flow bench configuration and based on an ad-hoc "streamline method". The aim is to identify the intake jet and its characterization in terms of position, penetration depth and curvature. Furthermore, two turbulence models are compared to one another.

Due to its importance in terms of the engine process, the tumble structure is investigated in the next step. Borée, Maurel, and Bazile [87] analyzed the generation of the tumble using particle image velocimetry (PIV). One of the major findings was the existence of a precessing vortex core (PVC), which was also observed in a numerical study [51]. CCVs in tumble position, intensity and its spatial/temporal breakdown lead to variations in terms of fuel-air mixture and combustion. Considerable research in recent years has focused on a quantification of theses CCVs [81, 88–93]. However, most investigations were limited to a phase-averaged statistical evaluation or to certain in-cylinder planes (i.e. 2D) and there remains a need for an improved understanding of the full 3D tumble structure. This thesis addresses the spatial and temporal development of the tumble structure during the intake stroke and the compression stroke. At first, a heuristic approach is used to identify its CCVs based on the velocity field. The approach presented is a combination of proper orthogonal decomposition (POD) and conditional averaging [87, 94–100] and quantifies the cyclic fluctuations of large-scale (coherent) and smaller structures with respect to an ensemble average. Secondly, the tumble center (TC) position within a 3D flow field of experimental engine setups [82, 101, 102] is investigated. For this purpose, an extension of a previously developed 2D algorithm is used to characterize the phase-averaged tumble structure in terms of its position, its intensity and the CCVs. Subsequently, the tumble breakdown is considered, which is a highly topical issue. For example, Janas [103] introduced a modified version of the two-point correlation for an estimation. In this study, the tumble breakdown is analyzed based on integral quantities (i.e. volume averaged tumble intensity and turbulent kinetic energy).

Additionally, the piston boundary layer during the intake stroke is analyzed. From a simulation perspective, two approaches have to be distinguished.

- *Wall-resolved boundary layer:* Turbulence has to be fully resolved. Near wall turbulence length scales are of the same order of magnitude as the thickness of the viscous sublayer which depends on the Reynolds number.

- *Wall-modeled boundary layer:* Modeling approaches are applied to avoid the necessity to resolve all turbulent scales. These modeling approaches are frequently derived from classical boundary layer assumptions (CBLA).

Typically, the boundary layers have to be fully resolved in classical large eddy simulations (LESs) of wall-bounded flows. Although, a highly accurate prediction of the boundary layer is achieved, LESs are difficult to apply (even in academic investigations) because of their high computational requirements [21, 49, 50]. This is particularly true for most of application-oriented research (as is the case for IC engine flows) where flows with moderate or high Reynolds numbers are considered. The frequently used wall-modeled approach offers a resource-conserving alternative [18, 104–106]. However, previous investigations have shown that the CBLA typically does not describe the real flow structure in ICEs [107, 108]. These findings are of high practical relevance since the wall resolution is usually not sufficient in URANS and SRSs, and thus, new wall models have to be developed [109]. This work aims to provide additional information about the complex flow structure close to the piston surface within the combustion chamber. The piston boundary layer is investigated in terms of its velocity profile, its thickness and how it is influenced by the tumble motion during the final phase of the intake stroke.

Table 1.1 gives an overview of the considered experimental engines setups, a selection of corresponding publications and the investigations based on it.

Table 1.1: Considered engines and investigations done

Section	Experimental research center	References (selection)	Addressed topics (in this work)
3.1 4.4	TU Darmstadt	[82, 102, 110, 111]	Numerical domain (port treatment) Tumble development (during compression)
3.2 4.2	Imperial College London	[68, 112, 113]	Choice of turbulence model Quantification of CCVs
4.1	University Duisburg-Essen	[86]	Mesh sensitivity analysis Investigation of intake jet
4.3	TU Bergakademie Freiberg	[101]	Tumble generation (during intake stroke) Tumble-piston interaction

2 Numerical and modeling approach

This section gives an overview about the most important modeling approaches applied in this work. To do so, the governing equations and the applied turbulence models are presented as a first step. Afterwards, the CFD solver and the principle methodology utilized for ICE simulations are briefly discussed. Finally, the terminology in terms of averaging used is clarified.

2.1 Governing equations

The section gives a short overview of the governing equations for fully compressible and turbulent flows (as applied in section 3.1), solved by ANSYS CFX. Please note that the formalism in the following is limited to those of an eddy viscosity model, which is applied throughout this thesis. A more general and detailed description can be found in [21, 49, 114]. The transport equations for mass, momentum and energy are defined as

$$\frac{\partial \overline{\rho}}{\partial t} + \frac{\partial (\overline{\rho}\widetilde{u}_i)}{\partial x_i} = 0\,, \tag{2.1}$$

$$\frac{\partial (\overline{\rho}\widetilde{u}_j)}{\partial t} + \frac{\partial (\overline{\rho}\widetilde{u}_i\widetilde{u}_j)}{\partial x_i} = -\frac{\partial \overline{p}_m}{\partial x_j} + \frac{\partial}{\partial x_j}\Bigg[\underbrace{(\mu+\mu_t)\left(\frac{\partial \widetilde{u}_i}{\partial x_j} + \frac{\partial \widetilde{u}_j}{\partial x_i}\right)}_{\tau_{ij}+\tau_{ij}^{mod}}\Bigg] \qquad \text{and} \tag{2.2}$$

$$\frac{\partial (\overline{\rho}\widetilde{H})}{\partial t} + \frac{\partial (\overline{\rho}\widetilde{u}_j\widetilde{H})}{\partial x_j} = \frac{\partial \overline{p}_m}{\partial t} + \frac{\partial}{\partial x_j}\left(\lambda\frac{\partial \widetilde{T}}{\partial x_j} + \frac{\mu_t}{Pr_t}\frac{\partial \widetilde{h}}{\partial x_j}\right) + \frac{\partial}{\partial x_j}\left[\widetilde{u}_i\left(\tau_{ij}+\tau_{ij}^{mod}\right)\right], \tag{2.3}$$

where $\widetilde{\phi}$ represents the density-weighted quantity. It is defined as

$$\widetilde{\phi} = \frac{\overline{\rho\phi}}{\overline{\rho}}\,. \tag{2.4}$$

$\overline{\phi}$ denotes, depending on the specific modeling approach (LES or URANS), an either filtered or averaged variable μ, λ and Pr_t represent the dynamic viscosity, the thermal conductivity and the turbulent Prandtl number ($Pr_t = 0.9$). p_m and μ_t denotes a modified pressure (includes the isotropic part of turbulent fluctuations) and the eddy viscosity, while the latter requires modeling (see section 2.2). The quantity $\widetilde{H}$, defined as

$$\widetilde{H} = \widetilde{h} + \frac{1}{2}\widetilde{u}_j\widetilde{u}_j + 0.5\widetilde{u'_j u'_j}\,, \tag{2.5}$$

describes the total enthalpy. This system is complemented by the equation of state for perfect gases, which is defined as

$$\overline{p} = \overline{\rho}\frac{R}{W}\widetilde{T}\,, \tag{2.6}$$

with the molecular weight W and the universal gas constant R.

Please note that for the remaining sections an incompressible approach is applied. This leads to a simplified system of equations (e.g. no Favre filtering and no energy equation), which is not further described for the sake of brevity.

2.2 Turbulence models

In this work, several modeling approaches for SRSs are analyzed. These approaches can be divided into three groups. The first is the group of large eddy simulations (LESs), which base on the filtered form of equations (2.1) to (2.6). Here, the eddy viscosity is defined as

$$\mu_t = \overline{\rho}(c_m \Delta)^2 D_m \,, \tag{2.7}$$

with the model-specific constant c_m. The presented results are based on a non-dynamic formulation and c_m is set to a fixed value. An alternative would be a dynamic procedures, where the value of c_m is adapted locally [115–117]. The filter width is set to $\Delta = \sqrt[3]{\Delta_x \Delta_y \Delta_z}$ with Δ_i as element size in x, y, z direction. D_m represents the model-specific differential operator, which is described afterwards.

The second group consists of hybrid turbulence models, which combines LES and URANS [50]. In the case of LES, the approach is fundamentally identical to those mentioned above. A small adjustment is done for the filter width, which is set to $\Delta = \max(\Delta_x, \Delta_y, \Delta_z)$, corresponding to the investigations in [118, 119]. In case of an insufficient local grid size (in terms of LES), these models revert to a URANS formulation. For URANS, which bases on the averaged form of equations (2.1) to (2.6), the eddy viscosity is generally modeled as

$$\mu_t \propto \overline{\rho} \frac{L^2}{t} \,, \tag{2.8}$$

with a characteristic length scale L and characteristic time scale t [104]. A great advantage of this approach is that a significant decrease in computational effort can be achieved [120], which is partially true for wall-bounded flows.

Finally, the third group is formed by new URANS approaches, developed in the recent past. They have the capability to resolve a substantial amount of turbulent fluctuations. The first type of these so-called “second-generation” URANS models is the partially-averaged Navier-Stokes (PANS) approach [121–123], where the eddy viscosity is factorized in a suitable way. The second type, which is investigated here, is scale-adaptive simulation (SAS), which results from revisiting the $k-L$ model developed by Rotta [124].

The following investigation focusses on the Smagorinsky, WALE, Sigma, DES-SST and SAS-SST turbulence model and the specific formulations are described next.

Smagorinsky model

This is one of the most widely used LES models [125] and has already been applied to a notable number of ICE simulations [53, 60–65]. The differential operator is defined as

$$D_m = \sqrt{2\widetilde{S}_{ij}\widetilde{S}_{ij}}\,, \tag{2.9}$$

with the strain rate

$$\widetilde{S}_{ij} = 0.5\left(\frac{\partial \widetilde{u}_i}{\partial x_j} + \frac{\partial \widetilde{u}_j}{\partial x_i}\right). \tag{2.10}$$

To avoid an overprediction of the eddy viscosity in the wall boundary layers, van Driest damping [126] is used. It is defined as

$$f_D(y^+) = 1 - e^{-\frac{y^+}{A^+}}\,, \tag{2.11}$$

with the model constant A^+ and the dimensionless wall distance y^+. Throughout this study, the model constant c_m and A^+ is set to 0.1 and 25, respectively [49].

WALE model

The wall-adaptive local eddy viscosity (WALE) model [127] has already been used for ICE simulations [66–68]. D_m is defined as

$$D_m = \frac{\left(S^d_{ij}S^d_{ij}\right)^{\frac{3}{2}}}{(\widetilde{S}_{ij}\widetilde{S}_{ij})^{\frac{5}{2}} + (S^d_{ij}S^d_{ij})^{\frac{5}{4}}}\,, \tag{2.12}$$

with

$$S^d_{ij} = \widetilde{S}_{ik}\widetilde{S}_{kj} + \widetilde{\Omega}_{ik}\widetilde{\Omega}_{kj} - \frac{1}{3}(\widetilde{S}_{mn}\widetilde{S}_{mn} - \widetilde{\Omega}_{mn}\widetilde{\Omega}_{mn}) \tag{2.13}$$

and

$$\widetilde{\Omega}_{ij} = 0.5\left(\frac{\partial \widetilde{u}_i}{\partial x_j} - \frac{\partial \widetilde{u}_j}{\partial x_i}\right). \tag{2.14}$$

An important feature of this model is that it exhibits the correct scaling for the eddy viscosity $\mu_t = \mathcal{O}(y^3)$ close to the wall (wall corresponds to $y = 0$). Furthermore, it has the capability to reproduce the laminar to turbulent transition due to zero eddy viscosity in the case of pure shear. For this work, c_m is set to 0.5 [127].

Sigma model

The Sigma model was developed by Nicoud et al. [128], where D_m is defined as

$$D_m = \frac{\sigma_3(\sigma_1 - \sigma_2)(\sigma_2 - \sigma_3)}{\sigma_1^2}, \tag{2.15}$$

with the singular values σ_i of the matrix $G_{ij} = \partial\widetilde{u}_k/\partial x_i \, \partial\widetilde{u}_k/\partial x_j$. Like the WALE model, the Sigma model ensures the correct scaling of the eddy viscosity towards the wall. Furthermore, there are improvements in terms of 2D flows, solid body rotation, and isotropic expansion and contraction [128]. The model constant c_m is set to 1.5 [129].

DES-SST model

Travin et al. [130] developed a detached eddy simulation model (DES-SST; DES in the following), which belongs to the group of hybrid LES-URANS turbulence models and was successfully applied to ICEs [51, 55]. The underlying URANS approach is the shear stress transport (SST) turbulence model [131], which solves a transport equation for the turbulent kinetic energy $\widetilde{k}$ and the turbulent frequency $\widetilde{\omega}$ [104]. The dissipation term of the $\widetilde{k}$ equation in the SST model is modified:

$$\widetilde{\varepsilon}_{SST} = \beta^* \widetilde{k}\widetilde{\omega} = \frac{\widetilde{k}^{\frac{3}{2}}}{L_t} \rightarrow \widetilde{\varepsilon}_{DES} = \frac{\widetilde{k}^{\frac{3}{2}}}{L_{DES}}, \tag{2.16}$$

with the constant β^*. In the case of a sufficiently fine spatial resolution, the model-specific length scale

$$L_{DES} = min(L_t, c_{DES}\Delta) \tag{2.17}$$

switches from the integral length scale L_t (i.e. the URANS approach) to a grid-dependent length scale $c_{DES}\Delta$ (i.e. the LES approach). The model constants are set in line with [131, 132] and [86].

SAS-SST model

For the SAS-SST model (SAS in the following) [133], an additional source term Q_{SAS}, defined as

$$Q_{SAS} = \max\left[c_1 \overline{\rho}\kappa\widetilde{S}_{ij}^2 \left(\frac{L_t}{L_{\nu K}}\right)^2 - c_2 \overline{\rho}\widetilde{k} \, \max\left(\frac{1}{\widetilde{\omega}^2}\left(\frac{\partial\widetilde{\omega}}{\partial x_j}\right)^2, \frac{1}{\widetilde{k}^2}\left(\frac{\partial\widetilde{k}}{\partial x_j}\right)^2\right), 0\right], \tag{2.18}$$

is introduced into the scale-determining $\widetilde{\omega}$ equation. c_1 and c_2 denote model constants, while κ represents the von Kármán constant. The von Kármán length scale

$$L_{\nu K} = \kappa \frac{\sqrt{2\widetilde{S}_{ij}\widetilde{S}_{ij}}}{u''} \tag{2.19}$$

is calculated based on

$$u'' = \sqrt{\frac{\partial^2 \widetilde{u}_i}{\partial x_k^2} \frac{\partial^2 \widetilde{u}_i}{\partial x_j^2}}. \tag{2.20}$$

L_{vK} allows the turbulence model to recognize resolved scales in unstable flows and to adjust the eddy viscosity to a level which allows the formation of a turbulent spectrum, while attached boundary layers are treated in URANS mode. The capability of the SAS model to resolve small-scale turbulent fluctuations is shown in [133–138]. The model constants are the same as in [132, 133].

2.3 Solver, ICE methodology and engine basics

All simulations are performed using ANSYS CFX R16.0, with the exception of section 4.2 (ANSYS CFX R15.0). The transport equations are discretized using a node-based finite volume method, which is conservative and time-implicit [139–141]. A control volume is constructed around each nodal point of the mesh and the fluxes are computed at the integration points located at the sub faces between two control volumes. The mass flow is evaluated such that a pressure-velocity coupling is achieved [142]. The discrete system of equations is solved by a coupled algebraic multi-grid method [141]. For a reduced numerical diffusion, a second-order backward scheme in time is used for all simulations presented in this thesis. The solver's suitability for SRSs in ICEs has investigated extensively and demonstrated in previous works [19, 51, 55].

A crucial topic for the simulation of ICEs is the rather complex mesh generation taking into account the moving piston and valves, which require special treatment. Here, the so-called *key grid approach* is applied. Starting from an initial mesh, the grid is deformed according to the moving boundaries until a critical mesh quality is reached. At this point a new mesh is generated and the previous results are interpolated to it. A detailed description of the methodology can be found in [114, 143]. Both, the implications of the mesh morphing and the interpolation in ANSYS CFX was investigated in detail in [55].

In this work, several engines are considered and analyzed by a variety of different methods. To present the results in a consistent and understandable manner, two basics have to be defined. The first concern is the coordinate system, illustrated in figure 2.1.
The origin of the coordinate system lies in the plane defined by the upper edge of the cylinder head gasket. Its x axis is oriented normal to the engine symmetry plane and the z axis is aligned with the cylinder axis and points towards the cylinder head.

The second concern the definition of the engine phases (which may differ from those presented in the original publications). For all realistic engines, the working process is divided into

- the **intake stroke** (−360° to −180 °CA),
- the **compression stroke** (−180° to 0 °CA),
- the **expansion stroke** (0° to 180 °CA) and
- the **exhaust stroke** (180° to 360 °CA),

only related to the crank angle. If not otherwise stated, this holds throughout this thesis.

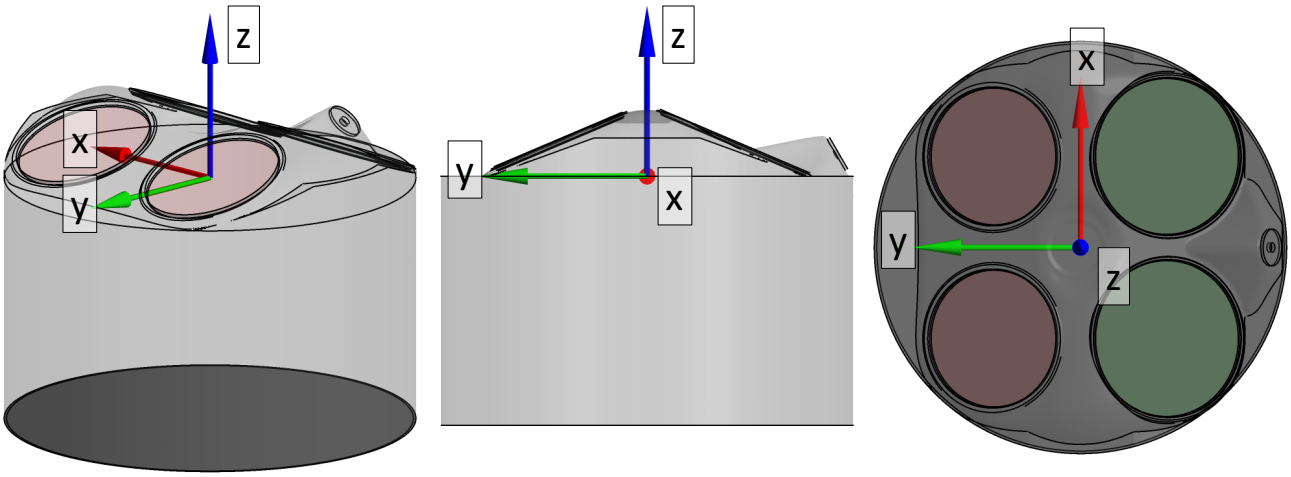

Figure 2.1: Definition of coordinate system used for IC engine investigations. Origin is positioned in the plane formed by the upper edge of cylinder head gasket. Red and green valves are related to the exhaust and intake side, respectively.

2.4 Definition of statistical quantities

For quasi-stationary flows, time-averaged quantities are typically used. In contrast, the analysis of non-stationary flows is more challenging and the calculation of statistical quantities varies from case to case. In this thesis, different evaluation methods are applied which are described next. An averaged quantity is defined as

$$\langle \phi \rangle_N(\mathbf{x}, \varphi) = \frac{1}{|N|} \sum_{n \in N} \phi(\mathbf{x}, \varphi, n), \tag{2.21}$$

where $\phi(\mathbf{x}, \varphi, n)$ represents an scalar/vectorial quantity which depends on the spatial coordinate $\mathbf{x}$, the crank angle φ and the cycle n. $|N|$ represents the total number of:

- Samples in time → time-averaged quantity denoted by $\langle \phi \rangle_T$
- Cycles → phase-averaged quantity denoted by $\langle \phi \rangle_P$
- Samples along a line/trajectory → line-averaged quantity denoted by $\langle \phi \rangle_L$
- Samples within a defined area → area-averaged quantity denoted by $\langle \phi \rangle_A$
- Samples within a volume → volume-averaged quantity denoted by $\langle \phi \rangle_V$

The corresponding fluctuations and its root mean square (rms) are calculated as

$$\phi'(\mathbf{x}, \varphi, n) = \phi(\mathbf{x}, \varphi, n) - \langle \phi \rangle_N(\mathbf{x}, \varphi) \tag{2.22}$$

and

$$\phi'_{\mathrm{rms}}(\mathbf{x}, \varphi) = \sqrt{\frac{1}{|N|} \sum_{n \in N} \frac{1}{k} \sum_{i=1}^{k} \phi_i'^2(\mathbf{x}, \varphi, n)}, \tag{2.23}$$

where k represents the number of variables to be averaged (e.g. 3 if the rms is calculated for all 3 velocity components).

In section 4.2, a subset of specific statistical values are calculated. These subsets base on a reduced number of instantaneous flow fields, whereby these flow fields are identical in terms of a conditioning vector Ξ. A subset average is defined according to

$$\langle\phi\rangle_{M(\Xi)}(\mathbf{x},\varphi) = \frac{1}{|M(\Xi)|}\sum_{n\in M(\Xi)}\phi(\mathbf{x},\varphi,n)\,. \tag{2.24}$$

As can be seen, equation (2.24) is very similar to equation (2.21), while the individual subsets $M(\Xi)$ are defined by

$$M(\Xi_i)\cap M(\Xi_j) = \emptyset \qquad \text{for all} \qquad i\neq j \tag{2.25}$$

and

$$\bigcup_{s=1}^{S} M(\Xi_s) = N\,, \tag{2.26}$$

where S represents the total number of subsets. Based on this conditional average, the following decomposition becomes feasible

$$\phi(\mathbf{x},\varphi,n) = \langle\phi\rangle_{M(\Xi)}(\mathbf{x},\varphi) + \phi^*(\mathbf{x},\varphi,n) \qquad \text{for all} \qquad n\in M(\Xi)\,. \tag{2.27}$$

Averaging the resulting subset-dependent flow fields yields

$$\langle\phi\rangle_N(\mathbf{x},\varphi) = \sum_{s=1}^{S}\frac{|M(\Xi_s)|}{|N|}\langle\phi\rangle_{M(\Xi_s)}(\mathbf{x},\varphi)\,. \tag{2.28}$$

The quantification of the subset specific small-scale fluctuations is performed similarly to Eq. (2.22)

$$\phi^*_{rms,M(\Xi)}(\mathbf{x},\varphi) = \sqrt{\frac{1}{|M(\Xi)|}\sum_{n\in M(\Xi)}\frac{1}{k}\sum_{i=1}^{k}\phi_i^{*2}(\mathbf{x},\varphi,n)}\,. \tag{2.29}$$

Please keep in mind that each cycle n belongs to one subset s. The root mean square of the coherent structure fluctuations is

$$\phi^{\dagger}_{rms}(\mathbf{x},\varphi) = \sqrt{\sum_{s=1}^{S}\frac{|M(\Xi_s)|}{|N|}\frac{1}{k}\sum_{i=1}^{k}\left(\langle\phi_i\rangle_{M(\Xi_s)} - \langle\phi_i\rangle_N\right)^2}\,, \tag{2.30}$$

and this can be seen as an indicator for large-scale CCV. The fluctuations are defined by the difference of the globally averaged flow field (Eq. (2.21)) and the subset average (Eq. (2.24)).

3 IC engine modeling aspects

This section recaps selected modeling aspects for SRSs in ICEs. The first part addresses the location of the boundaries and the treatment of the intake and exhaust port during the time period with closed intake and exhaust valves. The second part investigates selected turbulence models (presented in section 2.2) in terms of their applicability and accuracy in IC engine flows.

3.1 Set up a scale-resolving IC engine case

An appropriate treatment of boundaries and boundary conditions is a crucial point in scale-resolving engine simulations. Literature offers different strategies for the handling of the intake and the exhaust ports and each of them has a different effect on the temporal and spatial development of resolved fluctuations within these regions. The presented study investigates the impact of two aspects, namely the location of boundaries and the temporal treatment of the intake and exhaust ports. The aim is to identify the requirements to obtain an accurate in-cylinder velocity field.

This section is structured as follows. First, an overview of the engine setup and of the analyzed numerical domains is given. Afterwards, the modeling strategies are compared to each other and to the experimental values [82] in terms of the phase-averaged in-cylinder mass, pressure and velocities. This is followed by an investigation of the in-cylinder charge motion. The final part summarizes the results. For further details and results, the reader is referred to [144].

3.1.1 Engine and numerical setup

The analysis bases on the well-established benchmark engine from TU Darmstadt under motored conditions at 800 rpm as presented in [82]. The engine is characterized by very long ports, while the intake port is designed in such a way that a high level of charge motion (i.e. tumble) is introduced.

The top of figure 3.1 shows the first and most CPU-intensive modeling strategy, referred as *long ports permanently* (LPP). Here, the entire intake and exhaust port with a length of 1680 mm and 1080 mm (measured from the flange of the cylinder head up to the pressure plenum) are simulated throughout the entire operating cycle. This strategy is similar to those chosen in [51–53] and offers two major benefits:

- The simulated spatial and temporal development of the mean flow field, turbulent structures and temperature field within the ports allows the usage of relatively simple boundary conditions (e.g. no superimposed turbulence necessary).
- Due to the spatial extension of the domain, it can be assumed that there is a minimized influence of the boundary conditions onto the flow field within the cylinder (at least for this engine setup).

In contrast, the strategy with *short ports permanently* activated (SPP) leads to a significantly reduced numerical domain. The intake and the exhaust ports, which are calculated throughout the cycle, are shortened to a length of 192 mm and 122 mm. Thus, the temporal and spatial development of the flow is only simulated in close vicinity to the valves and the development in the upstream/downstream part has to be taken into account by the boundary conditions. Due to the small distance between the boundaries and the valves, the flow field imposed at the boundaries are likely to still exist at the (intake) valves.

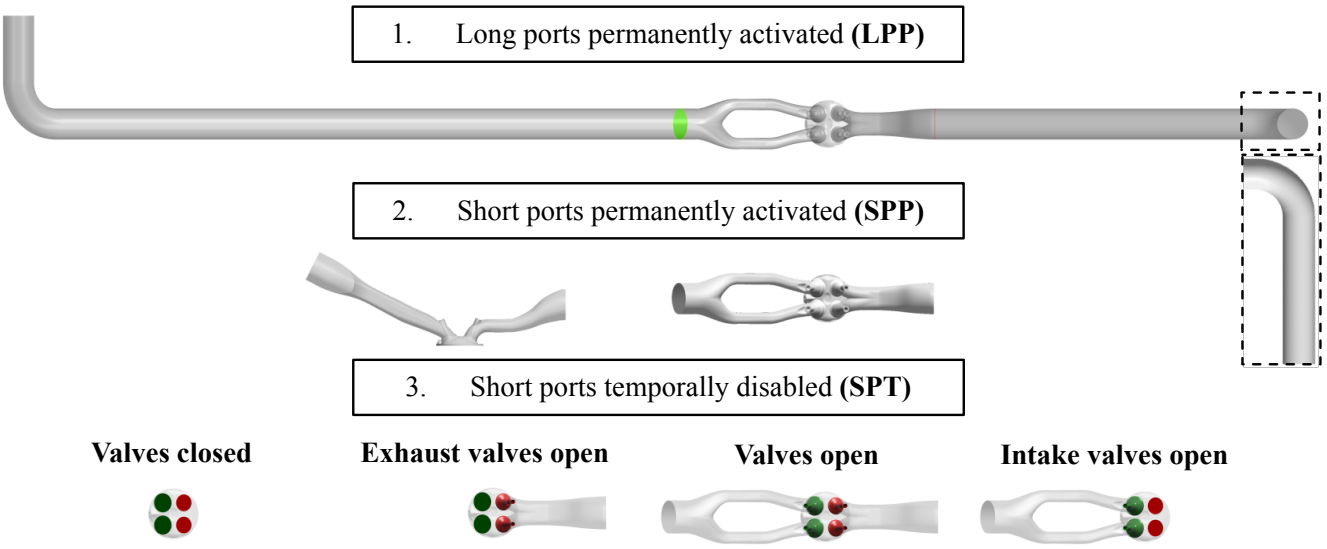

Figure 3.1: Numerical domain of three different port modeling strategies at TDC. The green and red areas in the LPP model indicate the boundaries of the short port versions. Figure adapted from [144].

A great advantage is the significant reduced demand of computational resources (compared to LPP). A similar strategy was chosen for the investigations presented in [54–59].

The last and least CPU-intensive modeling strategy (*short ports temporally*; SPT) bases on the SPP domain. Here, the ports are temporally disabled for the time period when the corresponding valves are closed and readded to the domain when the valves reopen. This methodology (applied in [60]) demands that the flow field of each port is reinitialized within each individual cycle. In this study the reinitialization is done by one (previously calculated) flow field for each port to minimize the computational costs.

For this compressible case, the full set of equations (2.1) to (2.6) has to be solved. The scale-adaptive simulation (SAS-SST) turbulence model (see section 2.2) is chosen for the highly complex in-cylinder flow field. All simulations are based on an identical mesh topology within the combustion chamber, consisting of tetrahedral, prismatic and hexahedral elements with a maximum cell size of 1 mm. Mesh refinements of 0.25 mm are defined at the intake jet region, the valve shaft and the separation edge within the intake port. The boundary layer flow is resolved by 10 prism layers with a minimum height of 25 μm next to the wall. A calibrated 0D/1D engine model was used to generate the necessary time-resolved boundary conditions for each modeling strategy. For the short port models, synthetic fluctuations [145] are superimposed to the time-resolved boundary condition at the intake. The simulation of 60 full engine cycles for each case ensures reasonable statistics.

3.1.2 Results

A fundamental element for the comparison is the agreement in terms of the trapped in-cylinder mass (not shown here). In general, all models show almost identical results with small discrepancies of about 2 % at closed intake valves (IVC). These discrepancies are traced back to differences at the input of thermal energy within the intake port, which also affects the in-cylinder temperature (and consequently the density) at IVC. Corresponding to the differences at the cylinder charge, there are small differences

at the peak pressure. The lowest peak pressure of 12.87 bar occurs in the case of SPT, while for the SPP and LPP cases a pressure of 12.92 bar and 13.14 bar is obtained.

Figure 3.2 illustrates the phase-averaged in-plane velocity components on the engine symmetry plane ($x = 0\,m$). Please note that fTDC is defined at 0 °CA.

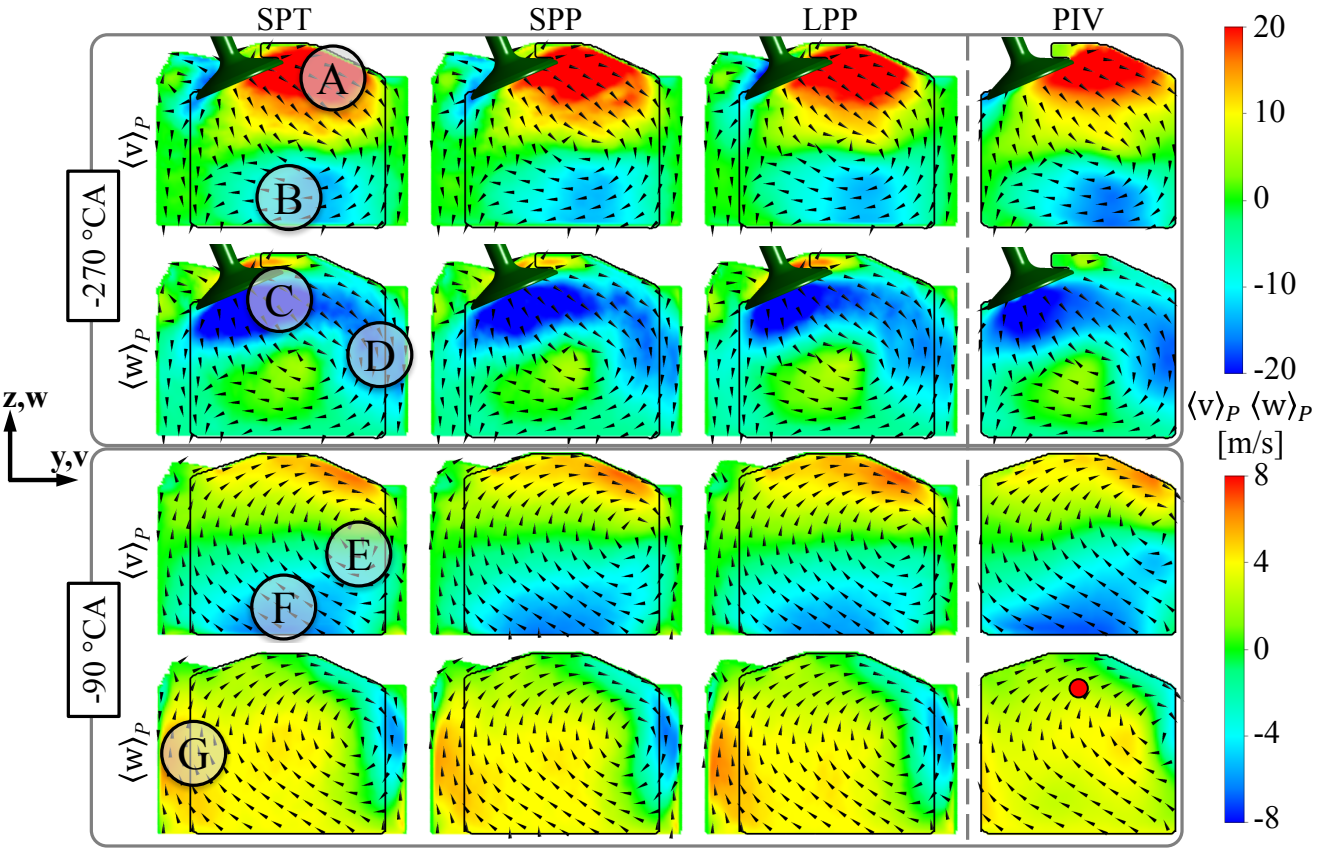

Figure 3.2: Phase-averaged in-plane velocity components $\langle v \rangle_P$ and $\langle w \rangle_P$ on engine symmetry plane. The red dot denotes the origin of the coordinate system and the x axis is the out-of-plane component. Firing TDC is defined at 0 °CA. Figure adapted from [144].

The velocity vectors at −270 °CA (i.e. during intake stroke) indicate a good agreement with respect to the general flow topology. For all results, there exist a distinctive intake jet and tumble structure develops. The highest absolute values for $\langle v \rangle_P$ and $\langle w \rangle_P$ ($> 20\,m\,s^{-1}$) occur in the vicinity of the intake valve (regions **A** and **C**). Interestingly these are the regions with the most notable differences. This is in good agreement to the investigations in [86], which has already pointed out the difficulties of capturing the intake jet correctly. The intake jet is deflected by the cylinder liner and the piston surface, leading to high velocities in regions **B** and **D**. The bottom of figure 3.2 illustrates the phase-averaged in-plane velocity components on the engine symmetry plane at −90 °CA (i.e. during compression stroke), which correspond even better. All results exhibit a TC (indicated by the circularly arranged velocity vectors) within the right half of the combustion chamber (region **E**). Compared to the simulation, the PIV data show a slightly higher absolute value for $\langle v \rangle_P$ in region **F**, while minor differences between the simulations occur in region **G**.

Next, the integral in-cylinder charge motion with respect to the x axis is evaluated. This is done by the scalar quantity

$$\mathrm{Tu_x}(\varphi,n)=\frac{1}{2\pi\Omega}\frac{\int_V \rho(\varphi,n)[(\mathrm{y}-\mathrm{y_c})\mathrm{v_z}(\varphi,n)-(\mathrm{z}-\mathrm{z_c})\mathrm{v_y}(\varphi,n)]dV}{\int_V \rho(\varphi,n)[(\mathrm{y}-\mathrm{y_c})^2+(\mathrm{z}-\mathrm{z_c})^2]dV}, \tag{3.1}$$

with Ω and V as the engine speed and the in-cylinder volume, respectively. $\mathrm{y_c}$ and $\mathrm{z_c}$ denote the center of the in-cylinder fluid mass. The sign of $\mathrm{Tu_x}$ represents the direction of rotation.

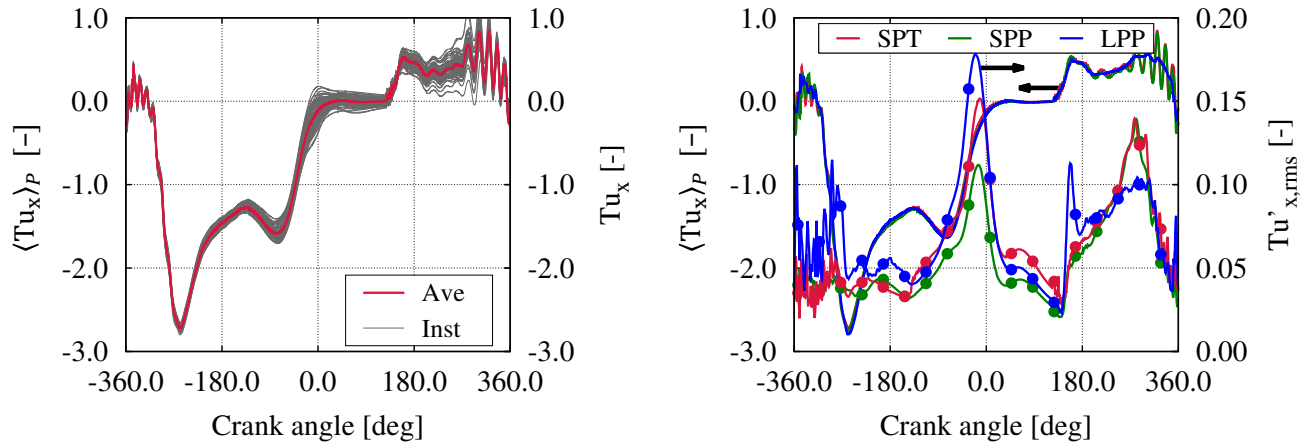

Figure 3.3: Left: Phase-averaged and instantaneous in-cylinder charge motion obtained by SPT. Right: Phase-averaged in-cylinder charge motion and its fluctuations obtained by SPT, SPP and LPP. Figure adapted from [144].

The left of figure 3.3 illustrates the phase-averaged and the instantaneous values for $\mathrm{Tu_x}$ obtained by the SPT strategy. A significant tumble motion develops during the intake stroke (identifiable from the increasing absolute value of $\langle \mathrm{Tu_x} \rangle_P$), which is highly relevant for the mixing and combustion process of modern direct injecting gasoline engines. It reaches a maximum of $|\langle \mathrm{Tu_x} \rangle_P| \approx 2.7$ at $-260\,°\mathrm{CA}$, decreases afterwards and remains on a level of $|\langle \mathrm{Tu_x} \rangle_P| = 1.42 \pm 0.15$ in the time period between $-200\,°\mathrm{CA}$ and $-60\,°\mathrm{CA}$. From this point to $0\,°\mathrm{CA}$ the tumble motion vanishes. Up to exhaust valve opens (EVO), $\langle \mathrm{Tu_x} \rangle_P$ remains at zero. The subsequent development of the tumble motion is specific for a motored case and can not be simply transferred to a fired engine setup. A reversed mass flow into the combustion chamber at EVO, causes an inverted tumble motion during the exhaust stroke. Similar to the phase-averaged velocity field, all simulations exhibit almost identical results in terms of $\langle \mathrm{Tu_x} \rangle_P$ (right of figure 3.3).
The rms of the fluctuations $\mathrm{Tu_x'}$, illustrated on the right of figure 3.3, quantifies the cyclic variability of the in-cylinder charge motion. It is interesting to see that up to about $-160\,°\mathrm{CA}$ there are almost no CCVs, even though there is a highly turbulent flow field for all modeling strategies. An explanation for this is the distinctive intake jet, which enters the combustion chamber approximately in the same direction each cycle and is the main contributor to the angular momentum (nominator in equation (3.1)) during the intake stroke. The CCVs rapidly increase at IVC reaching a maximum value shortly before $0\,°\mathrm{CA}$. During the expansion stroke, the cyclic variability decreases to a global minimum at about $160\,°\mathrm{CA}$, followed by an increase and a subsequently decrease during the exhaust stroke. In total, all models exhibit the same trends for the in-cylinder charge motion and its CCVs, though there are deviations between the exact values (e.g. shortly before fTDC).

3.1.3 Interim findings

Three different port modeling strategies (long ports version, short ports version and a version with short and temporally disabled ports) for scale-resolving ICE simulations were investigated. The results of the different port models were compared to each other as well as to the experimental results and they are summarized as follows:

i) In-cylinder mass, in-cylinder pressure and in-cylinder velocity field:
All models exhibit similar results for the integral quantities. The LPP model differs most from the other approaches. A qualitative and quantitative comparison of the velocity components on the engine symmetry plane shows good agreement between the simulations and the experimental results.

ii) In-cylinder charge motion:
Each port modeling strategy exhibits a distinctive and very similar intake jet and a corresponding in-cylinder charge motion (tumble). The tumble dominates the in-cylinder flow field during the intake and compression stroke. Examining the phase-averaged in-cylinder charge motion and its CCV, all models yield similar results.

3.2 Choice of an appropriate turbulence model

In the recent past, a number of different turbulence models have been applied to IC engine flows [51, 53, 55, 60–68]. However, based on the published results, a one-by-one comparison of these models is difficult because of the large number of different engine setups and numerical approaches. In the following, five turbulence models (three LES models, one hybrid model and one second-generation URANS model) are investigated with the goal to analyze the models' accuracy and capability to capture fluctuations. For a consistent and systematic comparison, all simulations are performed on the same grid and numerical approach (discretization, time integration).

This section is structured as follows. First, the engine setup, for which experimental, DNS and LES data are available [61, 68, 112, 113, 146, 147], is described. Next, the results obtained by the different turbulence models are compared to each other in terms of the phase-averaged velocity, resolved velocity fluctuations and variability of the tumble. Further results (e.g. comparison to experimental and DNS data as well as investigation of structural aspects of the resolved fluctuations [148]) are published in [149].

3.2.1 Engine and numerical setup

Figure 3.4 illustrates the axisymmetric engine setup, running at 200 rpm under motored condition. It consists of a flat piston, a flat dome and the cylindrical intake pipe and the single non-moving valve are concentric with the cylinder liner. A full cycle consists of an intake stroke (−360 °CA to −180 °CA) and exhaust stroke (−180 °CA to 0 °CA; not considered) with its top dead center at 0 °CA. [112, 113] offer a detailed description of the engine.

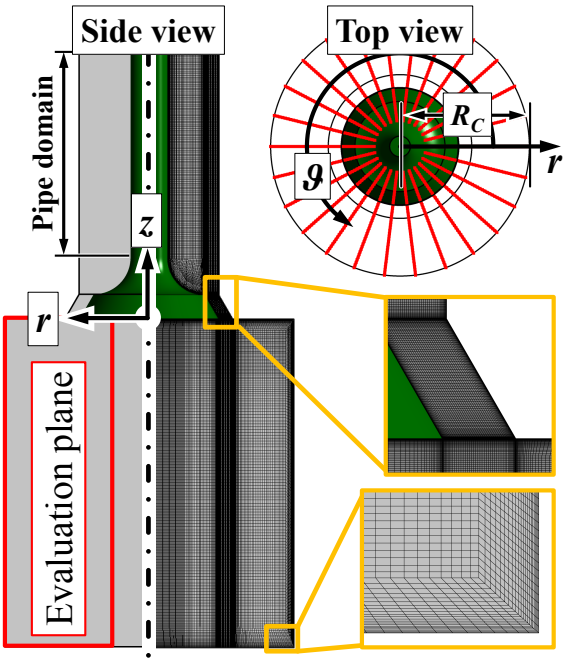

Figure 3.4: Geometry and mesh at bottom dead center and cylindrical coordinate system used. The evaluation plane is indicated in red. The red lines in the top view mark the azimuthal arrangement of the evaluation planes. Furthermore, the simulation domain of the preliminary pipe simulation is indicated. Figure adapted from [149].

All simulations are performed on a single hexahedral mesh (i.e. no remeshing necessary) with 14.5×10^6 nodes, a maximum element width of 0.5 mm and a mesh refinement at the wall up to an element height of 20 μm. The same sinusoidal piston movement is used as in the experiment. The time step width is adapted to the piston speed, reaching a minimum and a maximum value of 18.75×10^{-3} °CA (15.6 μs) and 25×10^{-3} °CA (20.8 μs), respectively. This ensures a *Courant-Friedrichs-Lewy* (CFL) number smaller than unity for almost the entire domain. Corresponding to the experimental conditions, the simulations are performed at 1.013 bar and 293 K. Due to the low velocities ($|\mathbf{u}|_{max} \approx 12\,\mathrm{m\,s^{-1}}$ at −270 °CA), an incompressible approach is used. The average flow rate at the inlet is calculated based on the piston speed and the ratio of the piston and the inlet area. Furthermore, resolved turbulent fluctuations were superimposed at the inlet, generated by a stand-alone simulation of the cylindrical intake pipe (indicated in figure 3.4).

Due to the rotational symmetry of the setup, a total number of 26 realizations is chosen for each cycle and crank angle to calculate statistical quantities. For each turbulence model, 13 consecutive cycles were calculated. The first cycle was initialized by a quiescent flow field and discarded for all analyses, which leads to a total number of 312 realizations for each model and crank angle. The average of these 312 realizations is denoted as "phase-average" ($\langle\phi\rangle_P$) in the following.

3.2.2 Results

The upper row of figure 3.5 illustrates the phase-averaged velocity magnitude at −270 °CA. The resulting flow fields of all models, consisting of an intake jet and a tumble structure in the center of the evaluation plane, differ only slightly. The intake jet is guided by the valve gap towards the cylinder liner and deflected towards the piston afterwards. Compared to the other models, a lower penetration depth is identified for the DES results. Furthermore, there are small differences for the TC position, indicated by zero velocity magnitude in the center of the combustion chamber. The DES model exhibits a shift towards the cylinder head. The models show further discrepancies at the flow structure close to the piston surface.

The bottom row of figure 3.5 visualizes the rms of the resolved velocity fluctuations (see equation (2.23)). High fluctuations occur in the shear layer of the intake jet. With increasing penetration depth, the fluctuations spread over the entire intake jet. Strong velocity fluctuations also exist in the area where the jet is redirected by the cylinder liner. However, there are noticeable deviations between the different turbulence models in this region. The fluctuations obtained by the Smagorinsky and the SAS models extend deeper into the combustion chamber. In contrast, the WALE and Sigma models show smaller regions with high fluctuation levels. For all models, slightly increased levels of fluctuation occur in the region of the presumed TC position (see top row). These fluctuations are partially attributed to CCVs of coherent structures (i.e. precessing vortex core; discussed below) as investigated in [51, 81, 137].

A very important aspect of IC engine flows is the cyclic variability of the large-scale tumble structure, usually known as the precessing vortex core. At first, the Γ_2-criterion (introduced in [150]; applicable due to the axissymmetry of the engine setup) is used to analyze the spatial and temporal development of the phase-averaged TC position. It is defined as

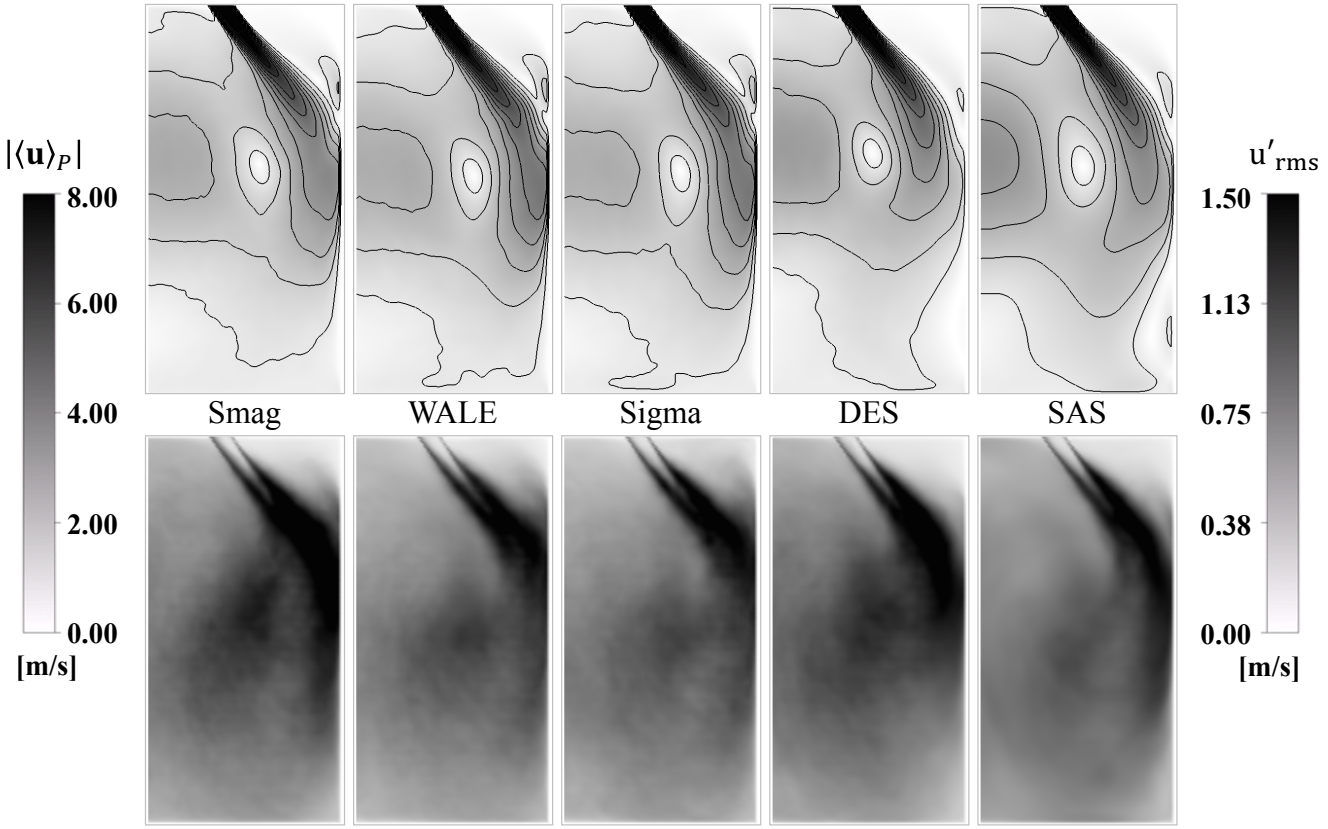

Figure 3.5: Comparison of the different turbulence models at −270 °CA. Top row: Phase-averaged velocity magnitude. Bottom row: Resolved velocity fluctuations evaluated by the root mean square. Figure adapted from [149].

$$\Gamma_2(r,z,\varphi) = \frac{1}{A}\int_{(r_o,z_o)\in A} \frac{[\mathbf{r}(r_o,z_o)\times(\mathbf{u}(r_o,z_o,\varphi)-\langle\mathbf{u}\rangle_A(r,z,\varphi))]}{\|\mathbf{r}(r_o,z_o)\|\,\|\mathbf{u}(r_o,z_o,\varphi)-\langle\mathbf{u}\rangle_A(r,z,\varphi)\|}\cdot\mathbf{n}\,\mathrm{d}A, \tag{3.2}$$

with a specified area A and its normal vector $\mathbf{n}$ at the currently considered point (r,z). $\mathbf{r}(r_o,z_o)$ describes the distance vector between (r,z) and the other point (r_o,z_o), which lies within the area A. $\mathbf{u}(r_o,z_o)$ represents the velocity vector at position (r_o,z_o), and $\langle\mathbf{u}\rangle_A(r,z)$ is the averaged velocity in A. For the Γ_2-criterion either the phase-averaged or the individual cycle velocity field can be used.

The left-hand side of figure 3.6 illustrates the temporal development of the phase-averaged TC position for all models. Initially, no distinct tumble structure is established independent of the model and thus the analysis starts at −330 °CA, where larger differences for the TC positions are obtained. These differences decrease up to −324 °CA (indicated by squares). Interestingly, for this specific crank angle, the z coordinate of the TC position is almost identical for all turbulence models, while there are radial differences. Up to −270 °CA (dots), the models predict different TC positions, and two groups are identified. The first group consists of the DES and the SAS models, while the Smagorinsky, WALE and Sigma models form the second group. Within each group the TCs are close together. Up to −216 °CA (triangles), the deviations between these groups become smaller.

The phase-averaged velocity field and the TC position (indicated by red dots) for the Sigma model at the three selected crank angles are shown on the right-hand side of figure 3.6. As described before, there is a

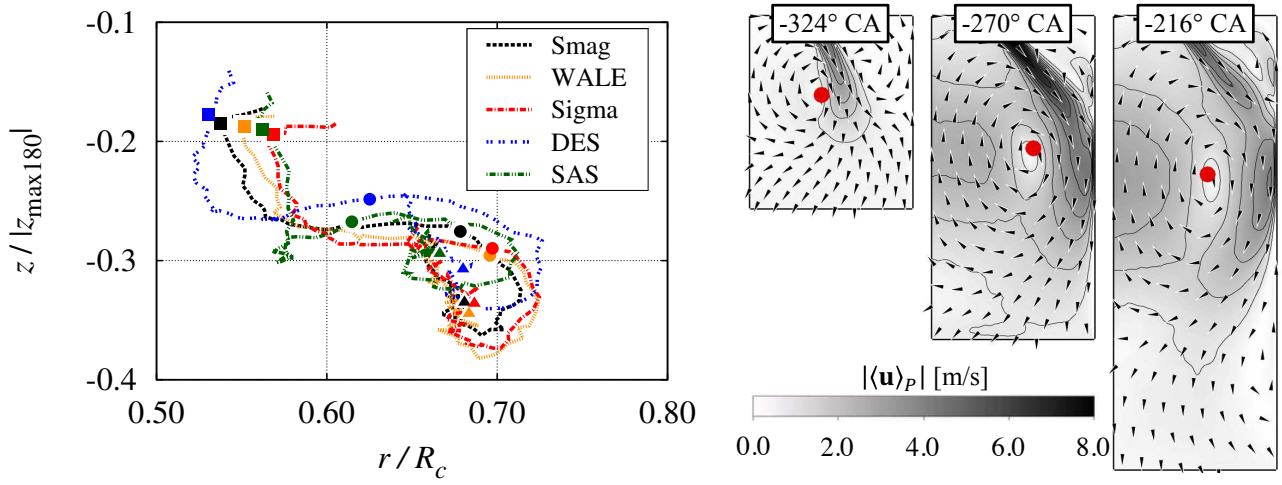

Figure 3.6: Left: Temporal evolution of the phase-averaged tumble center position within the evaluation plane. Symbols mark different points in time: −324 °CA (square), −270 °CA (circle), −216 °CA (triangle) Right: Phase-averaged velocity magnitude and tumble center position (indicated by red dots) of the Sigma model. Figure from [149].

distinctive intake jet at −324°, −270° and −216 °CA. Furthermore, a tumble structure is clearly identified for −270°, and −216 °CA and the calculated TC lies close to the point with a zero velocity magnitude.

The left of figure 3.7 shows the phase-averaged and the instantaneous TC positions for the Sigma model at −270 °CA, where a significant clustering of the instantaneous TC is obtained. In general, the results of the other turbulence models are very similar, while there are differences in terms of the variability. The right of figure 3.7 illustrates the phase-averaged distance between the instantaneous and

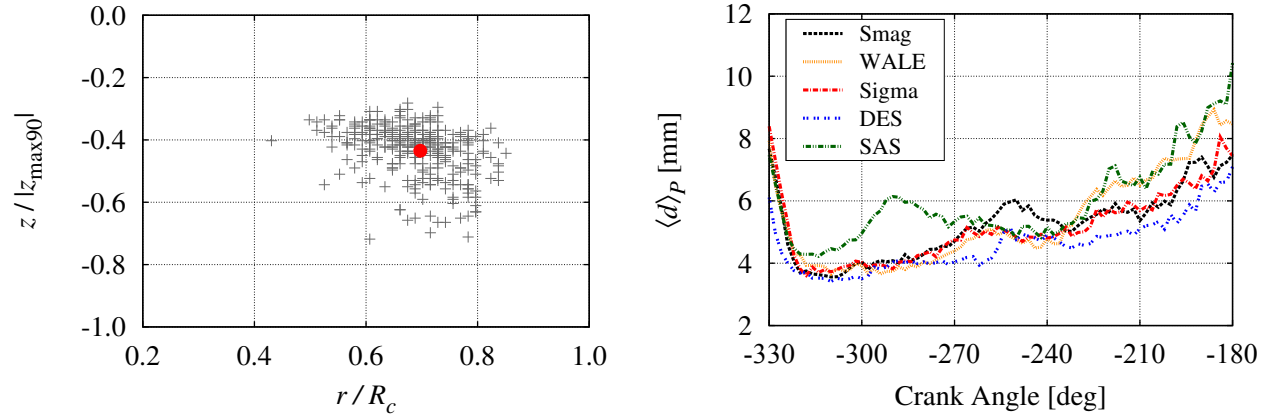

Figure 3.7: Left: Phase-averaged (dot) and instantaneous tumble center positions for Sigma model at −270 °CA. Right: Average distance between the phase-averaged and the instantaneous tumble center for all turbulence models. Figure adapted from [149].

the phase-averaged TC position as a measure of the spatial fluctuation of the vortex core. This distance is calculated by

$$\langle d \rangle_P = \frac{1}{N} \sum_{n=1}^{N} \sqrt{(r(n) - \langle r \rangle_P)^2 + (z(n) - \langle z \rangle_P)^2} \tag{3.3}$$

with the total number of realizations N and the r and z coordinates of the instantaneous and phase-averaged TC. The initial phase of the tumble formation starts at −330 °CA, and all models exhibit great variability in the TC position. The Sigma model exhibits the largest averaged distance ($\langle d \rangle_P = 8.2\,\text{mm}$), while the lowest value results from the DES model ($\langle d \rangle_P = 6.0\,\text{mm}$). These differences in $\langle d \rangle_P$ decrease until an averaged distance of about 4.0 mm is reached at −320 °CA. Up to about −260 °CA, the SAS model exhibits a noticeable increase ($\langle d \rangle_P = 6.1\,\text{mm}$) and a subsequent decrease for the averaged distance, while the other models exhibit a slight increase to about 5.0 mm. In the range from −262 °CA to −232 °CA an increase (maximum value of 6.0 mm) and a subsequent decrease in $\langle d \rangle_P$ are seen for the Smagorinsky model, while the other models exhibit smaller variations. At −230 °CA, all models show an increase in $\langle d \rangle_P$ until the end of the intake stroke. At this point, the largest value is obtained by the SAS model ($\langle d \rangle_P = 10.0\,\text{mm}$) and the lowest value by the DES model ($\langle d \rangle_P = 6.1\,\text{mm}$).

3.2.3 Interim findings

Several scale-resolving turbulence models were applied to an established ICE benchmark case. The results were compared to each other in terms of the phase-averaged velocities, the resolved velocity fluctuations and the cyclic variability of the coherent vortical structure (“tumble”). The results are summarized as follows:

i) Qualitative evaluation of different turbulence models:
All turbulence models exhibit an almost identical in-cylinder flow structure, while there are small differences in the TC position and the penetration depth of the intake jet. Considering the velocity fluctuations, high values occur in the shear layer of the intake jet, in the area where the jet is redirected by the cylinder liner and in the region of the presumed TC position, while there are notable differences between the different turbulence models.

ii) Temporal development and cyclic variability of the TC position:
All models exhibit a similar temporal development for the phase-averaged TC position and its cyclic variability. In the early phase of the intake stroke, the TC lies in the vicinity of the valve gap. Afterwards, it moves downwards (in line with the piston motion) and towards the cylinder liner. Starting with a high variability in the early phase of tumble formation, the CCVs decrease and remain low until about −270 °CA. Later, the CCVs of the tumble structure increase until the end of the intake stroke.

4 IC engine intake flow

In the following, selected physical aspects in terms of the ICE intake flow are investigated. At first, a quasi steady state flow bench configuration is used to analyze the flow in the vicinity of the intake valve. In the second part, the CCVs of the intake jet and the large-scale tumble are quantified based on a simplified engine setup. Afterwards, a state-of-the-art engine geometry is used to investigate the tumble generation during the intake stroke and its interaction with the piston boundary layer. Finally, two well-known engine setups are investigated with regard to the tumble development during the compression stroke.

4.1 Investigation of the intake jet

The intake flow is the main contributor to the formation of a distinctive large-scale tumble motion. For the following investigations, a quasi steady-state flow bench setup is chosen, which offers an excellent basis for the study of such an intake flow. The presented results base on different meshes and different turbulence models. First, the phase-averaged velocity field and the resolved fluctuations are compared to each other and to 2D-2C PIV. Afterwards, the phase-averaged intake jet is investigated in terms of its position and its velocity along the jet-centerline. A more detailed description of the applied methodology and further investigations can be found in [151].

4.1.1 Flow bench setup

The left-hand side of figure 4.1 shows the complete CAD model (basis for the numerical domain) consisting of the intake port, the cylinder head and the outlet tube. The valve lift is set to $h = 5\,\mathrm{mm}$. Corresponding to the experiment, the simulations are performed at a temperature of 298 K. For the inlet

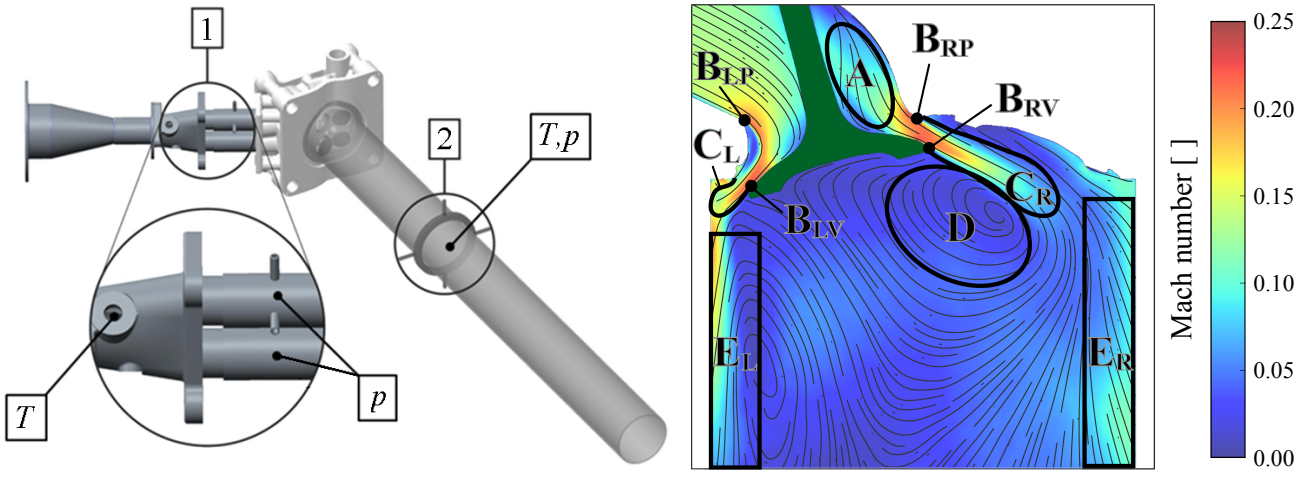

Figure 4.1: Left: CAD model of the intake port, cylinder head and outlet tube, including experimental measurement points for temperature T and pressure p. Right: Ensemble-averaged Mach number and streamlines on the valve middle plane. A to E indicate the most relevant phenomena, referred throughout this section. Subscripts L, R, V and P denote "left", "right", "valve" and "port", respectively. Figure taken from [151].

boundary condition, a mass flow of $3\,\mathrm{kg\,min^{-1}}$ with resolved turbulent fluctuations is chosen and ambient pressure is set at the outlet. Three body conformal and hybrid meshes (coarse, medium and fine)

consisting of tetrahedral, prismatic and hexahedral elements are applied, which are identical in their general topology. The minimum grid size is set to 0.5 mm (coarse), 0.25 mm (medium) and 0.125 mm (fine). Mesh refinements are located in the vicinity of the valve stem, at the separation edges (**B** in the right side of figure 4.1) and in the region of the intake jet (**C** in the right side of figure 4.1). A total number of 10, 15 and 20 (coarse, medium, fine) prisms are chosen for the boundary layer to attempt to place the first layer within the viscous sublayer (i.e. $y^+ < 5$) corresponding to [26, 107]. Depending on the grid size, the time step width is chosen in such a way that a CFL number smaller than unity is obtained for the entire domain. Previous numerical studies [86] have shown that the incompressible set of equations are suitable for this case. This is also confirmed by the right-hand side of figure 4.1, where the maximum Mach number is smaller than 0.25. In this study, the Sigma and the DES-SST models are investigated (see section 2.2). The analysis is limited to specific combinations of turbulence models and meshes, which are termed by the following abbreviations:

1. SF → Sigma on fine mesh
2. SM → Sigma on medium mesh
3. SC → Sigma on coarse mesh
4. DES → DES-SST on medium mesh

Identical to the PIV, horizontal and vertical velocity components on the valve middle plane are used for the comparison and for the investigations in terms of the intake jet. All statistic quantities are calculated by a total number of $N = 600$ samples for the experiment and $N = 400$ samples for each simulation.

4.1.2 Results

The top row of figure 4.2 illustrates the ensemble-averaged velocity magnitude obtained from PIV and simulations. The intake jet ($\mathbf{C_L}$ in figure 4.1), outside the experimental ROI, become detached at the valve ($\mathbf{B_{LV}}$) and is redirected by the cylinder liner ($\mathbf{E_L}$). The intake jet ($\mathbf{C_R}$), identifiable in experiment and simulation, detaches at the valve ($\mathbf{B_{RV}}$ and $\mathbf{B_{RP}}$) and penetrates the combustion chamber towards its center. This part of the jet is the main contributor to the recirculation zone (**D**) and characterized by a significant variation in its position and shape. Further downstream, the jet is deflected by the cylinder liner ($\mathbf{E_R}$) towards the outlet. With the exception of small deviations at the intake jet and the TC ($\mathbf{C_R}$ and **D**), the results are almost identical.
The bottom row of figure 4.2 shows the instantaneous velocity magnitude. All simulation results show a significant amount of resolved small-scale structures at the valve shaft (**A**). These structures are transported into the combustion chamber by the mean flow, identifiable by the scattered spots in the velocity magnitude within the valve gap. Similar to the PIV, SF and SM exhibit turbulent structures directly at the separation edges of the valve ($\mathbf{B_{LV}}$, $\mathbf{B_{RV}}$). In contrast, for the SC and DES turbulent structures occur notably behind these locations.

The left of figure 4.3 illustrates the trajectory-based $Y^* - Z^*$ coordinate system, used for the investigation of the intake jet. The red dot represents the reference point for the jet centerline extraction, located on the outer edge of the valve face in the valve center plane. At this point, an evaluation line perpendicular to the valve face is constructed, which is shifted one valve lift downstream (red vector).

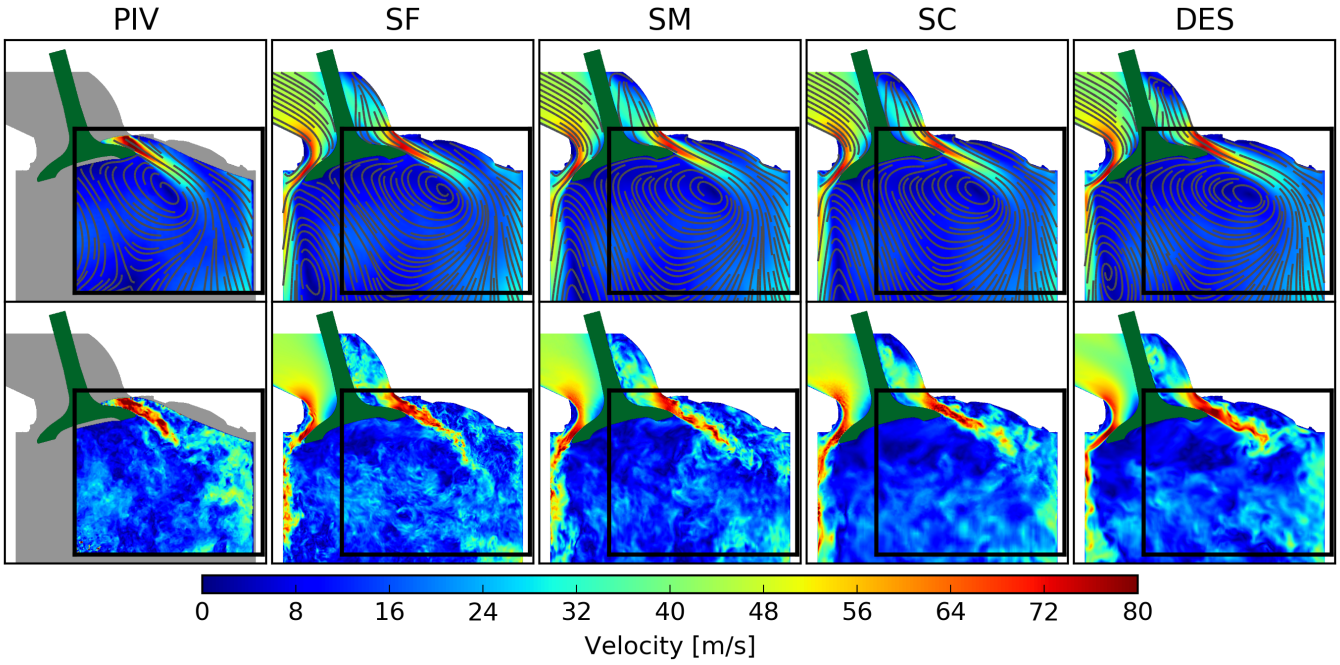

Figure 4.2: Ensemble-averaged (top row) and instantaneous (bottom row) velocity magnitude obtained by PIV and simulation on the valve middle plane. Figure adapted from [151].

The starting point of the jet centerline $\mathbf{x}_0 = \mathbf{x}(s = 0)$ is defined by the maximum velocity on this evaluation line. s represents a curved coordinate axis (adapted to the jet centerline). $\mathbf{x}$ is the two component vector which describes the position of the jet centerline on the considered plane. Beginning with the starting point, the jet centerline is integrated based on the phase-averaged velocity field according to the following equation:

$$\mathbf{x}(s) = \int_0^{\mathbf{s}} \frac{\mathbf{u}(\mathbf{x}(s^{'}))}{|\mathbf{u}(\mathbf{x}(s^{'}))|} \mathrm{d}s^{'} \,, \mathbf{x}(s) = \begin{pmatrix} Y(s) \\ Z(s) \end{pmatrix} \mathbf{u} = \begin{pmatrix} u_y \\ u_z \end{pmatrix}. \tag{4.1}$$

The downstream integration limit is $s = 30\,\mathrm{mm}$ and the upstream integration limit is $s = -10\,\mathrm{mm}$. A trajectory-based $Y^* - Z^*$ coordinate system is introduced. The $Y^* - Z^*$ plane and the $Y - Z$ plane (see left of figure 4.3) are identical to the X axis as the out-of-plane component. Y^* represents a dimensionless axis along the jet centerline, and Z^* is a dimensionless axis normally oriented to the Y^* axis (i.e. locally adapted). Both coordinates are normalized by the valve lift.

The right of figure 4.3 illustrates the jet centerline obtained by PIV and simulations. Starting at the valve gap, the jet centerlines are close together. Leaving the valve gap, the PIV exhibits a slight deflection towards the center of the cylinder, while the simulation results are curved towards the cylinder head. Apart from that, the initial intake jet is less influenced by the in-cylinder flow field, identifiable by the almost straight jet centerlines. Beginning with $Y^* \approx 3$, strong curvatures occur, which differ notably between the simulation results. The jet centerline of the DES model shows the smallest curvature, and the Sigma model shows increasing curvature with increasing spatial resolution. The intake jet obtained by SF agrees best with the PIV in terms of its position, although there are still non-negligible differences between the two results.

Figure 4.4 illustrates the ensemble-averaged velocity and the rms of the velocity fluctuations in the direction of flow along the jet centerline (Y^*). Values are normalized by a reference velocity $\mathrm{v}_{\mathrm{char}}$,

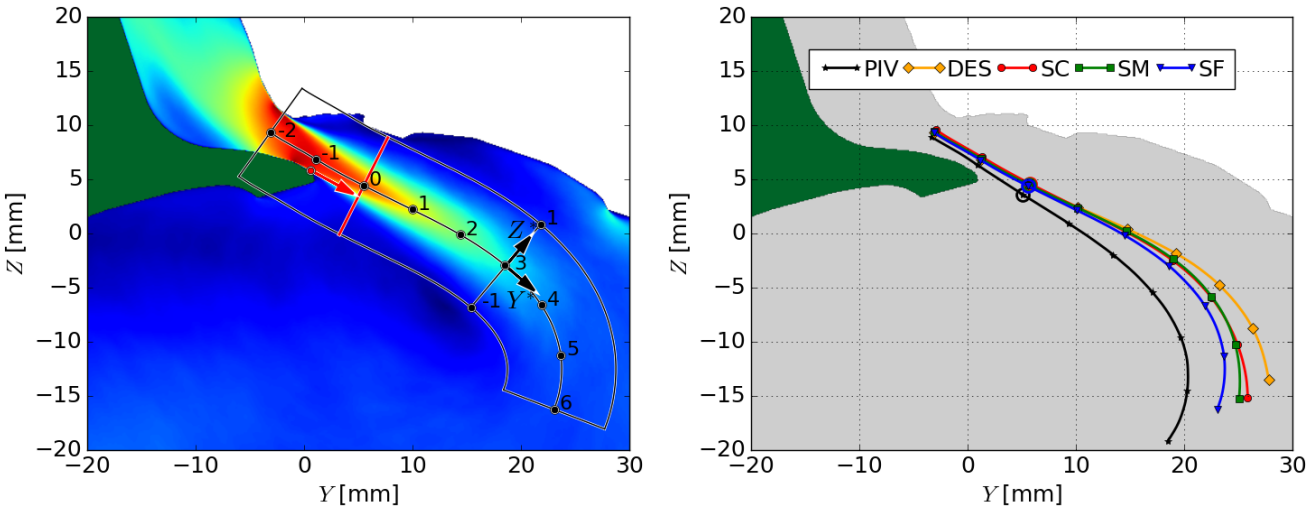

Figure 4.3: Left: Jet centerline and corresponding $Y^* - Z^*$ coordinate system. Right: Jet centerlines based on the ensemble-averaged velocity fields on the valve middle plane. Starting point ($Y^* = 0$) on each jet centerline is denoted by a circle. Symbols (e.g. squares) are distributed in intervals of $\Delta Y^* = 1$. Figure adapted from [151].

calculated from the mass flow, the density and the cross-sectional area of the two intake valves (see [151]).

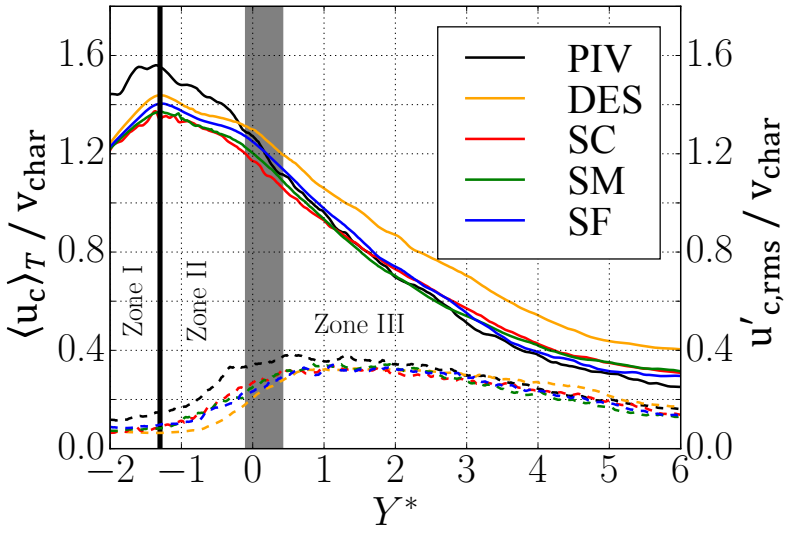

Figure 4.4: Ensemble-averaged velocity (—) and rms of velocity fluctuations (- - -) in the direction of flow along the jet centerline (Y^*). Both values are normalized by a reference velocity v_{char}, calculated from the mass flow, density and the cross-sectional area of the two intake valves. Figure taken from [138].

Three zones are defined. *Zone I* starts at $Y^* = -2$ (i.e. within the valve gap) where the fluid is accelerated. The velocity fluctuations are low and nearly constant. For all results, the maximum velocity is located at $Y^* = -1.3$, which marks the end of *Zone I*. *Zone II* is defined by a moderate (and almost linear) velocity decrease until $\langle u_c \rangle / v_{char} = 1.2$. The exact location for $\langle u_c \rangle / v_{char} = 1.2$ varies for each result around $Y^* = 0$ (gray area in figure 4.4). The velocity fluctuations increase notably in this region. *Zone III* marks the far field of the intake jet, identifiable by the stronger velocity decrease and the moderate decrease of velocity fluctuations on the jet centerline.

Similar trends are obtained for all results and the different zones are clearly identifiable. Over the entire jet centerline, the DES model shows higher values for $\langle u_c \rangle / v_{char}$ than the Sigma model (independent of the grid). In *Zone I* and *Zone II*, the PIV exhibits higher values for $\langle u_c \rangle / v_{char}$ than the simulations. These differences vanish at the beginning of the third zone. Regarding the normalized velocity fluctuations in flow direction, the highest and lowest values are obtained by the PIV and the DES model. The results of SC, SM and SF are almost identical. In *Zone III* similar results are obtained for all models.

4.1.3 Interim findings

This work investigated a quasi steady-state flow bench configuration, focusing on the flow field in the vicinity of the intake valve. The DES-SST and the Sigma turbulence models were applied on three different grids (coarse, medium and fine). The results are summarized as follows:

i) Qualitative comparison:
The ensemble-averaged flow fields are similar with differences at the exact position of the intake jet and the recirculation zone. Experiment and simulations exhibit a high level of resolved fluctuations close to the valve gap and throughout the cylinder. A higher spatial resolution leads to more resolved small-scale structures and to a more pronounced jet breakup close to the separation edge of the valve.

ii) Detailed analysis of the phase-averaged intake jet:
Differences within the valve gap amplify along the direction of flow. The curvature of the intake jet shows a high grid sensitivity and the Sigma model on the fine mesh shows best agreement to the experiment. For a more detailed comparison, the velocity fields were transformed into a local adapted coordinate system. Based on the velocity component aligned with the jet centerline, three zones were identified: acceleration, moderate velocity decrease and strong velocity decrease.

4.2 Large-scale fluctuations

An important topic in the field of ICEs is the definition and the quantification of CCVs. Typically, CCVs of global quantities (peak and mean pressure) can be identified clearly. Such definitions are less straightforward for local results based on a very limited number of cycles, as is the case for 3D-CFD. This study aims to identify large-scale structures and quantify its CCVs with respect to an ensemble average. For this reason, a heuristic approach (originally presented in [137]) is applied on in-cylinder velocity fields. This approach combines POD, previously used for the identification and investigation of velocity fluctuations [87, 94–99], and conditional averaging [100].
After an overview of the general workflow, the results obtained by the previously described simplified engine setup (section 3.2.1) are shown. The detailed workflow can be found in [137].

4.2.1 Engine setup and definition of CCVs

The study bases on a simplified engine, already described in section 3.2.1. Please note that a reduced mesh with about 8×10^6 grid points is used and the results are limited to those obtained by the SAS-SST turbulence model. A total number of 208 samples (i.e. 9 consecutive cycles while the first one is dropped) is considered. Although the terminology “CCV” is used frequently, to the author’s knowledge there is no generally accepted and unique definition. Here, the definition of CCV in terms of the velocity field within an ICE bases on the following considerations:

- Each engine cycle represents an individual process.
- For any crank angle within an engine cycle, the flow field is influenced by intrinsically (e.g. turbulence) and extrinsically (e.g. pressure waves) induced fluctuations.
- Each specific flow field bases on a less complex and unique flow topology. This flow topology is superposed with large-scale and small-scale flow structures.
- Cyclic variations of large-scale flow structures are considered as CCVs.
- Additional fluctuations (i.e. small-scale structures) exist, but are not considered as CCVs.

This means that CCVs of the velocity field are exclusively defined by the spatial and/or temporal variations of large-scale structures (e.g. the intake jet and tumble). To extract these CCVs, an ad-hoc methodology is applied, which bases on the snapshot POD method [98, 99, 152] and conditional averaging. Figure 4.5 shows the general workflow.
The starting point of this method is the fact that the high-energetic POD modes are linked to high-energetic flow structures (e.g. the intake jet) [56, 97, 99]. CCVs of these flow structures are reflected by a variation of the first POD coefficients. These coefficients are used to cluster the instantaneous cycles into subsets. As a result, each subset is characterized by a fundamental flow structure, similar for all instantaneous cycles within this subset. The deviation of the subset average to the ensemble average represents large-scale CCVs. For a mathematical description see section 2.4 or [137].

4.2.2 Results

Figure 4.6 shows the first POD modes (each normalized by its maximum value) resulting from the velocity field at −310 °CA.

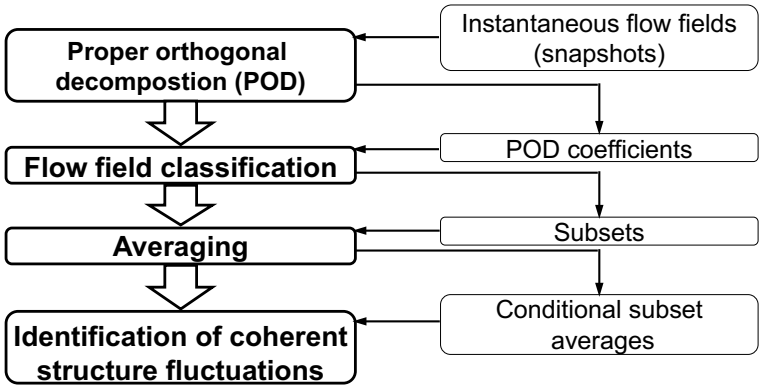

Figure 4.5: General workflow to calculate conditional averages and large-scale fluctuations in context of ICEs at a specified crank angle. Figure taken from [137].

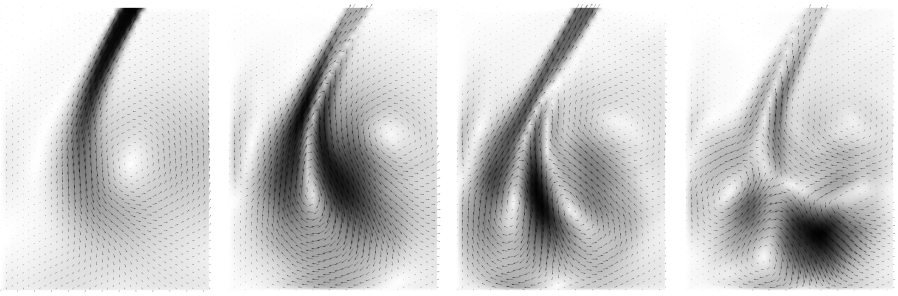

(a) Mode 1 **(b)** Mode 2 **(c)** Mode 3 **(d)** Mode 4

Figure 4.6: POD modes 1 to 4 (each normalized by its maximum value) resulting from the velocity field at −310 °CA of the simplified engine setup. Figure taken from [137].

As mentioned in previous investigations [56, 81, 87, 96–98], a similarity between the first POD mode (figure 4.6a) and the ensemble-averaged velocity field (figure 4.8a) exists. Due to the dominant structures, it can be assumed that especially the second and third modes are connected to the intake jet and large-scale vortex. In contrast, an interpretation of the forth mode is more difficult.
In a next step, the POD coefficients are used to group the instantaneous flow fields into different subsets. Here, the following observations are taken into account:

- For most of the intake stroke, the singular values of the first and second modes are high compared to those of the higher modes (see [137]).
- Mode 1 is associated to the ensemble-averaged velocity field.
- Modes 2 and 3 are associated to the dynamics of the intake jet and the large-scale tumble structure (see figure 4.6).
- The POD coefficient of the first mode is almost constant and thus less useful for a classification (see figure 4.7).
- The other POD coefficients show variations and are suitable for a clustering (see figure 4.7).

Furthermore, it is important to find a compromise between the number of subsets and the samples within each subset. Due to these reasons, a total number of four subsets is chosen, which base on the coefficients of the second and third POD modes (see table 4.1). Beside the classification criteria, table 4.1 shows the number of instantaneous velocity fields clustered into each subset.

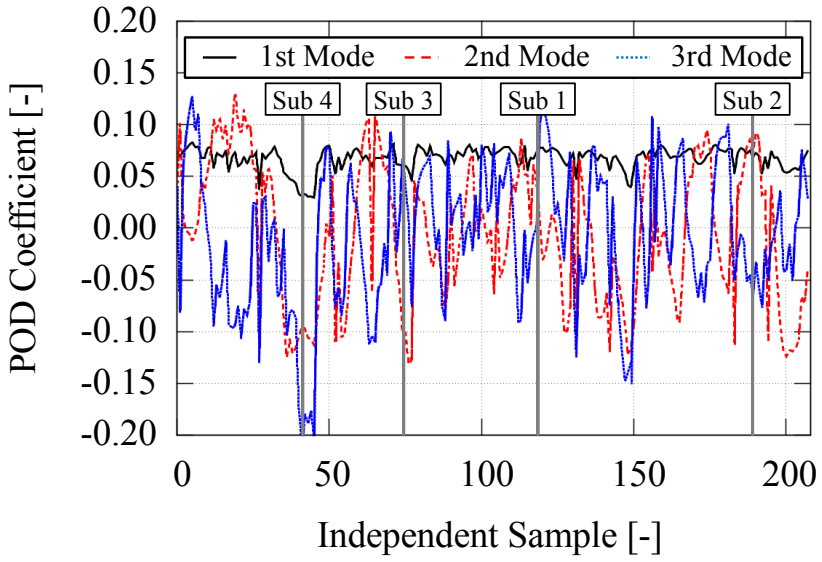

Figure 4.7: POD coefficients of first, second and third modes. Vertical lines illustrate a single example for each classification criteria. Figure adapted from [137].

Table 4.1: Subset classification based on the coefficients of the second POD mode and the third POD mode at −310 °CA. Number of samples within the subsets are shown in the last column.

Subset	Coefficient mode 2	Coefficient mode 3	Number of samples
1	≥ 0	≥ 0	36
2	≥ 0	< 0	65
3	< 0	≥ 0	64
4	< 0	< 0	43

Figure 4.8 shows the ensemble average and the subset averages (obtained by the instantaneous velocity fields within an individual subset) at −310 °CA. All results exhibit a similar flow topology, characterized by an intake jet and a tumble-like vortex structure. An explicit comparison of the obtained fields is illustrated in figure 4.8f by means of velocity isolines (intake jet 6 m/s; vortex structure 1 m/s). Close to the valve gap, there is a strong influence of the wall on the flow, and the intake jet is identical for all the averages. In contrast, a clear variation of the jet direction and its penetration depth exists within the combustion chamber.

Compared to the ensemble average, the first and third subset averages show an increased penetration depth, while the second and forth show a larger deviation with respect to the jet direction. With exception of the first, each subset average shows a clear variation of the vortex core position compared to the ensemble average. It is interesting to see that the vortex core position is linked to the position of the intake jet. Considering the second subset, the intake jet exhibits the most significant bending, while the corresponding vortex core is shifted significantly towards the cylinder axis.

Figure 4.9a shows the rms of the velocity fluctuations calculated by the ensemble-averaged and by the total number of instantaneous velocity fields according to equation (2.23).

The velocity fluctuations are observed in a well-defined and thin shear layer generated by the intake jet close to the valve gap and rapidly spreading out with increasing penetration depth. Figures 4.9b to e

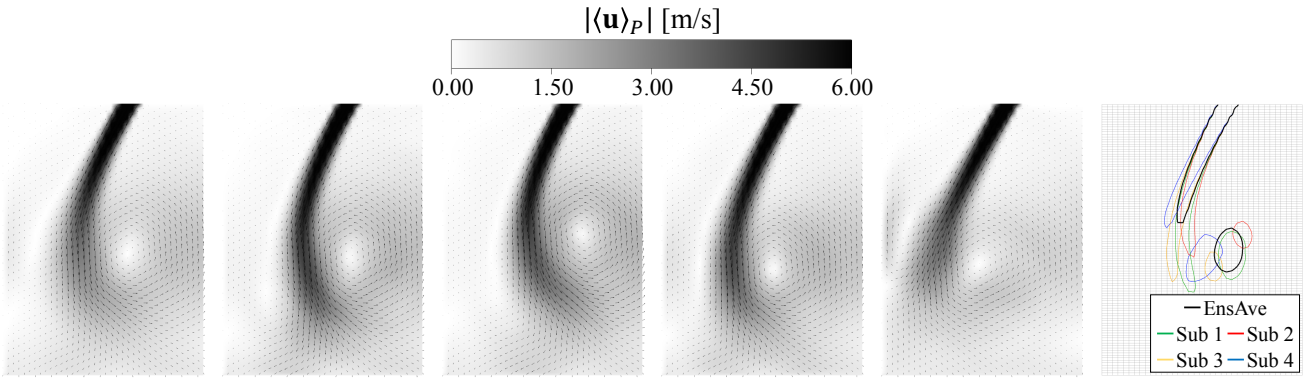

(a) EnsAve **(b)** Sub 1 **(c)** Sub 2 **(d)** Sub 3 **(e)** Sub 4 **(f)** All

Figure 4.8: Ensemble average (a) and subset averages (b-e) at $-310\,°\mathrm{CA}$. Comparison of results using velocity isolines ($6\,\mathrm{m\,s^{-1}}$ for the intake jet and $1\,\mathrm{m\,s^{-1}}$ for the vortex core) in f. Figure adapted from [137].

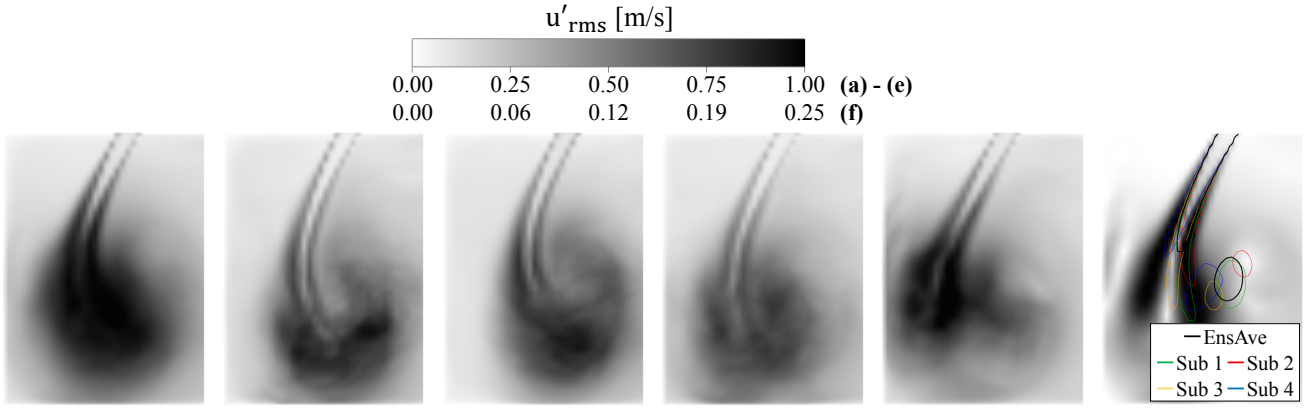

(a) $\mathrm{rms}_{\mathrm{EnsAve}}$ **(b)** $\mathrm{rms}_{\mathrm{Sub1}}$ **(c)** $\mathrm{rms}_{\mathrm{Sub2}}$ **(d)** $\mathrm{rms}_{\mathrm{Sub3}}$ **(e)** $\mathrm{rms}_{\mathrm{Sub4}}$ **(f)** $\mathrm{rms}_{\mathrm{CCV}}$

Figure 4.9: Root mean square of velocity fluctuations calculated by equation 2.23 (a), by equation 2.29 (b-e) and by equation 2.30 (f) at $-310\,°\mathrm{CA}$. Isolines defined as in figure 4.8. Figure adapted from [137].

show the rms calculated instantaneous velocity fields within the subsets (equation (2.29)). Similar to figure 4.9a, each subset exhibits very narrow regions of velocity fluctuations in the vicinity of the valve gap. This concentration to the shear layer region of the corresponding intake jet is preserved up close to the cylinder liner and piston, where an increased level of velocity fluctuations indicates the final jet breakup. This well-defined structure of velocity fluctuations indicates that the subset averages are a good approximation to the fundamental flow topology representative for the corresponding instantaneous velocity fields. Figure 4.9f shows the large-scale fluctuations (equation (2.30)), which represent the CCV as defined in section 4.2.1. It is interesting to see that the general structure of large-scale fluctuations looks very similar to the second POD mode. Another interesting observation is the occurrence of the narrow region bounded by the high rms values, which marks an overlap between all the subset averages and the ensemble average.

An identical analysis was performed based on the well-known TCC engine [153]. The results obtained by this realistic 4-stroke engine setup are similar to those obtained by the simplified engine. Both are presented in [137].

4.2.3 Interim findings

A new ad-hoc methodology to identify and quantify CCVs in ICEs was proposed. The general idea is to identify the large-scale structures and quantify their deviation to the ensemble average. For this, the instantaneous flow fields are grouped into subsets with the aim to average and to calculate a large- and a small-scale contribution to the total fluctuations. The difference of the subset average to the ensemble average is denoted as large-scale fluctuation (i.e. CCV), while the differences between the instantaneous velocity fields within an individual subset are denoted as small-scale fluctuations. The results are summarized as follows:

i) Proper orthogonal decomposition:
   As mentioned in previous investigations, the first POD mode is very similar to the ensemble-averaged velocity field. The interpretation of higher modes is more difficult.

ii) Ensemble and subset averages:
   A total number of 4 subsets was chosen, which base on the coefficient of the second and third POD modes, representing a compromise between the number of subsets and the number of snapshots within each subset. All averages show a similar structure in general, consisting of an intake jet and a tumble-like vortex structure in the center of the cylinder. The orientation and penetration depth of the intake jet differs from result to result. Furthermore, a variation of the vortex core position was detected.

iii) Quantification of CCVs and small-scale fluctuations:
   The quantification of CCVs was based on the deviations between the subset and ensemble averages. The structure of CCVs is very similar to those of the second POD mode. Small-scale structures occur in regions where high turbulent fluctuations are expected, e.g. in the high shear region of the jet.

4.3 Tumble structure development during the intake stroke

In recent years, much research has focused on the large-scale tumble structure [51, 81, 87–92]. However, most of these investigations are limited to a 2D evaluation on certain in-cylinder planes, and thus, there remains a lack of knowledge in terms of the full 3D tumble structure. For this reason, this work visualizes the 3D tumble structures during the intake stroke based on highly resolved simulations of an experimental single stroke engine [101]. In addition, the interaction between the tumble and the piston boundary layer is analyzed. These and further results (e.g. angular velocity of the tumble) can be found in [137].

4.3.1 Engine and numerical setup

The setup bases on a modern gasoline cylinder-head and operates in a single stroke mode (stroke referred as "cycle" in the following), representing an engine speed of 960 rpm at full load operation condition. Each cycle starts at −360 °CA with slightly opened intake valves (0.6 mm) and a clearance height of 7 mm between the piston and the dome. Reaching BDC (i.e. −180 °CA), the piston motion and intake valve motion are stopped and a subsequent time period of 100 °CA is analyzed, resulting into 280 °CA for an individual cycle. It has to be noted that each cycle is independent of the previous ones since it starts from a quiescent initial state (i.e. zero velocity). Due to the limitation to the intake stroke and the experimental setup (i.e. water as working fluid), an incompressible approach is sufficient for this case. Similar to the SPP strategy (section 3.1), the inlet is placed upstream of the flow split, and the corresponding boundary condition consists of an averaged flow rate (section 4.2) superposed by synthetic fluctuations [145].

The applied hybrid mesh consists of tetrahedral, prismatic and hexahedral elements with a maximum and minimum cell size of 1 mm and 0.25 mm, respectively. Normal to the piston surface, 55 prism layers with a total height of 2 mm (first layer height 5 μm) are used to ensure a high resolution of the wall boundary layer (i.e. $y^+ < 1$) for the entire simulation time. For remaining surfaces, 15 prism layers are applied. This leads to a total number of up to 34.3×10^6 nodes. To ensure a sufficient temporal resolution (i.e. CFL < 1) for the entire simulation domain, the time step width is adapted to the piston speed. Starting with 0.05 °CA, it reaches a minimum value of 0.025 °CA at −270 °CA. A central differencing scheme in space and a second-order backward scheme in time are used to minimize numerical diffusion. The scale adaptive simulation (SAS-SST) turbulence model (section 2.2) is chosen. In total, 30 realizations are available.

4.3.2 Results

Figure 4.10a shows the resolved turbulent structures of an individual cycle, visualized by the Q-criterion (Q=1000 s^{-2}) [154].

Due to the "stable flow" [155] within the intake port, only a small amount of resolved turbulence exists. Behind the valve shaft and the separation edge, the SAS-SST model is triggered into an LES-like mode, which is confirmed by the significant number of resolved small-scale structures in the valve gap region and throughout the combustion chamber. These turbulent structures are colored by the viscosity ratio (μ_t/μ). The observed values are typical for scale-resolving engine simulations [64]. Figure 4.10b and figure 4.10c illustrate the phase-averaged velocity in two cross sections. The orientation of the intake

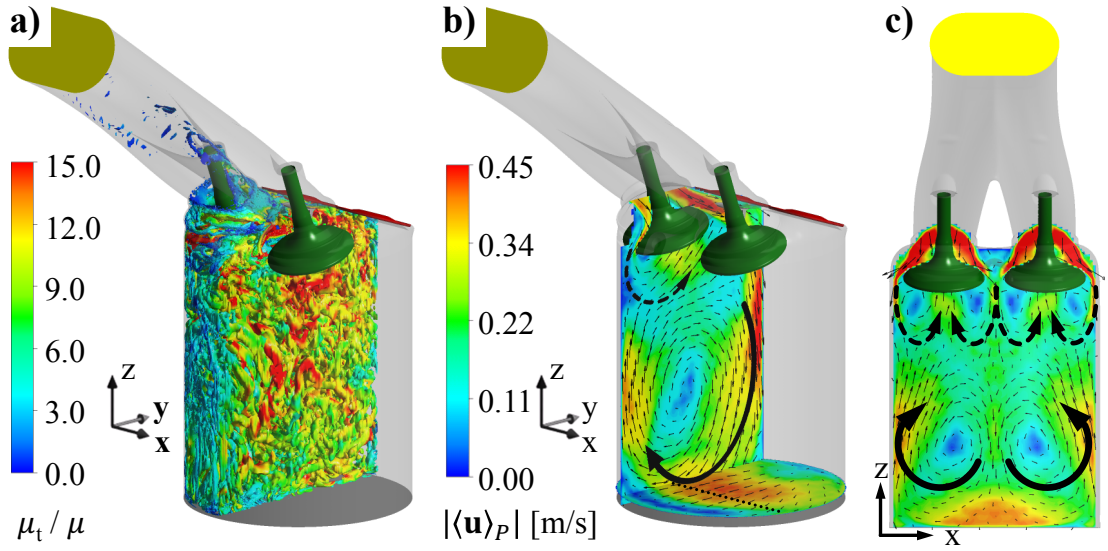

Figure 4.10: a) Turbulent structures at −200 °CA, visualized by Q-criterion and colored by viscosity ratio. b) Phase-averaged velocity magnitude $|\langle \mathbf{u} \rangle_P|$ on valve middle plane and 3.5 mm above piston. c) $|\langle \mathbf{u} \rangle_P|$ on a y-normal plane (indicated by the dotted line in b). Figure adapted from [138].

port and the separation edge upstream of the intake valve lead to a well defined intake jet, which is deflected by the cylinder liner and the piston surface (identifiable by regions with increased velocity magnitude). The resulting tumble structure (indicated by black arrows) characterizes the flow within the combustion chamber in the second half of the intake stroke.

Next, the rotation center of the in-cylinder charge motion (i.e. the tumble center) is detected by the $\mathbf{\Gamma}_{3p}$ criterion (introduced and described in detail in [138]). It is defined as

$$\mathbf{\Gamma}_{3p}(\mathbf{x}, \varphi) = \frac{1}{V(\mathbf{x}, \varphi)} \int\limits_{\mathbf{x}_o \in V} \frac{\mathbf{r}_p(\mathbf{x}_o) \times \mathbf{u}_p(\mathbf{x}_o, \varphi)}{\|\mathbf{r}_p(\mathbf{x}_o)\| \|\hat{\mathbf{u}}(\mathbf{x}_o, \varphi))\|} d\mathbf{x}_o \,. \tag{4.2}$$

with $\hat{\mathbf{u}}(\mathbf{x}_o, \varphi) = \mathbf{u}(\mathbf{x}_o, \varphi) - \langle \mathbf{u} \rangle_V(\mathbf{x}, \varphi)$. $V(\mathbf{x}, \varphi)$ represents a rectangular subvolume with an edge length of 24 mm and the point $\mathbf{x}$ as centroid. Depending on the spatial position and the considered crank angle, each edge of $V(\mathbf{x}, \varphi)$ can be reduced to a minimum length of 6 mm (independent from the other edges). On the one hand, this adaption allows a calculation of $\mathbf{\Gamma}_{3p}$ until close to the cylinder liner. On the other, as much volume as possible (up to the defined limit) is used for the calculation, which improves the robustness and the reliability of the detection method. The velocity vector $\mathbf{u}_p(\mathbf{x}_0, \varphi)$ and the position vector $\mathbf{r}_p(\mathbf{x}_o)$ are defined as

$$\mathbf{u}_p(\mathbf{x}_o, \varphi) = \hat{\mathbf{u}}(\mathbf{x}_o, \varphi) - \mathbf{e}_{\Gamma_3}(\mathbf{x}, \varphi) \cdot (\hat{\mathbf{u}}(\mathbf{x}_o, \varphi) \cdot \mathbf{e}_{\Gamma_3}(\mathbf{x}, \varphi)) \,. \tag{4.3}$$

and

$$\mathbf{r}_p(\mathbf{x}_o) = \mathbf{r}(\mathbf{x}_o) - \mathbf{e}_{\Gamma_3}(\mathbf{x}, \varphi) \cdot (\mathbf{r}(\mathbf{x}_o) \cdot \mathbf{e}_{\Gamma_3}(\mathbf{x}, \varphi)) \tag{4.4}$$

with $\mathbf{r}(\mathbf{x}_o)$ being the distance vector between $\mathbf{x}$ and $\mathbf{x}_o$ (both within V). The unit vector $\mathbf{e}_{\mathbf{\Gamma}_3}$ is calculated as

$$\mathbf{e}_{\mathbf{\Gamma}_3}(\mathbf{x},\varphi) = \frac{\mathbf{\Gamma}_3(\mathbf{x},\varphi)}{\|\mathbf{\Gamma}_3(\mathbf{x},\varphi)\|} \tag{4.5}$$

and bases on

$$\mathbf{\Gamma}_3(\mathbf{x},\varphi) = \frac{1}{V(\mathbf{x},\varphi)} \int\limits_{\mathbf{x}_o \in V} \frac{\mathbf{r}(\mathbf{x}_o) \times \hat{\mathbf{u}}(\mathbf{x}_o,\varphi)}{\|\mathbf{r}(\mathbf{x}_o)\| \|\hat{\mathbf{u}}(\mathbf{x}_o,\varphi)\|} d\mathbf{x}_o \,, \tag{4.6}$$

which was originally presented in [156, 157].
Considering an axisymmetric and uncurved vortex structure, its rotation axis is represented by a trajectory tangential to the vectors for which $|\mathbf{\Gamma}_{3p}(\mathbf{x},\varphi)| = 1$ is valid. In contrast, $|\mathbf{\Gamma}_{3p}| = 0$ means that no rotation appears. In this thesis, the TC of an IC engine is represented by exactly the trajectory which includes the maximum magnitude for $\mathbf{\Gamma}_{3p}(\mathbf{x},\varphi)$ on the symmetry plane (i.e. $\max(|\mathbf{\Gamma}_{3p}(\mathrm{x}=0,\mathrm{y},\mathrm{z},\varphi)|) = \mathbf{\Gamma}_{3p}(\mathrm{x}=0,\mathrm{y_{TC}},\mathrm{z_{TC}},\varphi)$ with $\mathrm{y_{TC}}$ and $\mathrm{z_{TC}}$ as tumble center coordinates). The results are presented in figure 4.11, where the phase-averaged and the cycle-individual TC are shown.

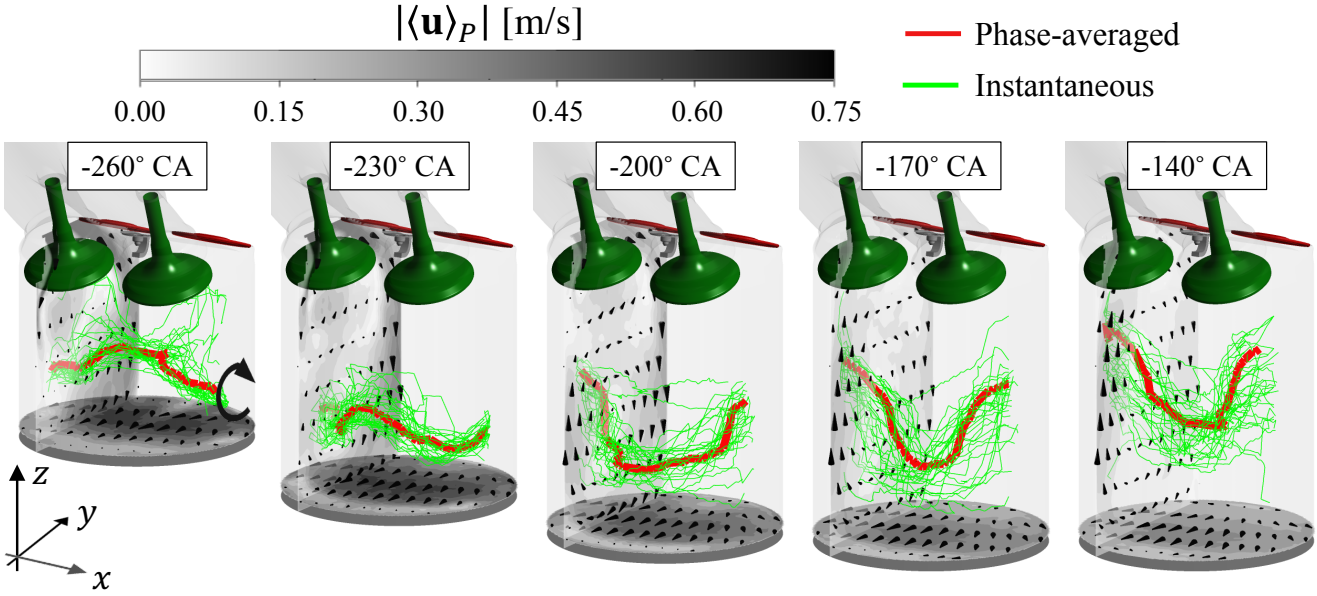

Figure 4.11: Phase-averaged and instantaneous tumble center, detected by the $\mathbf{\Gamma}_{3p}$ criterion. Phase-averaged velocity magnitudes 3.5 mm above the piston and on the valve middle plane. Figure adapted from [138].

Starting with −260 °CA, a cyclic variation of the TC (also known as PVC) occurs. With regard to the selected planes, the PVC was also identified in previous investigations [51, 81, 87]. During the entire intake stroke and even in the phase when the piston remains in its lowest position, a significant movement of the TC can be observed. Considering the valve middle plane, the TC starts next to the intake valves and moves against the main flow direction towards the piston surface until −160 °CA. Afterwards, there is a movement towards the cylinder head. Up to −200 °CA the TC is highly deformed ("w-shaped"),

while a less complex structure ("v-shaped") is observed from −170 °CA onwards. An analysis of the phase-averaged tumble structure in terms of its angular velocity figured out a strong variance of the angular velocity along the TC line (shown in [138]). Regions directly affected by the intake jet (next to the valve middle plane) exhibit a high angular velocity while smaller values are obtained close to the symmetry plane. This variance vanishes with a declining intake jet (i.e. at the end of the piston motion).

Figure 4.12 illustrates the flow field and the boundary layer profile exemplary at −200 °CA in two different cross sections. In region **A** the tumble structure is deflected by the piston surface, leading to a flow topology similar to a stagnation point. A flow almost parallel to the wall exists at positions **P1** and **P3** and a constantly thin boundary layer is observed (height of the viscous sublayer less than 0.1 mm). In region **B** the tumble is redirected towards the cylinder head, and the boundary layer height increases significantly. At later crank angles, the boundary layer thickness increases, while its general structure is maintained. This increase can be traced back to the decreasing angular velocity of the tumble (see [138]) and its reduced interaction with the piston, due to the upward motion of the tumble (see figure 4.11).

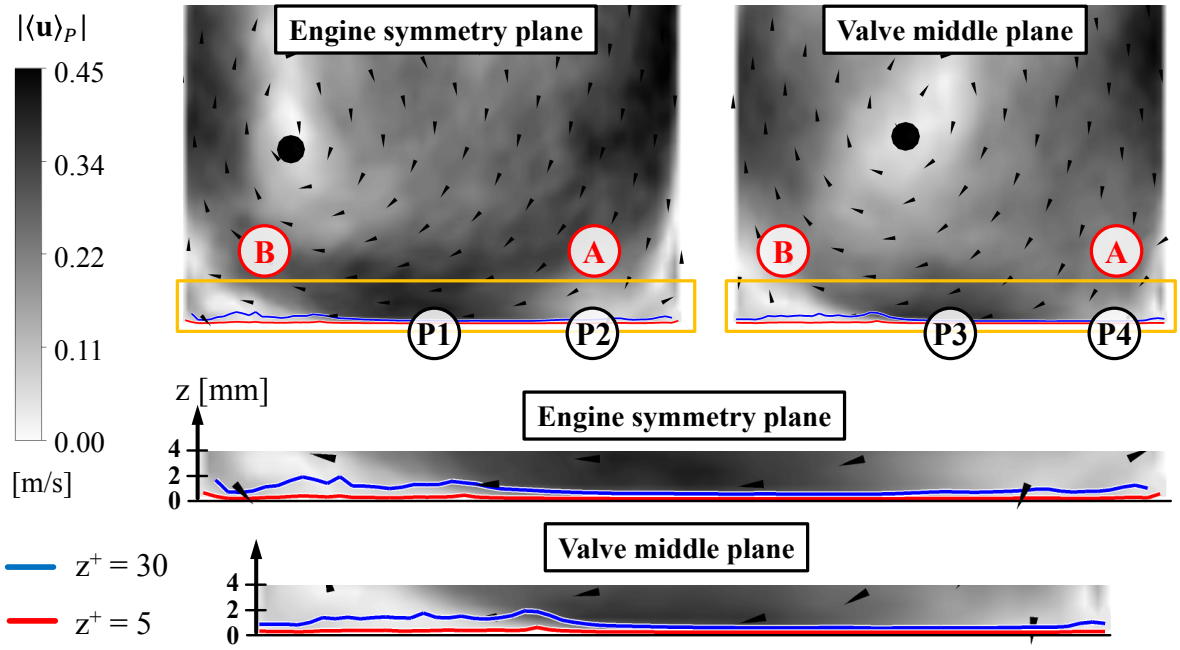

Figure 4.12: Velocity magnitude on the engine symmetry plane and the valve middle plane at −200 °CA. P1 - P4 indicate locations where dimensionless velocity profiles are evaluated (see figure 4.13). Regions marked by orange boxes are enlarged and illustrated in the lower part. The red and blue lines represent the $z^+ = 5$ and $z^+ = 30$ isosurfaces. Black dots mark the local tumble center. Figure adapted from [138].

Figure 4.13 shows the phase-averaged dimensionless piston boundary layer profiles at −260°, −200° and −140 °CA. The profiles are evaluated at positions **P1** - **P4**, illustrated in figure 4.12. For comparison purposes, the classical boundary layer assumption (CBLA) [18] (red dashed line) is shown, being the basis for many wall model formulations. **P2** and **P4** are in the stagnation point region with significant normal velocity components, see figure 4.12. **P1** and **P3** are in a region with a flow mostly parallel to the wall. For all averaged profiles, comparable results are obtained up to $z^+ \approx 5$. With increasing z^+ values, the dimensionless velocity profiles exhibit larger deviations and no agreement with the log-formulation of the CBLA is found. This is consistent with observations in [26, 107] and [86], confirming that no

turbulent equilibrium boundary layer exists at the piston surface. Interestingly, the results for **P1** and **P3** are closer to the CBLA, while the profiles for **P2** and **P4** show the largest discrepancies.

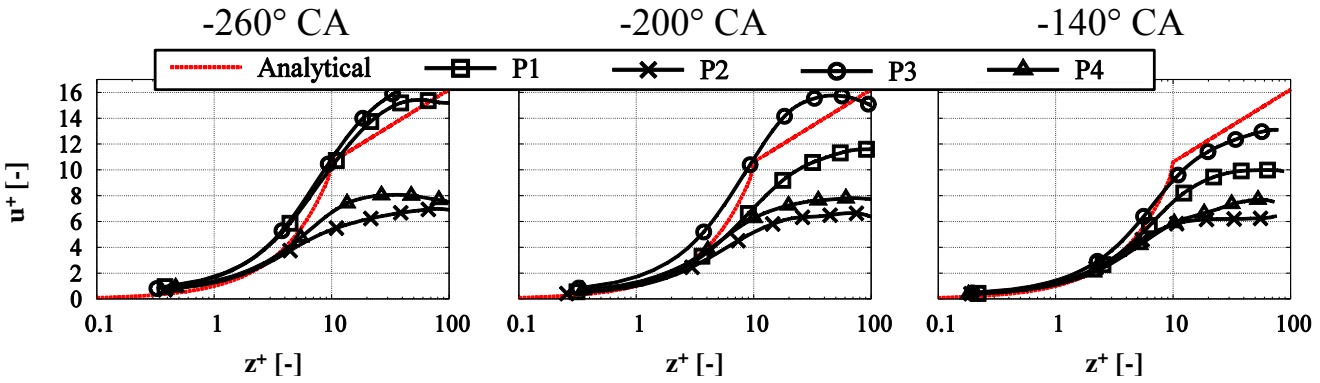

Figure 4.13: Phase-averaged dimensionless velocity profiles at P1 - P4 (see figure 4.12). In addition, the velocity profile from the classical boundary layer assumption is shown for reference. Figure taken from [138].

4.3.3 Interim conclusion

This work investigated the generation of the large-scale tumble structure and its interaction with the piston boundary layer. In the following, the results are summarized:

i) Generation of large-scale tumble:
The TC and its movement during the investigated time period was visualized. A complex "w-shape" structure in the early phase and a less complex "v-shape" structure were obtained for the TC. Based on the available multi-cycle numerical data, significant CCVs of the entire 3D-tumble structure were found.

ii) Interaction with piston boundary layer:
The piston boundary layer was investigated based on a highly resolved mesh and the thickness of the boundary layer (based on specified values for y^+) was computed. It was shown that the boundary layer thickness varies strongly along the piston surface. This was connected to the interaction with the tumble flow structure, which leads to regions with stagnation points and wall-parallel flows in the vicinity of the piston surface. The dimensionless velocity profiles at specified locations were calculated, and significant deviations from the classical boundary layer profile could be identified.

4.4 Tumble structure development during compression stroke

Although the technical terms “tumble” and “tumble breakdown” are frequently used in the IC engine community, the current literature is mostly limited to a phenomenological point of view. In this section, the tumble structure during the compression stroke is analyzed with the aim to get more information and a deeper insight. To do so, two well-known experimental engine setups [82, 102] are considered by means of

- the phase-averaged velocity field,
- the development of the phase-averaged TC position and its CCV,
- the development of the phase-averaged tumble intensity (TI) and its CCV and
- an evaluation of integral quantities.

Please note that these results are not published yet and represent an enhancement of the previous investigations.

4.4.1 Engine and numerical setup

At first, an overview of the investigated engines is given. Figure 4.14 illustrates their cylinder head geometries. The top row shows the “wall-guided” (WG) engine, already described in section 3.1. Here, a side mounted injector (placed between the intake valves) is used, oriented towards the centrally mounted spark plug. The “spray-guided” (SG) engine (bottom row) is a derivative of the WG engine. Its injector is placed close to the cylinder axis. Another important aspect is the modification of the intake system, especially at the intake valves (smaller diameter of the valve disks) and at the lower intake port in close vicinity to the valves (elimination of the separation edges). [84, 102] provide a detailed description of the SG engine.
Both engines are identical in terms of their global parameters, like bore and stroke, and run under identical boundary conditions (e.g. motored at 800 rpm, same cooling temperature and ambient pressure). For modeling and simulation, the SPT approach (described in section 3.1) is applied. The most important facts in terms of the simulation are summarized as follows:

- Compressible approach of the governing equations; i.e. equations (2.1) to (2.6)
- Usage of the scale-adaptive simulation model (see section 2.2)
- Same mesh topology and parameters as specified in section 3.1
- Generation of the necessary time resolved boundary conditions is done as described in section 3.1

For reasonable statistics, a total number of 100 (50) consecutive cycles were simulated for the WG (SG) engine setup. Please note that the higher number of consecutive cycles in case of the WG engine raises the expectation of an improved quality in terms of the results (compared to the SG engine).

4.4.2 Results

In order to get a first impression of the general in-cylinder flow structure, figure 4.15 shows the phase-averaged velocity vectors and magnitude on the engine symmetry plane during the compression stroke.

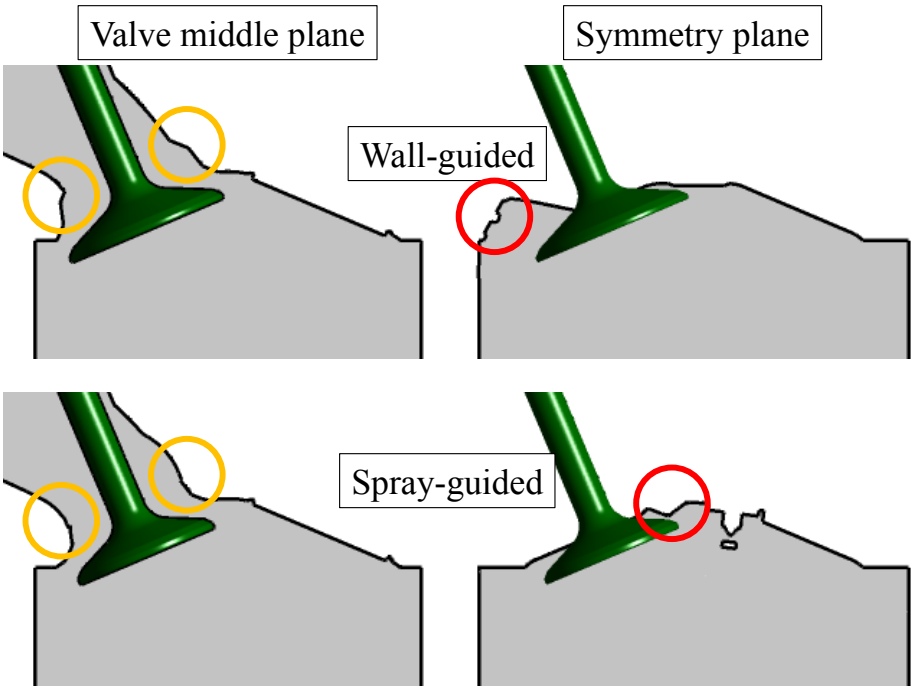

Figure 4.14: Lower part of the intake port and cylinder head for wall-guided and spray-guided engine setup. Most significant differences between the engines concern the diameter of the intake valve disk, the intake port in vicinity of the valves (orange circles) and the position of the injector (red circle).

Both engines exhibit a significant rotational in-cylinder charge motion (i.e. tumble) for all illustrated crank angle. The velocity field obtained by the WG engine is structured. The SG engine at −180 and −150 °CA exhibits some "stagnation point like" topologies in the upper part of the combustion chamber. It is interesting to see that the location of the TC (i.e. center of the rotational charge motion) notably differs for both engines, although there are only limited differences in terms of the engine geometries. After −60 °CA, it becomes challenging to interpret the velocity field due to its more complex topology. The velocity magnitude shows even greater discrepancies. For all considered crank angle, the values of the WG engine are larger than the values of the SG engine. This is particularly true for the early (−180 to −150 °CA) and the late (after −60 °CA) compression stroke. For these phases, the WG engine exhibits a maximum velocity magnitude of more than $10\,\mathrm{m\,s^{-1}}$, while the SG engine reaches about $7\,\mathrm{m\,s^{-1}}$.

In a next step, the tumble structure is analyzed. The TC is detected based on the vectorial quantity $\mathbf{\Gamma 1}_{3p}$. It represents a variation of $\mathbf{\Gamma}_{3p}$ (see section 4.3) and bases on the same set of equations. As a slight modification $\hat{\mathbf{u}}(\mathbf{x}_o, \varphi)$ is replaced by $\mathbf{u}(\mathbf{x}_o, \varphi)$. This leads to great advantages with regard to computational demands and robustness. A disadvantage of this approach is that it does not take into account the relative velocity of the tumble center and therefore it is not Galilei invariant. This leads to a discrepancy in terms of the exact tumble center position for cases when the tumble is transported by convection and its relative velocity is large compared to its rotational speed [158]. However, due to the lack of convection (from a macroscopic point of view), it can be expected that the effect of the Galilei invariance becomes small or even negligible during an ICE compression stroke. The left-hand side of figure 4.16 illustrates TC calculated by $\mathbf{\Gamma 1}_{3p}$ (blue; not Galilei invarinat) and $\mathbf{\Gamma}_{3p}$ (orange; Galilei invarinat). The largest deviation between both approaches occurs at −180 °CA, where a mass flow into the combustion chamber exists (i.e. before IVC) [137]. For phases with closed intake valves, the results

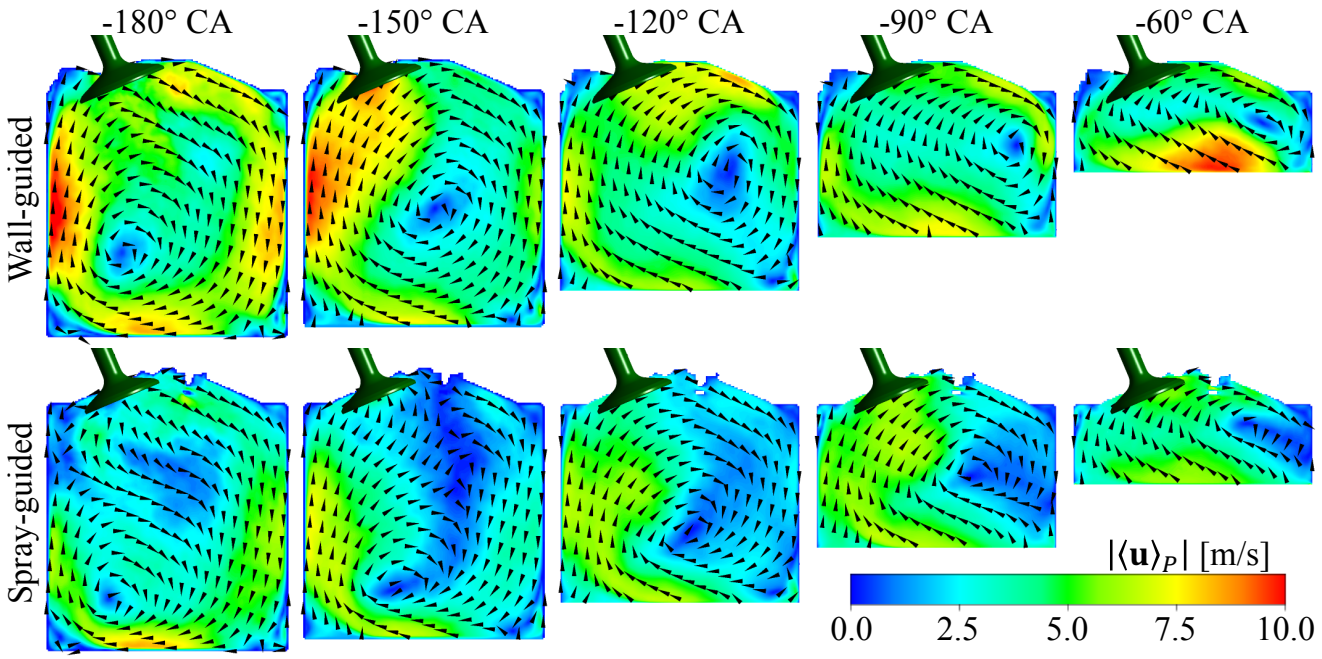

Figure 4.15: Phase-averaged velocity vectors and velocity magnitude on engine symmetry plane for WG engine (top row) and SG engine (bottom row).

obtained by both approaches are quasi identical. This is also true for crank angle with high piston speeds, like −90 °CA. Because of the previously mentioned advantages and the small deviation in terms of the position, the $\mathbf{\Gamma 1}_{3p}$ approach is used in the following.

The following investigations (e.g. in terms of the TI) focus on the "core region" of the large-scale tumble structure. For this, evaluation planes are defined, which are distributed with a distance of 1 mm in x direction along the TC. These evaluation planes use the tangent on the local tumble center line as normal vectors and have a radius of 3 mm. The right of figure 4.16 demonstrates the principle arrangement of the evaluation planes.

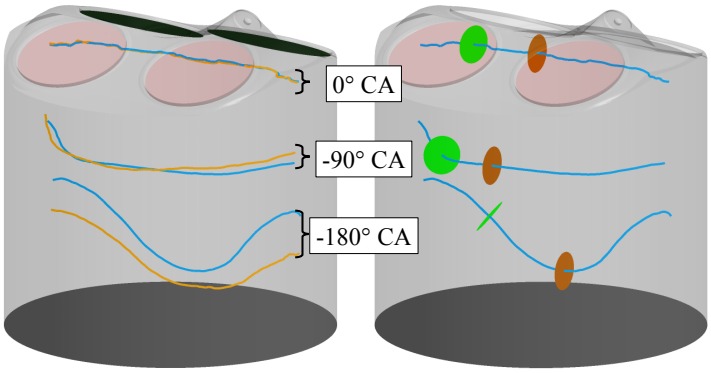

Figure 4.16: Left: Phase-averaged tumble center calculated by $\mathbf{\Gamma 1}_{3p}$ (blue) and $\mathbf{\Gamma}_{3p}$ (orange). Right: Principle arrangement of evaluation planes (exemplarily shown for $\mathbf{x} = 0$ and $\mathbf{x} = 20\,\mathrm{mm}$; brown and green) along the tumble center.

To gain an initial impression, the phase-averaged and instantaneous TC positions during the compression stroke are considered next. The temporal development of the phase-averaged TC is illustrated in figure 4.17.

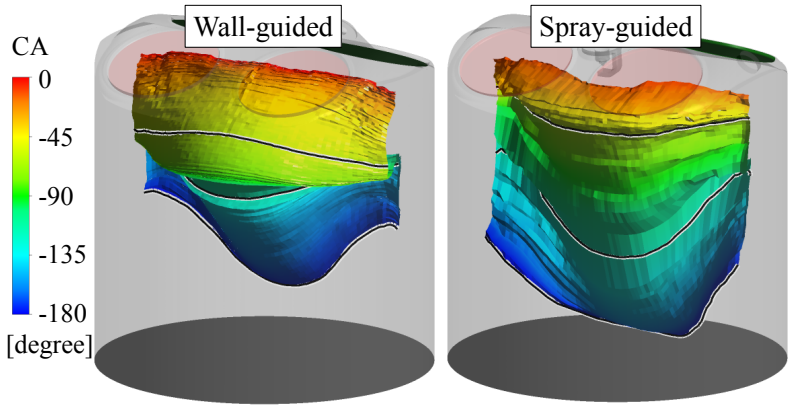

Figure 4.17: Temporal development of the phase-averaged tumble center during the compression stroke. Black lines indicate the tumble center at −180°, −120° and −60 °CA. The engine geometry is fixed at −110 °CA.

Both engines start with a strongly deformed tumble structure in the lower half of the combustion chamber. Due to the upwards motion of the piston, the TC is pushed towards the cylinder head. This movement is accompanied by a continuous deformation of the tumble. As already assumed by means of figure 4.15, there are clear differences between both engines. Considering −180 °CA, the tumble structure obtained by the SG engine is located notably closer to the piston than this is the case for the WG engine. Starting from this initial position, the TC of the SG engine exhibits a continuous rotation and movement towards the cylinder head. In contrast, a fast reorientation and movement towards the cylinder head at the beginning of the compression stroke (i.e. at less than 45 °CA) is observed for the WG engine. This is followed by a moderate upwards movement of the tumble. The differences between the engines with regard to the TC position become smaller shortly before fTDC.

Figure 4.18 shows the phase-averaged TC and the corresponding instantaneous results at various crank angle. Both engines exhibit a “v-shaped” tumble structure at −180 °CA. Consistent to section 4.3, this deformation lies in a plane approximately perpendicular to the piston crown. During the compression stroke, the TC changes its orientation and twists in such a way that the deformation lies in a plane almost parallel to the piston crown. However, there are differences between both engines concerning the exact shape and orientation of the phase-averaged TC. Shortly before fTDC, the TC is moved towards the cylinder head and the “v-shape” becomes less pronounced. Finally, the tumble is pushed into the roof-shaped compression volume and the TC becomes an almost straight line.

Both engines evince a distinctive cyclic variability, indicated by the scattering of the instantaneous results with a different intensity. Considering −180 °CA, the instantaneous results of the SG engine are strongly clustered (apart from a few exceptions), while the WG engine exhibits a higher spreading. This clustering vanishes until −120°, and no significant differences between the engines occur at this point in time. At −60 °CA, the SG engine shows higher CCVs compared to the WG engine. There are again no substantial differences at 0 °CA.

To gain a more quantitative statement, the CCVs in terms of the TC position are evaluated. For this, $\langle d \rangle_{P,Norm}$ is introduced, which is defined as

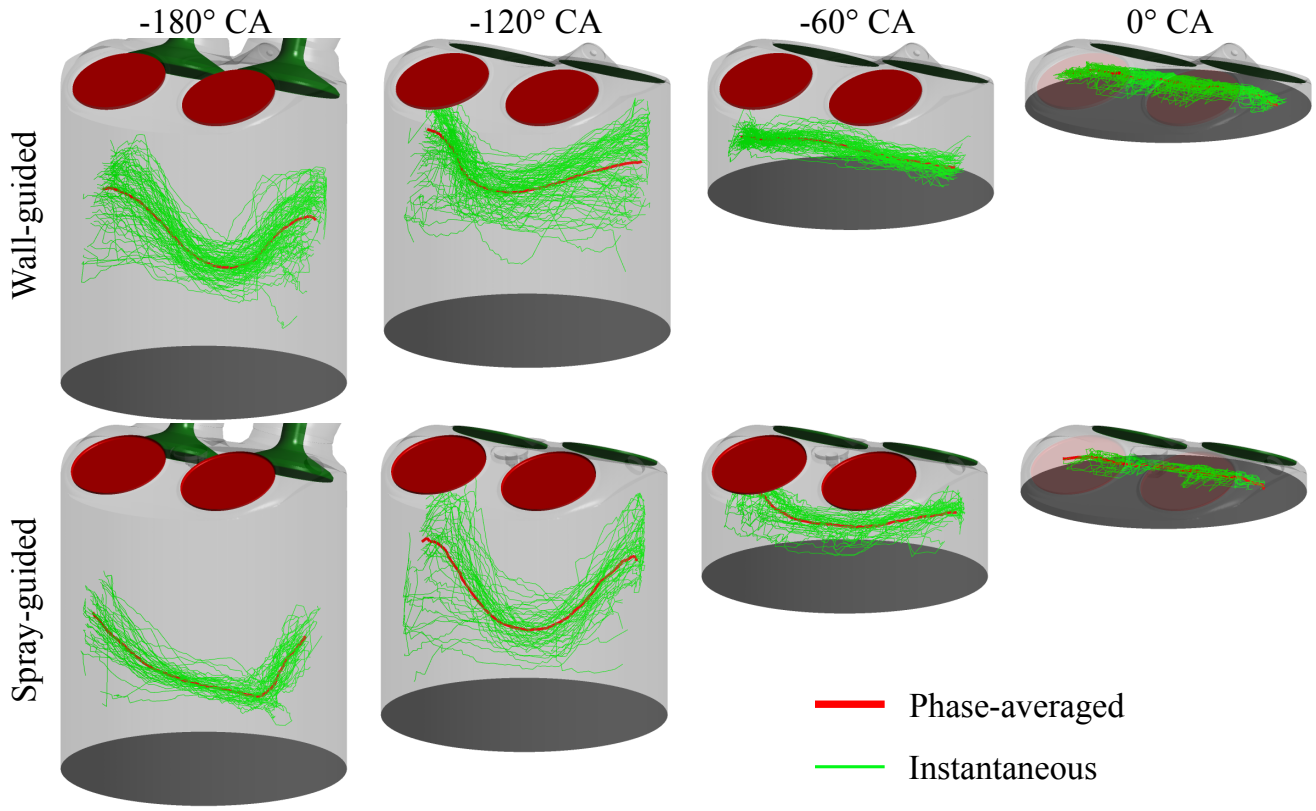

Figure 4.18: Phase-averaged and instantaneous tumble center detected by $\mathbf{\Gamma 1}_{3p}$.

$$\langle d \rangle_{P,Norm}(\mathrm{x},\varphi) = \frac{1}{N}\sum_{n=1}^{N}\sqrt{\left(\frac{\mathrm{y}'(\mathrm{x},\varphi,n)}{b}\right)^2+\left(\frac{\mathrm{z}'(\mathrm{x},\varphi,n)}{s(\varphi)+h}\right)^2}. \tag{4.7}$$

Fluctuations in terms of the spatial coordinate are indicated by y' and z'. In contrast to the evaluation method in section 3.2, the decreasing volume of the combustion chamber is taken into account for this analysis. To do so, each term in equation (4.7) is normalized by its corresponding characteristic length scale, namely the bore b and the height between the uppermost point of the pent-roof cylinder head and the piston (sum of current stroke s and a fixed height of $h = 13.5\,\mathrm{mm}$). Figure 4.19 illustrates the results obtained from equation (4.7). Consistent to the discussion in context with figure 4.18, both engines show different levels of cyclic variability in terms of the tumble center position at −180 °CA. For $|\mathrm{x}| < 20\,\mathrm{mm}$, the differences become smaller until the intake valves are closed (i.e. −130 °CA). This is not the case for the region close to the cylinder liner (marked by **A**), where the CCVs obtained by the WG engine become stronger compared to the ones of the SG engine. It is interesting to see that both engines exhibit a very different behavior after IVC. For the WG engine, $\langle d \rangle_{P,Norm}$ decreases and reaches a local minimum in the range between −80 °CA and −60 °CA (depending on the x position; blue region marked by **B**). During this period, a repeatable and not varying tumble structure (with regard to the TC position) is assumed. This looks quite different for the SG engine, where $\langle d \rangle_{P,Norm}$ remains on a constant level at the center of the combustion chamber and a massive increase is obtained in the region close to the cylinder liner. The differences between the engines become smaller up to about −35 °CA. In the time

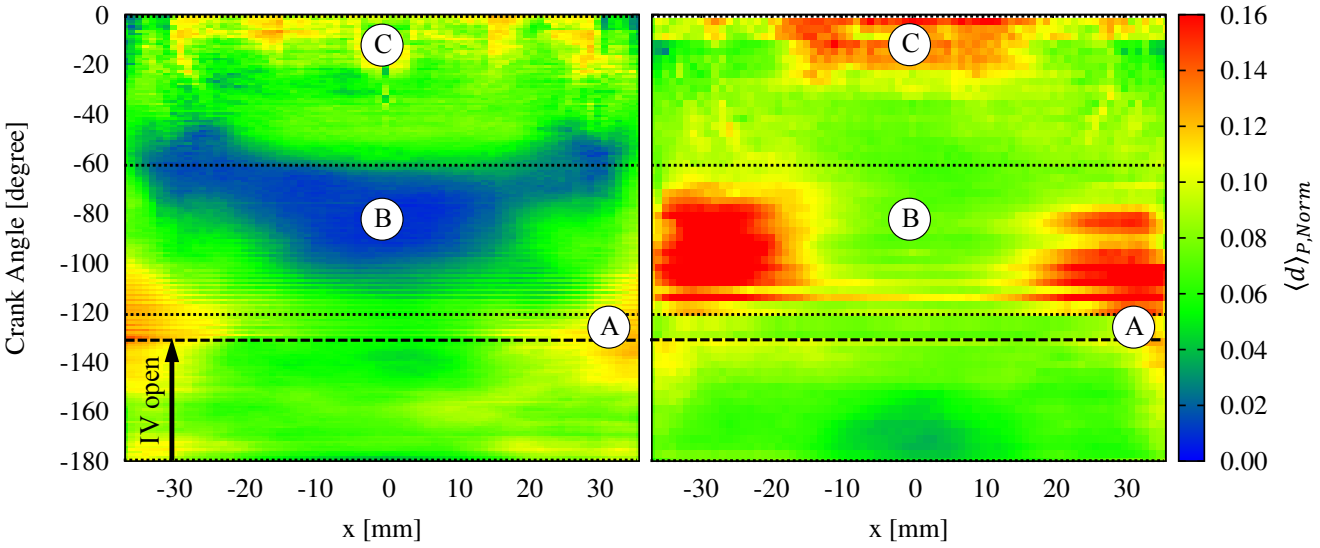

Figure 4.19: Cyclic variability for the WG engine (left) and the SG engine (right). CCVs are quantified by an averaged and normalized distance between the instantaneous and the phase-averaged tumble center positions. Dashed line marks IVC. Dotted lines mark points in time already shown in figure 4.18.

period between −30 °CA and −10 °CA (depending on the x position; marked by **C**), both engines exhibit an increase regarding the cyclic variability. This level is kept until the end of the compression stroke.

Please note that the streaks after IVC (between **A** and **B**; especially visible for the SG engine) result from a discontinuity of the TC position caused by pressure oscillations. The pressure oscillations result from the discretely closed valves (i.e. a shortcoming of the numerical model) and do not represent a physical phenomenon.

Next, the phase-averaged tumble intensity $\langle TI \rangle_P(\mathrm{x}, \varphi)$ is evaluated (see also [138]). It is defined as

$$\langle TI \rangle_P(\mathrm{x}, \varphi) = \frac{1}{2\pi\Omega} \frac{1}{N} \sum_{n=1}^{N} \left(\frac{1}{|A(\mathrm{x})|} \int\limits_{\mathbf{x} \in A(\mathrm{x})} |\boldsymbol{\omega}(\mathbf{x}, \varphi, n) \cdot \mathbf{n}_A(\mathbf{x}, \varphi, n)| \, d\mathbf{x} \right), \tag{4.8}$$

with the engine speed Ω and the vorticity $\boldsymbol{\omega}$. The evaluation is done on circular planes along the TC (exemplarily shown in figure 4.16) with an area $|A(\mathrm{x})|$ and their normal vectors $\mathbf{n}_A$. The higher the tumble intensity the higher is the energy content of the in-cylinder charged motion, stored by its kinetic energy. The obtained results are illustrated in the top row of figure 4.20. Focussing on the center of the combustion chamber (i.e. $|\mathrm{x}| < 20\,\mathrm{mm}$), both engines exhibit a similar behavior during the entire compression stroke. Starting with $\langle TI \rangle_P \approx 10$ (depending on the x position) the TI decreases and reaches a local minimum shortly after IVC. Afterwards, the TI first increases moderately (close to **B**), followed by a stronger increase in the second half of the compression stroke, which results from the conservation of angular momentum. Both engines reach a global maximum in terms of the TI between −40 °CA and −30 °CA and remain on this high level for about 15 °CA. Shortly before TDC, the TI exhibits a rapid drop from $\langle TI \rangle_P \approx 15$ to $\langle TI \rangle_P \approx 6$ in a time period of about 3 °CA (depending on the engine; marked by **C**). Close to the cylinder liner, both engines exhibit a contrary behavior. Starting on a similar level, the TI of the WG engine increases moderately from about −120 to −60 °CA. In contrast, a strong decrease

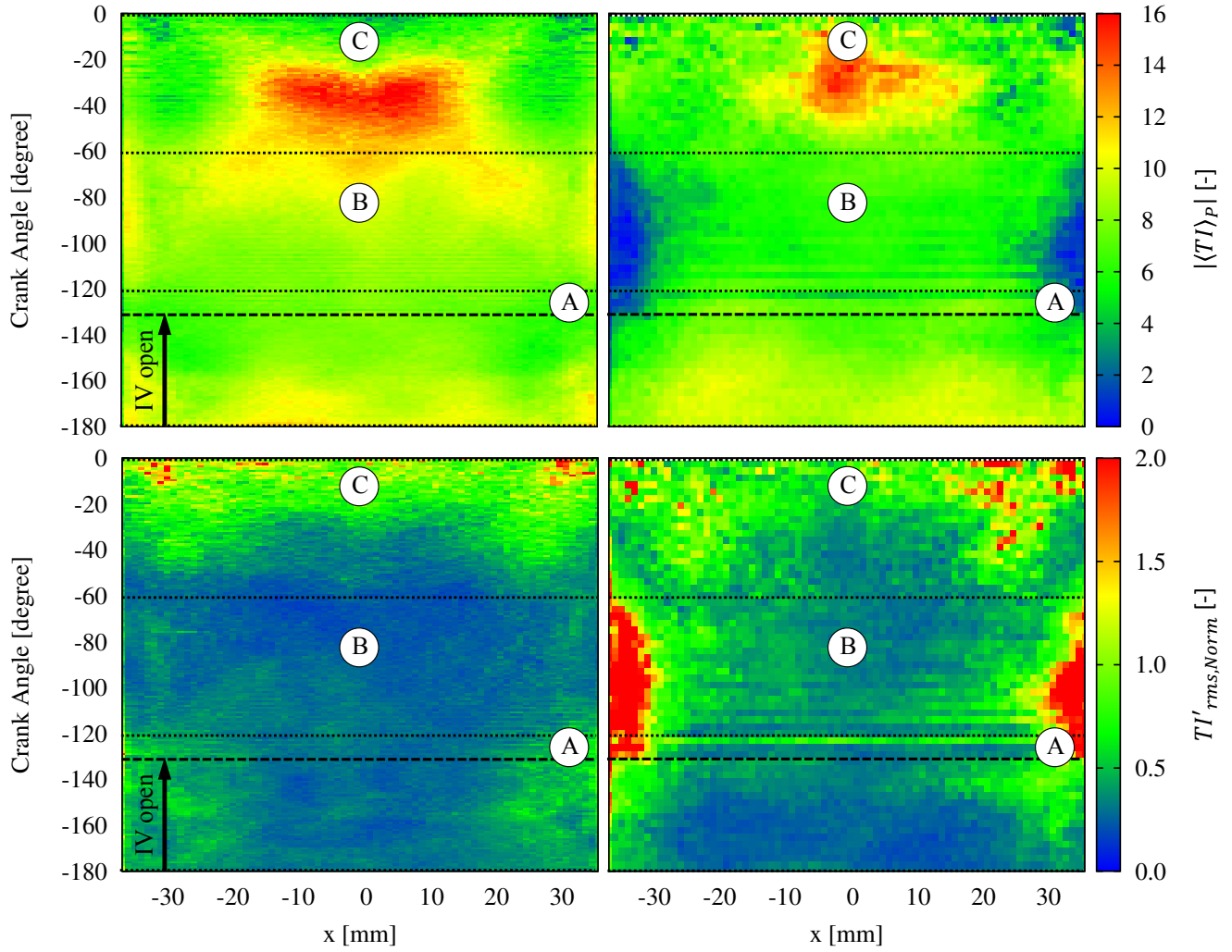

Figure 4.20: Phase-averaged tumble intensity (TI; top row) and its cyclic fluctuations (bottom row) obtained from the WG engine (left) and the SG engine (right). Dashed line marks IVC. Dotted lines mark points in time already shown in figure 4.18.

is identifiable for the SG engine in the same time period. Until the end of the compression stroke, the differences vanish.

The bottom row of figure 4.20 illustrates the cyclic variability with regard to the TI. The calculation of the CCVs, labelled by $TI'_{rms,Norm}(x, \varphi)$, bases on equation (2.23). The results are additionally normalized by $\langle TI\rangle_P(x, \varphi)$. Similar to the TI, both engines show a similar behavior at the center of the combustion chamber and a contrary behavior close to the cylinder liner. Considering the range $-20\,\text{mm} < x < 20\,\text{mm}$, both engines start with a low level of cyclic variability. For the WG engine, the CCVs are kept on a low level until about $-50\,°\text{CA}$, followed by a continuous increase until the end of the compression stroke. For the SG engine, a first moderate increase is identified shortly before IVC. This is followed by a second increase, beginning in the range between $-60°$ and $-40\,°\text{CA}$ (depending on the x position). Close to the cylinder liner, both engines show a similar level for $TI'_{rms,Norm}$ at $-180\,°\text{CA}$. In the middle of the combustion stroke, the WG engine exhibits a decrease and the SG engine a strong decrease. At the end, the cyclic variability for both engines is on a similar level.

To obtain a more condensed presentation, the quantity $|\langle TI\rangle_P|$ is averaged along the TC (denoted as $|\langle TI\rangle_{L,P}|$) in a next step. Due to its importance in terms of a fast and therefore effective combustion in gasoline engines, the volume-and phase-averaged resolved fluctuations $\langle k_{res}\rangle_{V_{Tum},P}$, with $k_{res} = 0.5(u'_{res}{}^2 + v'_{res}{}^2 + w'_{res}{}^2)$ are calculated as well. V_{Tum} represents a tube-like subvolume with the TC as the center-axis and a radius of 3 mm. The results are illustrated in figure 4.21. For the sake of completeness, the in-cylinder charge motion $|\langle \mathrm{Tu_x}\rangle_P|$ (equation (3.1)) and the in-cylinder- and phase-averaged resolved fluctuations $\langle k_{res}\rangle_{V_{Cyl},P}$ are also shown, representing commonly used quantities of the engine design process. All results are shown for the WG engine (left) and SG engine (right).

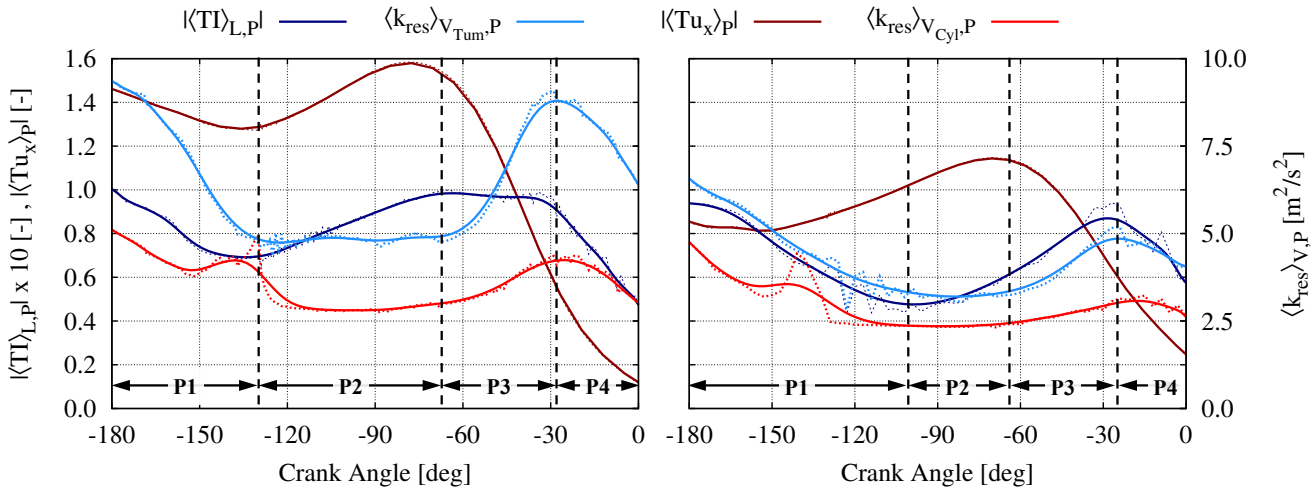

Figure 4.21: Line- and phase-averaged tumble intensity $|\langle TI\rangle_{L,P}|$, subvolume- and phase-averaged resolved fluctuations $\langle k_{res}\rangle_{V_{Tum},P}$, phase-averaged in-cylinder charge motion $|\langle \mathrm{Tu_x}\rangle_P|$ as well as in-cylinder- and phase-averaged resolved fluctuations $\langle k_{res}\rangle_{V_{Cyl},P}$ for WG engine (left) and SG engine (right). P1 to P4 indicate 4 phases in terms of the large-scale tumble structure during the compression stroke. Solid lines and dotted lines represent smoothed curves and raw data, respectively.

At first, $|\langle TI\rangle_{L,P}|$ and $\langle k_{res}\rangle_{V_{Tum},P}$ obtained by the WG engine are considered. Four phases can be distinguished.

P1) Vanishing intake jet: Phase with shrinking energy input into the combustion chamber and a negligible tumble compression (only moderate piston motion and opened intake valves). $|\langle TI\rangle_{L,P}|$ starts with a value of 10 at BDC and decreases until a local minimum of 7 at IVC. In the meantime, $\langle k_{res}\rangle_{V_{Tum},P}$ also decreases due to a significantly reduced production of turbulent structures (less pronounced shear layer of the intake jet).

P2) Tumble compression: The tumble is compressed and the conservation of angular momentum leads to an increase of the TI. $|\langle TI\rangle_{L,P}|$ reaches a local maximum of 10 at −70 °CA and $\langle k_{res}\rangle_{V_{Tum},P}$ remains almost constant (equilibrium between production and dissipation).

P3) Initial tumble breakdown: Phase in which no further increase at the TI can be achieved. $|\langle TI\rangle_{L,P}|$ remains almost constant until −28 °CA although the tumble structure is further compressed. This ongoing tumble compression leads to instabilities, which are directly transferred to a generation/production of small-scale fluctuations. A significant increase in $\langle k_{res}\rangle_{V_{Tum},P}$ is obtained (production larger than dissipation).

P4) Final tumble breakdown: Phase with strongly decreasing TI and fluctuations. Tumble compression becomes small due to the reduced piston motion. The tumble structure decreases to $|\langle TI\rangle_{L,P}| \approx 5$ until fTDC. Also $\langle k_{res}\rangle_{V_{Tum},P}$ decreases until fTDC is reached (dissipation larger than production). The significant reduced energy transfer from the tumble structure to small-scale fluctuations indicates that the tumble is mainly influenced by dissipation.

The in-cylinder charge motion $|\langle \mathrm{Tu_x}\rangle_P|$ starts with a value of 1.46 at BDC and decreases until a local minimum at IVC. Afterwards, it increases to a maximum of 1.58 at −78 °CA, followed by a monotonically drop until fTDC. With exception of the plateau, the general trend of $|\langle \mathrm{Tu_x}\rangle_P|$ is very similar to those obtained by $|\langle TI\rangle_{L,P}|$. Very similar trends also exist for $\langle k_{res}\rangle_{V_{Cyl},P}$ and $\langle k_{res}\rangle_{V_{Tum},P}$. With exception of a deviation shortly before IVC, both curves exhibit same phases with decreasing, constant and increasing values. Even the local minimum and maximum exist at the same points in time.
Different results occur for the SG engine, which is especially true for $|\langle TI\rangle_{L,P}|$ and $\langle k_{res}\rangle_{V_{Tum},P}$. Again, a time period exists with the same characteristics as the phase **P1** obtained by the WG engine. However, the local minimum at $|\langle TI\rangle_{L,P}|$ is reached considerably after IVC. Compared to the WG engine, phase **P2** is significantly shorter and less pronounced. It can be allocated in the time period from −100 °CA to −65 °CA, where an increase for $|\langle TI\rangle_{L,P}|$ and relatively stable values for $\langle k_{res}\rangle_{V_{Tum},P}$ exist. The major difference to the WG engine concerns phase **P3**. In absence of an plateau, the TI exhibits a continuous increase, which goes hand in hand with an increase in terms of $\langle k_{res}\rangle_{V_{Tum},P}$. Both quantities reach a maximum value at about −25 °CA. It should be noted that the maximum values are considerably smaller than those obtained by the WG engine. Phase **P4** shows the same trend as is the case for the WG engine. Considering the trend of the in-cylinder charge motion $|\langle \mathrm{Tu_x}\rangle_P|$ and $\langle k_{res}\rangle_{V_{Cyl},P}$, no significant differences to the WG are identified. An interesting fact is that the local minimum of $|\langle \mathrm{Tu_x}\rangle_P|$ is shifted towards the BDC (compared to the WG engine), while the minimum obtained by $|\langle \mathrm{Tu_x}\rangle_P|$ lies closer to the TDC.

4.4.3 Interim findings

In this section, the development of the large-scale tumble structure during the compression stroke was investigated. Several observations were made:

i) Phase-averaged velocity field:
Both engines exhibit a considerable rotational in-cylinder charge motion (i.e. tumble) for a wide time period during the compression stroke.

ii) Phase-averaged and instantaneous tumble center (TC):
The temporal development of the phase-averaged TC was shown and a complex tumble structure was figured out. Depending on the crank angle, both engines exhibit a notable spreading in terms of the instantaneous TC position, which indicates strong CCVs. The WG engine showed a repeatable TC position in the range between −100 °CA to −40 °CA. In contrast, the SG engine exhibits stronger CCVs. A first indicator for the tumble breakdown is the increased cyclic variability shortly before fTDC for both engines.

iii) Phase-averaged tumble intensity (TI) and its cyclic variations:
Considering the center of the combustion chamber, both engines exhibit a strong increase at the TI

during the second half of the compression stroke. After reaching a maximum, the TI remains on this high level for a time period of about 15 °CA. Shortly before fTDC (exact point in time differs for both engines) a massive drop within a time period of about 3 °CA occurs. Both engines exhibit moderate CCVs in terms of the TI for a wide time period during the compression stroke. A massive increase of the CCVs occur in the range of $-40\,°\text{CA} < \varphi < -20\,°\text{CA}$. This and the massive drop with regard to the TI before fTDC are a second indicator for the tumble breakdown.

iv) Evaluation of integral quantities:
Based on the line- and phase-averaged tumble intensity and the subvolume- and phase-averaged resolved fluctuations, the compression stroke was classified into four phases. The first phase is connected to the intake jet. During the second phase the TI is increased due to the tumble compression. The third and fourth phase were associated to the tumble breakdown. A very different behavior for both engines could be figured out.

5 Conclusion and further studies

Despite more than 100 years of experience, ICEs are still a big challenge for industry and academia, and their development is still a predominantly heuristic approach. For the last three decades, due to the increasing computational resources and the arising possibilities in terms of analyses, CFD has become more and more important. In line with this further growing importance, the presented work offered a numerical study of several ICEs with focus on two topics:

- Investigation of modeling aspects
- Investigation of the intake flow

All presented studies were done based on experimental engine setups and compared to existing measurements (and numerical data in case of their significance) to ensure a high quality of the obtained results. To take into account effects caused by CCVs, scale-resolving turbulence models were used throughout this thesis.

Investigation of modeling aspects

An appropriate modeling in terms of ICEs is a crucial and widely discussed point. This is particularly true for scale-resolving simulations, where the chosen modeling approach significantly affects the temporal and spatial development of resolved fluctuations and consequently the CCVs. The presented study focussed on two modeling aspects. The aim was to identify the requirements and to obtain an accurate in-cylinder velocity field as well as cyclic variations.

The first modeling aspect dealt with the location of the boundaries as well as the temporal treatment of the intake ports and the exhaust ports. Based on a well-known experimental engine setup, running in motored operation condition, three different port modeling strategies were applied:

- LPP: Entire intake and exhaust port up to the pressure plenum were simulated throughout the entire operating cycle.
- SPP: Shortened intake and exhaust ports were calculated throughout the operating cycle.
- SPT: Same domain as SPP with temporally disabled ports for the time period when the corresponding valves were closed.

Each of these variants was analyzed based on a total number of 60 consecutive cycles.
Evaluating the integral quantities (e.g. the integral in-cylinder charge motion), all models exhibited similar phase-averaged results and CCVs. A qualitative and quantitative comparison of the velocity components and their fluctuations offered a good agreement among the different simulations as well as between the simulations and the experiment. All port modeling strategies exhibited an intake jet, which resulted in a distinctive rotational in-cylinder tumble motion. This tumble dominated the in-cylinder flow field during the second half of the intake stroke and for a long time period during the compression stroke. It can be summarized that there were only negligible differences between the different modeling approaches in terms of the simulation results. Considering the computational resources, the demands of the LPP model were more than twice as high as those of the short port approaches. SSP and SPT, which

were on a similar level, offer a good compromise between computational demands and accuracy. This fact becomes particularly important when a large number of engine cycles is needed, e.g. for statistics, as it is the case here.

The second modeling aspect dealt with the accuracy of scale-resolving turbulence models and their capability to capture large-scale and small-scale fluctuations. Three LES models (Smagorinsky, WALE, Sigma), one hybrid model (DES-SST) and one second-generation URANS model (SAS-SST) were investigated, based on a simplified engine setup running in motored operation condition. To ensure a reliable, consistent and systematic comparison, all simulations were performed on the same grid and numerical approach (e.g. time integration). A total number of 312 realizations for each turbulence model formed the basis for the investigation.

Very similar phase-averaged in-cylinder flow structures were obtained for all applied models. Small differences occurred at the penetration depth of the intake jet and the exact position of the tumble-like vortex structure. Larger differences existed at the resolved small-scale velocity fluctuations (e.g. in the jet shear layer). Considering the tumble center, all models showed a high variability at the beginning of the tumble formation, a decreased cyclic variability in the middle of the intake stroke and increasing CCVs at the end of the intake stroke.

In case of sufficient spatial and temporal resolution, the Sigma model is a very suitable choice. It represents a state of the art LES model and has the advantage that it yields the correct scaling towards walls. Compared to DES-SST and SAS-SST, it exhibits a higher amount of resolved turbulent structures, which can be useful for further analyses and/or the interaction with other models, e.g. for the accurate description of mixing. For more realistic engine geometries and operation points, hybrid models become more relevant. Higher engine speeds and therefore higher (local) variations of the Reynolds number lead to very small turbulent scales. Thus, a sufficient spatial and temporal resolution might not be guaranteed within the entire computational domain. Here, the underlying URANS approach offers a reasonable backup for describing the fluid flow. For sufficiently high Reynolds numbers, the SAS model shows preferable characteristics, especially since other models such as the DES family might require special attention to avoid numerical artefacts like grid induced separation.

Investigation of the intake flow

As mentioned previously, ICEs combine a multitude of highly complex and interacting sub-processes, like fluid mechanics, mixing processes and combustion. The intake flow is placed at the beginning of the so-called cause-and-effect chain and great care should be taken in its prediction quality. For example, cyclic variations in the combustion phase originate (at least partially) from CCVs of the intake flow and even the best models are ineffective in case of an incorrect flow field. Due to this importance, the presented work focussed on the intake jet and the large-scale tumble motion.

The first topic dealt with the intake flow of a simplified engine setup (flow bench configuration) with focus on the part of the intake jet which points into the center of the combustion chamber. To estimate the sensitivity of this tumble forming phenomenon, several modeling aspects, like the applied turbulence model and the numerical grid, were discussed. In a first step, a detailed comparison between experiment and the simulation results was done, and relevant phenomena (e.g. flow separation at the intake valve) were explained. Afterwards, the velocity field was transformed into a local coordinate system (locally

aligned with the jet centerline) and normalized by the mass flow through the valve gap. The highly complex jet structure could be divided into three zones:

- Strong acceleration of the flow (in vicinity of the valve gap) with low level of resolved velocity fluctuations
- Moderate velocity decrease and increasing resolved fluctuations
- Strong velocity decrease and moderate decrease of resolved fluctuations

It can be summarized that the intake jet position, its orientation, its penetration depth and its curvature strongly depend on the applied numerical approach. For an accurate prediction of the intake jet (and the resulting tumble motion) the region close to the intake valve demands a particularly high level of attention (e.g. during the mesh generation).

The second topic aimed to identify and quantify the cyclic variability of large-scale structures within the combustion chamber. To do so, the instantaneous velocity fields were decomposed into an averaged part as well as a large and a small-scale contribution to the total fluctuations. The separation of the fluctuations based on a combination of POD and conditional averaging. The instantaneous flow fields were grouped into different subsets by usage of the cycle-dependent POD coefficients. Afterwards, averaged fields were calculated using the individual subsets (subset-averaged) and all available data sets (phase-averaged). The difference between the subset average and phase average was defined as large-scale fluctuation (CCV), while the difference between the instantaneous velocity field and its specific subset average denote small-scale fluctuation.
The new ad-hoc methodology was applied on a simplified engine setup running in motored operation condition with 208 independent samples. The focus was to detect large scale flow topologies and their cyclic fluctuations in addition to small-scale fluctuations. All subset averages showed similar structural elements, consisting of an intake jet and a tumble-like vortex structure in the center of the cylinder. However, there existed clear deviations in terms of the intake jet (e.g. orientation and penetration depth) for each of the four subsets. Furthermore, a variation of the vortex core position was detected. Small-scale structures occurred in regions where high turbulent fluctuations are expected, e.g. in the shear-layer of the intake jet. It can be concluded that the proposed methodology allows to separate fluctuations of the velocity field into a large-scale coherent and a small-scale turbulent contribution.

In the third subsection, the generation of the large-scale tumble structure and its interaction to the piston boundary layer during the intake stroke was studied. The basis for this were 30 realizations of an experimental gasoline engine setup with a state-of-the-art cylinder head.
In accordance to the previous setups, the engine exhibited a distinctive intake jet which leaded to a significant rotational in-cylinder charge motion (i.e. tumble). An extension of a previously presented methodology was developed and applied to detect and visualize the phase-averaged tumble center within the 3D flow field. The phase-averaged and the instantaneous tumble center were highly deformed at the beginning of the tumble generation. A less complex tumble center structure occurred at the end of the intake stroke. During its entire existence, the tumble center exhibited a significantly rotational and translational movement, even in the phases with a piston speed of almost zero. Based on the instantaneous tumble center, it could be shown that significant cycle-to-cycle variations exist.
Consequently, the piston boundary layer was analyzed. Its thickness was computed based on specified

values of the dimensionless wall normal distance and strongly varying values (with regard to the piston surface) were extracted. This varying boundary layer thickness could be connected to the large-scale tumble structure, which leads to regions similar to a stagnation point and wall-parallel flows. Finally, dimensionless velocity profiles were calculated and significant deviations from the classical boundary layer profile were found.

In the last subsection, the tumble development during the compression stroke was considered. The investigation based on two well-known experimental engine setups, running in motored operation condition. A total number of 100 and 50 consecutive cycles (depending on the engine) were calculated.
Consistent to the previous subsections, the phase-averaged velocity fields exhibited a significant tumble motion, existent for a wide time period during the compression stroke. The evaluation of the phase-average and instantaneous tumble displayed a highly complex tumble structure for both engines as well as a notable cyclic variability in terms of the tumble center position. To gain an impression of the kinetic energy stored by the in-cylinder charged motion, the phase-averaged tumble intensity was evaluated. Apart from differences with regard to the exact values, both engines showed a similar general trend with a notable increase during the second half of the intake stroke and a massive drop shortly before fTDC. Moderate CCVs of the tumble intensity until about −30 °CA were obtained. This was followed by a strong increase until fTDC. In a final step, the tumble intensity in connection with the velocity fluctuations within the tumble structure were analyzed. The tumble development during the compression stroke could be subdivided into four consecutive phases *vanishing intake jet*, *tumble compression*, *initial tumble breakdown* and *final tumble breakdown*. However, the intensity of these phases differ for both engines.

In summary, detailed insights into the intake jet and the tumble structure within IC engines were given. By means of the usage of newly developed post processing methodologies both phenomena were characterized in terms of their phase-averaged and instantaneous structures. Furthermore, their cyclic variability could be figured out and quantified.
The new methodologies and findings offer an excellent base for further analyses with regard to the previously mentioned cause-and-effect chain. A very interesting phenomena is the impact of the large-scale tumble structure and its cyclic variability on the combustion and therefore the efficiency of an IC engine. In order to make a quantitative statement, a substantial number of engine geometries under identical operating conditions and boundary conditions should be considered.

References

[1] Y. Orbach and G. Fruchter. *Forecasting sales and product evolution: The case of the hybrid/electric car*. In: *Technological Forecasting and Social Change* 78.7 (2011), pp. 1210 –1226. DOI: 10.1016/j.techfore.2011.03.018.

[2] BP. *BP Energy Outlook 2017 edition*. 2017.

[3] Continental Automotive GmbH - Business Unit Engine Systems. *Continental Engine Systems Strategie - DRIVE 25*. Siemenssstr. 12, 93055 Regensburg, Dec. 2017.

[4] F. Dudenhöffer. *Pkw-Neuwagen: geringere CO2-Belastungen ohne Zusatzkosten möglich*. In: *Wirtschaftsdienst* 94.8 (2014), pp. 600–602. DOI: 10.1007/s10273-014-1721-7.

[5] European Commission. *type approval of motor vehicles with respect to emissions from light passenger and commercial vehicles (Euro 5 and Euro 6) and on access to vehicle repair and maintenance information*. In: *Official Journal of the European Union* (2007).

[6] European Commission. *amending Regulation (EC) No 715/2007 of the European Parliament and of the Council and Commission Regulation (EC) No 692/2008 as regards emissions from light passenger and commercial vehicles (Euro 6)*. In: *Official Journal of the European Union* (2012).

[7] European Commission. *amending Regulation (EC) No 692/2008 as regards emissions from light passenger and commercial vehicles (Euro 6)*. In: *Official Journal of the European Union* (2016).

[8] J. Hadler et al. *Methoden für die Entwicklung eines RDE-fähigen Antriebs*. In: *Motortechnische Zeitschrift* 76.7-8 (2015), pp. 58–63.

[9] J. Hadler et al. *Einflussfaktoren auf die Partikelentstehung unter Realfahrbedingungen*. In: *Motortechnische Zeitschrift* 77.3 (2016).

[10] European Parliament and Council of European Union. *Setting emission performance standards for new passenger cars as part of the community's integrated approach to reduce CO2 emissions from light-duty vehicles*. In: *Official Journal of the European Union* (2009).

[11] European Parliament and Council of European Union. *Regulation (EC) No 443/2009 to define the modalities for reaching the 2020 target to reduce CO2 emissions from new passenger cars*. In: *Official Journal of the European Union* (2014).

[12] R. Budack et al. *Der neue 2,0-l-R4-TFSI-Motor von Audi*. In: *MTZ-Motortechnische Zeitschrift* 77.5 (2016), pp. 16–25.

[13] V. Wong et al. *Assessment of thin thermal barrier coatings for IC engines*. Tech. rep. SAE Technical Paper, 1995.

[14] H. Kosaka et al. *Concept of "Temperature Swing Heat Insulation" in Combustion Chamber Walls, and Appropriate Thermo-Physical Properties for Heat Insulation Coat*. In: *SAE International Journal of Engines* 6 (2013), pp. 142–149. DOI: 10.4271/2013-01-0274..

[15] Y. Wakisaka et al. *Reduction of Heat Loss and Improvement of Thermal Efficiency by Application of "Temperature Swing" Insulation to Direct-Injection Diesel Engines*. In: *SAE Int. J. Engines* 9 (Apr. 2016), pp. 1449–1459. DOI: 10.4271/2016-01-0661.

[16] T. Goto et al. *Der neue Ottomotor Skyactiv-G von Mazda*. In: *MTZ-Motortechnische Zeitschrift* 72.6 (2011), pp. 476–483.

[17] A. Scholtissek et al. *Internal Combustion Engine - cause-and-effect chain*. In: (2017). DOI: 10.6084/m9.figshare.5170480.v1.

[18] H. Schlichting and K. Gersten. *Boundary-layer theory*. 8th. Springer Science & Business Media, 2000.

[19] C. Hasse et al. *Hybrid URANS/LES Turbulence Simulation of Vortex Shedding Behind a Triangular Flameholder*. In: *Flow, Turbulence and Combustion* 83.1 (2009), pp. 1–20. DOI: 10.1007/s10494-008-9186-7.

[20] A. Nasr and J. Lai. *A turbulent plane offset jet with small offset ratio*. In: *Experiments in Fluids* 24.1 (1998), pp. 47–57. DOI: 10.1007/s003480050149.

[21] S. Pope. *Turbulent Flows*. 1st. Cornell University, 2000.

[22] A. Assoudi et al. *Experimental and numerical study of an offset jet with different velocity and offset ratios*. In: *Engineering Applications of Computational Fluid Mechanics* 9.1 (2015), pp. 490–512. DOI: 10.1080/19942060.2015.1071525.

[23] N. Zuckerman and N. Lior. *Jet impingement heat transfer: physics, correlations, and numerical modeling*. In: *Advances in heat transfer* 39 (2006), pp. 565–631. DOI: 10.1016/S0065-2717(06)39006-5.

[24] G. Carlomagno and A. Ianiro. *Thermo-fluid-dynamics of submerged jets impinging at short nozzle-to-plate distance: a review*. In: *Experimental thermal and fluid science* 58 (2014), pp. 15–35. DOI: 10.1016/j.expthermflusci.2014.06.010.

[25] C Jainski et al. *Laser imaging investigation of transient heat transfer processes in turbulent nitrogen jets impinging on a heated wall*. In: *International Journal of Heat and Mass Transfer* 74 (2014), pp. 101 –112. DOI: 10.1016/j.ijheatmasstransfer.2014.02.072.

[26] J. Borée and P. Miles. *In-Cylinder Flow*. In: *Encyclopedia of Automotive Engineering*. John Wiley & Sons, Ltd, 2014. DOI: 10.1002/9781118354179.auto119.

[27] C. Hasse. *Scale-resolving simulations in engine combustion process design based on a systematic approach for model development*. In: *International Journal of Engine Research* 17.1 (2016), pp. 44–62. DOI: 10.1177/1468087415597842.

[28] R. Moser, J. Kim, and N. Mansour. *Direct numerical simulation of turbulent channel flow up to Re=590*. In: *Physics of Fluids* 11.4 (1999), pp. 943–945. DOI: http://dx.doi.org/10.1063/1.869966.

[29] R. Adrian. *Hairpin vortex organization in wall turbulence*. In: *Physics of Fluids* 19.4 (2007). DOI: 10.1063/1.2717527.

[30] C. Baumgarten. *Mixture formation in internal combustion engines*. Springer Science & Business Media, 2006.

[31] R. Lebas et al. *Numerical simulation of primary break-up and atomization: DNS and modelling study*. In: *International Journal of Multiphase Flow* 35.3 (2009), pp. 247 –260. DOI: 10.1016/j.ijmultiphaseflow.2008.11.005.

[32] J. Shinjo and A. Umemura. *Simulation of liquid jet primary breakup: Dynamics of ligament and droplet formation*. In: *International Journal of Multiphase Flow* 36.7 (2010), pp. 513 –532. DOI: 10.1016/j.ijmultiphaseflow.2010.03.008.

[33] L. Jing and X. Xu. *Direct Numerical Simulation of Secondary Breakup of Liquid Drops*. In: *Chinese Journal of Aeronautics* 23.2 (2010), pp. 153 –161. DOI: 10.1016/S1000-9361(09)60199-0.

[34] S. Sazhin. *Modelling of fuel droplet heating and evaporation: recent results and unsolved problems*. In: *Fuel* 196 (2017), pp. 69–101. DOI: 10.1016/j.fuel.2017.01.048.

[35] J. Bellan. *Supercritical (and subcritical) fluid behavior and modeling: drops, streams, shear and mixing layers, jets and sprays*. In: *Progress in Energy and Combustion Science* 26.4 (2000), pp. 329 –366. DOI: http://dx.doi.org/10.1016/S0360-1285(00)00008-3.

[36] J. Heywood. *Internal Combustion Engines Fundamentals*. 1st. McGraw-Hill, 1988.

[37] R. Dahms et al. *Understanding ignition processes in spray-guided gasoline engines using high-speed imaging and the extended spark-ignition model SparkCIMM. Part A: Spark channel processes and the turbulent flame front propagation*. In: *Combustion and Flame* 158.11 (2011), pp. 2229 –2244. DOI: 10.1016/j.combustflame.2011.03.012.

[38] Henning Bockhorn. *Soot formation in combustion: mechanisms and models*. Vol. 59. Springer-Verlag, 1994.

[39] N. Peters. *Turbulent Combustion*. Cambridge University Press, 2000.

[40] J. Tan et al. *Developments in computational fluid dynamics modelling of gasoline direct injection engine combustion and soot emission with chemical kinetic modelling*. In: *Applied Thermal Engineering* 107 (2016), pp. 936 –959. DOI: 10.1016/j.applthermaleng.2016.07.024.

[41] C. Hasse et al. *Quenching of laminar iso-octane flames at cold walls*. In: *Combustion and Flame* 122.1 (2000), pp. 117 –129. DOI: 10.1016/S0010-2180(00)00107-3.

[42] A. Gruber et al. *Turbulent flame-wall interaction: a direct numerical simulation study*. In: *Journal of Fluid Mechanics* 658 (2010), pp. 5–32. DOI: 10.1017/S0022112010001278.

[43] A. Dreizler and B. Böhm. *Advanced laser diagnostics for an improved understanding of premixed flame-wall interactions*. In: *Proceedings of the Combustion Institute* 35.1 (2015), pp. 37 –64. DOI: 10.1016/j.proci.2014.08.014.

[44] D. Bradley and G. Kalghatgi. *Influence of autoignition delay time characteristics of different fuels on pressure waves and knock in reciprocating engines*. In: *Combustion and Flame* 156.12 (2009), pp. 2307 –2318. DOI: http://dx.doi.org/10.1016/j.combustflame.2009.08.003.

[45] S. Fontanesi, A. d'Adamo, and C. Rutland. *Large-Eddy simulation analysis of spark configuration effect on cycle-to-cycle variability of combustion and knock*. In: *International Journal of Engine Research* 16.3 (2015), pp. 403–418. DOI: 10.1177/1468087414566253.

[46] E. Meindl. *Numerical and Experimental Investigation of Knock in Turbocharged Direct Injection Spark Ignition Engines*. PhD thesis. TU Bergakademie Freiberg, 2016.

[47] G. Lecocq et al. *A new LES model coupling flame surface density and tabulated kinetics approaches to investigate knock and pre-ignition in piston engines*. In: *Proceedings of the Combustion Institute* 33.2 (2011), pp. 3105–3114. DOI: 10.1016/j.proci.2010.07.022.

[48] C. Rutland. *Large-eddy simulations for internal combustion engines - a review*. In: *International Journal of Engine Research* 12.5 (2011). DOI: 10.1177/1468087411407248.

[49] J. Fröhlich. *Large Eddy Simulation turbulenter Strömungen*. 1st. B.G. Teubner, 2006.

[50] P. Spalart et al. *Comments on the feasibility of LES for wings, and on a hybrid RANS/LES approach*. In: *Advances in DNS/LES* 1 (1997), pp. 4–8.

[51] C. Hasse, V. Sohm, and B. Durst. *Detached eddy simulation of cyclic large scale fluctuations in a simplified engine setup*. In: *International Journal of Heat and Fluid Flow* 30.1 (2009), pp. 32–43. DOI: 10.1016/j.ijheatfluidflow.2008.10.001.

[52] B. Enaux et al. *LES study of cycle-to-cycle variations in a spark ignition engine*. In: *Proceedings of the combustion Institute* 33.2 (2011), pp. 3115–3122. DOI: 10.1016/j.proci.2010.07.038.

[53] T. Kuo et al. *Large Eddy Simulation (LES) for IC Engine Flows*. In: *Oil & Gas Science and Technology - Revue d'IFP Energie Nouvelles* 69.1 (2014), pp. 61–81. DOI: 10.2516/ogst/2013127.

[54] D. Goryntsev et al. *Analysis of cyclic variations of liquid fuel-air mixing processes in a realistic DISI IC-engine using Large Eddy Simulation*. In: *International Journal of Heat and Fluid Flow* 31.5 (2010), pp. 845–849. DOI: 10.1016/j.ijheatfluidflow.2010.04.012.

[55] C. Hasse, V. Sohm, and B. Durst. *Numerical investigation of cyclic variations in gasoline engines using a hybrid URANS/LES modeling approach*. In: *Computers & Fluids* 39.1 (2010), pp. 25–48. DOI: 10.1016/j.compfluid.2009.07.001.

[56] K. Liu et al. *Large-eddy Simulation of Motored Flow in a Two-valve Piston Engine: POD Analysis and Cycle-to-cycle Variations*. In: *Flow, Turbulence and Combustion* 91.2 (2013), pp. 373–403. DOI: 10.1007/s10494-013-9475-7.

[57] R. Yu and X. Bai. *A semi-implicit scheme for large eddy simulation of piston engine flow and combustion*. In: *International Journal for Numerical Methods in Fluids* 71.1 (2013), pp. 13–40. DOI: 10.1002/fld.3644.

[58] V. Mittal et al. *LES of gas exchange in IC engines*. In: *Oil & Gas Science and Technology - Revue d'IFP Energie Nouvelles* 69.1 (2014), pp. 29–40. DOI: 10.2516/ogst/2013122.

[59] S. Fontanesi et al. *Investigation of boundary condition and field distribution effects on the cycle-to-cycle variability of a turbocharged GDI engine using LES*. In: *Oil & Gas Science and Technology - Rev. IFP Energie Nouvelles* 69.1 (2014), pp. 107–128. DOI: 10.2516/ogst/2013142.

[60] M. Toledo et al. *Large eddy simulation of the generation and breakdown of a tumbling flow*. In: *International journal of heat and fluid flow* 28.1 (2007), pp. 113–126. DOI: 10.1016/j.ijheatfluidflow.2006.03.029.

[61] D. Haworth. *Large-Eddy Simulation of in-Cylinder Flows*. In: *Oil & Gas Science and Technology - Revue d'IFP Energie Nouvelles* 54.2 (1999), pp. 175–185. DOI: 10.2516/ogst:1999012.

[62] D. Haworth and K. Jansen. *Large-eddy simulation on unstructured deforming meshes: towards reciprocating IC engines*. In: *Computers & Fluids* 29.5 (2000), pp. 493–524. DOI: 10.1016/S0045-7930(99)00015-8.

[63] M. Baumann, F. di Mare, and J. Janicka. *On the Validation of Large Eddy Simulation Applied to Internal Combustion Engine Flows Part II: Numerical Analysis*. In: *Flow, Turbulence and Combustion* 92.1 (2014), pp. 299–317. DOI: 10.1007/s10494-013-9472-x.

[64] O. Vermorel et al. *Towards the understanding of cyclic variability in a spark ignited engine using multi-cycle LES*. In: *Combustion and Flame* 156.8 (2009), pp. 1525–1541. DOI: 10.1016/j.combustflame.2009.04.007.

[65] K. Liu and D. Haworth. *Large-Eddy Simulation for an Axisymmetric Piston-Cylinder Assembly With and Without Swirl*. In: *Flow, Turbulence and Combustion* 85.3-4 (2010), pp. 279–307. DOI: 10.1007/s10494-010-9292-1.

[66] F. Brusiani, C. Forte, and G. Bianchi. *Assessment of a numerical methodology for large eddy simulation of ice wall bounded non-reactive flows*. Tech. rep. SAE Technical Paper, 2007.

[67] F. Brusiani and G. Bianchi. *LES simulation of ICE non-reactive flows in fixed grids*. Tech. rep. SAE Technical Paper, 2008.

[68] A. Montorfano et al. *Comparison of Direct and Large Eddy Simulations of the Turbulent Flow in a Valve/Piston Assembly*. In: *Flow, Turbulence and Combustion* 95.2 (2015), pp. 461–480. DOI: 10.1007/s10494-015-9620-6.

[69] A. Sjunnesson, C. Nelsson, and E. Max. *LDA measurements of velocities and turbulence in a bluff body stabilized flame*. In: *Laser Anemometry* 3 (1991), pp. 83–90.

[70] D. Lyn et al. *A laser-Doppler velocimetry study of ensemble-averaged characteristics of the turbulent near wake of a square cylinder*. In: *Journal of Fluid Mechanics* 304 (1995), pp. 285–319. DOI: 10.1017/s0022112095004435.

[71] A. Kravchenko and P. Moin. *Numerical studies of flow over a circular cylinder at Re_D=3900*. In: *Physics of Fluids* 12.2 (2000), pp. 403–417. DOI: 10.1063/1.870318.

[72] M. Klein, A. Sadiki, and J. Janicka. *Investigation of the influence of the Reynolds number on a plane jet using direct numerical simulation*. In: *International Journal of Heat and Fluid Flow* 24.6 (2003), pp. 785–794. DOI: 10.1016/S0142-727X(03)00089-4.

[73] A. Amamou et al. *Numerical study of turbulent round jet in a uniform counterflow using a second order Reynolds Stress Model*. In: *Journal of Hydro-Environment Research* 9.4 (2015), pp. 482–495. DOI: 10.1016/j.jher.2015.04.004.

[74] B. Armalyt et al. *Experimental and theoretical investigation of backward-facing step flow*. In: *Journal of Fluid Mechanics* 127 (1983), pp. 473–496. DOI: 10.1017/s0022112083002839.

[75] S. Jovic and D. Driver. *Backward-facing step measurements at low Reynolds number, Re_h=5000*. Tech. rep. 1994.

[76] H. Le, P. Moin, and J. Kim. *Direct numerical simulation of turbulent flow over a backward-facing step*. In: *Journal of fluid mechanics* 330.1 (1997), pp. 349–374. DOI: 10.1017/s0022112096003941.

[77] H. Lübcke et al. *Comparison of LES and RANS in bluff-body flows*. In: *Journal of Wind Engineering and Industrial Aerodynamics* 89.14-15 (2001), pp. 1471–1485. DOI: 10.1016/s0167610501001349.

[78] P. Catalano et al. *Numerical simulation of the flow around a circular cylinder at high Reynolds numbers*. In: *International Journal of Heat and Fluid Flow* 24.4 (2003), pp. 463–469. DOI: 10.1016/S0142-727X(03)00061-4.

[79] D. Cavar and K. Meyer. *LES of turbulent jet in cross-flow: Part 1 - A numerical validation study*. In: *International Journal of Heat and Fluid Flow* 36 (2012), pp. 18–34. DOI: 10.1016/j.ijheatfluidflow.2011.12.009.

[80] K. Akselvoll and P. Moin. *Large eddy simulation of a backward facing step flow*. In: *Engineering Turbulence Modelling and Experiments* 2 (2014), pp. 303–313. DOI: 10.1016/B978-0-444-89802-9.50033-2.

[81] M. Voisine et al. *Spatio-temporal structure and cycle to cycle variations of an in-cylinder tumbling flow*. In: *Experiments in Fluids* 50.5 (2011), pp. 1393–1407. DOI: 10.1007/s00348-010-0997-7.

[82] E. Baum et al. *On the validation of LES applied to internal combustion engine flows: Part 1: Comprehensive experimental database*. In: *Flow, Turbulence and Combustion* 92.1-2 (2014), pp. 269–297. DOI: 10.1007/s10494-013-9468-6.

[83] F. Zentgraf et al. *On the turbulent flow in piston engines: Coupling of statistical theory quantities and instantaneous turbulence*. In: *Physics of Fluids* 28.4 (2016). DOI: 10.1063/1.4945785.

[84] D. Freudenhammer et al. *Volumetric intake flow measurements of an IC engine using magnetic resonance velocimetry*. In: *Experiments in Fluids* 55.5 (2014), pp. 1–18. DOI: 10.1007/s00348-014-1724-6.

[85] D. Freudenhammer et al. *The influence of cylinder head geometry variations on the volumetric intake flow captured by Magnetic Resonance Velocimetry*. In: *SAE International Journal of Engines* 8.2015-01-1697 (2015), pp. 1826–1836.

[86] F. Hartmann et al. *Spatially resolved Experimental and Numerical Investigation of the Flow through the Intake Port of an IC Engine*. In: *Oil & Gas Science and Technology - Revue d'IFP Energie Nouvelles* 71.1 (2016), p. 2. DOI: 10.2516/ogst/2015021.

[87] J. Borée, S. Maurel, and R. Bazile. *Disruption of a compressed vortex*. In: *Physics of Fluids* 14.7 (2002), pp. 2543–2556. DOI: 10.1063/1.1472505.

[88] M. Fogleman et al. *Application of the proper orthogonal decomposition to datasets of internal combustion engine flows*. In: *Journal of Turbulence* 5 (2004), N23. DOI: 10.1088/1468-5248/5/1/023.

[89] S. Roudnitzky, P. Druault, and P. Guibert. *Proper orthogonal decomposition of in-cylinder engine flow into mean component, coherent structures and random Gaussian fluctuations*. In: *Journal of Turbulence* 7 (2006), N70. DOI: 10.1080/14685240600806264.

[90] B. Böhm, F. di Mare, and A. Dreizler. *Characterisation of cyclic variability in an optically accessible IC Engine by means of phase-independent POD*. In: *Proceedings of the LES4ICE International Conference*. IFP. 2010.

[91] Y. Cao et al. *Cluster-based analysis of cycle-to-cycle variations: Application to internal combustion engines*. In: *Experiments in Fluids* 55.11 (2014), pp. 1–8. DOI: 10.1007/s00348-014-1837-y.

[92] T. Wang et al. *An investigation into in-cylinder tumble flow characteristics with variable valve lift in a gasoline engine*. In: *Flow, Turbulence and Combustion* 94.2 (2015), pp. 285–304. DOI: 10.1007/s10494-014-9562-4.

[93] Johannes Bode. *Untersuchung der Zyklus-zu-Zyklus-Schwankungen in einem Ottomotor mit Hilfe mehrdimensionaler Strömunsdiagnostik*. PhD thesis. TU Darmstadt, 2017.

[94] P. Arányi et al. *Analysis of different POD methods for PIV-measurements in complex unsteady flows*. In: *International Journal of Heat and Fluid Flow* 43 (2013), pp. 204–211. DOI: 10.1016/j.ijheatfluidflow.2013.07.001.

[95] W. Juergens and H. Kaltenbach. *Eigenmode decomposition of turbulent velocity fields behind a swept, backward-facing step*. In: *Journal of Turbulence* 4 (2003), N18. DOI: 10.1088/1468-5248/4/1/018.

[96] F. di Mare and R. Knappstein. *Statistical analysis of the flow characteristics and cyclic variability using Proper Orthogonal Decomposition of highly resolved LES in internal combustion engines*. In: *Computers & Fluids* 105 (2014), pp. 101–112. DOI: 10.1016/j.compfluid.2014.09.019.

[97] P. Abraham et al. *Evaluating Large-Eddy Simulation (LES) and High-Speed Particle Image Velocimetry (PIV) with Phase-Invariant Proper Orthogonal Decomposition (POD)*. In: *Oil & Gas Science and Technology - Revue d'IFP Energie Nouvelles* 69.1 (2014), pp. 41–59. DOI: 10.4271/2013-01-0542.

[98] H. Chen et al. *A Practical Guide for Using Proper Orthogonal Decomposition in Engine Research*. In: *International Journal of Engine Research* 14.4 (2013), pp. 307–319. DOI: 10.1177/1468087412455748.

[99] H. Chen, D. Reuss, and V. Sick. *On the use and Interpretation of Proper Orthogonal Decomposition of In-Cylinder Engine Flows*. In: *Measurement Science and Technology* 23.8 (2012), p. 085302. DOI: 10.1088/0957-0233/23/8/085302.

[100] D. Block et al. *Prospects and limitations of conditional averaging*. In: *Physica Scripta* 2006.T122 (2006), p. 25. DOI: 10.1088/0031-8949/2006/T122/007.

[101] M. Köhler, D. Hess, and C. Brücker. *Flying PIV measurements in a 4-valve IC engine water analogue to characterize the near-wall flow evolution*. In: *Measurement Science and Technology* 26.12 (2015), p. 125302. DOI: 10.1088/0957-0233/26/12/125302.

[102] B. Peterson et al. *Assessment and application of tomographic PIV for the spray-induced flow in an IC engine*. In: *Proceedings of the Combustion Institute* 36.3 (2017), pp. 3467–3475.

[103] Peter Janas. *Large Eddy Simulation of In-Cylinder Phenomena in Spark Ignition Engine*. PhD thesis. Universität Duisburg-Essen, 2017.

[104] D. Wilcox. *Turbulence Modeling for CFD*. 2nd. DCW Industries, Inc., 1994.

[105] U. Piomelli. *Wall-layer models for large-eddy simulations*. In: *Progress in Aerospace Sciences* 44.6 (2008), pp. 437–446. DOI: 10.1016/j.paerosci.2008.06.001.

[106] S. Kawai and J. Larsson. *Wall-modeling in large eddy simulation: Length scales, grid resolution, and accuracy*. In: *Physics of Fluids* 24.1 (2012). DOI: 10.1063/1.3678331.

[107] C. Jainski et al. *High-speed micro particle image velocimetry studies of boundary-layer flows in a direct-injection engine*. In: *International Journal of Engine Research* 14.3 (2013), pp. 247–259. DOI: 10.1177/1468087412455746.

[108] M. Schmitt et al. *Investigation of wall heat transfer and thermal stratification under engine-relevant conditions using DNS*. In: *International Journal of Engine Research* 17.1 (2016), pp. 63–75. DOI: 10.1177/1468087415588710.

[109] Peter C. Ma et al. *Development and Analysis of Wall Models for Internal Combustion Engine Simulations Using High-speed Micro-PIV Measurements*. In: *Flow, Turbulence and Combustion* 98.1 (2017), pp. 283–309. DOI: 10.1007/s10494-016-9734-5.

[110] E. Baum et al. *Tomographic PIV measurements in an IC engine*. In: *16th international symposium on applications of laser techniques to fluid mechanics, Lisbon, Portugal*. 2012, pp. 09–12.

[111] E. Baum et al. *Investigation of the 3D flow field in an IC engine using tomographic PIV*. In: *Proceedings of the Combustion Institute* 34.2 (2013), pp. 2903 –2910. DOI: 10.1016/j.proci.2012.06.123.

[112] A. Morse, J. Whitelaw, and M. Yianneskis. *Turbulent flow measurements by Laser-Doppler anemometry in motored piston-cylier assemblies*. In: *J. Fluids Eng.* 101:2 (1979), pp. 208–216. DOI: 10.1115/1.3448937.

[113] M. Schmitt et al. *Direct numerical simulation of multiple cycles in a valve/piston assembly*. In: *Physics of Fluids* 26.3 (2014). DOI: 10.1063/1.4868279.

[114] *ANSYS CFX-Solver Theory Guide*. Release 18.0. ANSYS. 2017.

[115] M. Germano et al. *A dynamic subgrid-scale eddy viscosity model*. In: *Physics of Fluids* 3.7 (1991), pp. 1760–1765. DOI: 10.1063/1.857955.

[116] D. Lilly. *A proposed modification of the Germano subgrid-scale closure method*. In: *Physics of Fluids* 4.3 (1992), pp. 633–635. DOI: 10.1063/1.858280.

[117] H. Toda et al. *A Dynamic Procedure for Advanced Subgrid-Scale Models and Wall-Bounded Flow*. In: *7th International Symposium On Turbulence and Shear Flow Phenomena*. 2011.

[118] P. Spalart et al. *A new version of detached-eddy simulation, resistant to ambiguous grid densities*. In: *Theoretical and computational fluid dynamics* 20.3 (2006), pp. 181–195. DOI: 10.1007/s00162-006-0015-0.

[119] M. Shur et al. *A hybrid RANS-LES approach with delayed-DES and wall-modelled LES capabilities*. In: *International Journal of Heat and Fluid Flow* 29.6 (2008), pp. 1638–1649. DOI: 10.1016/j.ijheatfluidflow.2008.07.001.

[120] K. Hanjalić et al. *Merging LES and RANS strategies: Zonal or seamless coupling?* In: *Direct and Large-Eddy Simulation V*. Springer, 2004, pp. 451–464.

[121] S. Girimaji and K. Abdol-Hamid. *Partially averaged Navier-Stokes model for turbulence: Implementation and validation*. In: *AIAA paper* 502 (2005), p. 2005. DOI: 10.2514/6.2005-502.

[122] S. Girimaji. *Partially-averaged Navier-Stokes model for turbulence: A Reynolds-averaged Navier-Stokes to direct numerical simulation bridging method*. In: *Journal of Applied Mechanics* 73.3 (2006), pp. 413–421. DOI: 10.1115/1.2151207.

[123] J. Bin et al. *Partially-Averaged Navier-Stokes method with modified $k-\varepsilon$ model for cavitating flow around a marine propeller in a non-uniform wake*. In: *International Journal of Heat and Mass Transfer* 55.23-24 (2012), pp. 6582–6588. DOI: 10.1016/j.ijheatmasstransfer.2012.06.065.

[124] J. Rotta. *Turbulente Strömungen*. Universitätsverlag Göttingen, 2010.

[125] J. Smagorinsky. *General circulation experiments with the primitive equations: I. The basic experiment*. In: *Monthly weather review* 91.3 (1963), pp. 99–164.

[126] E. Van Driest and C. Blumer. *Boundary Layer Transition - free-stream Turbulence and Pressure Gradient Effects*. Tech. rep. 6. 1963, pp. 1303–1306. DOI: 10.2514/3.1784.

[127] F. Nicoud and F. Ducros. *Subgrid-Scale Stress Modelling Based on the Square of the Velocity Gradient Tensor*. In: *Flow, Turbulence and Combustion* 62.3 (1999), pp. 183–200. DOI: 10.1023/A:1009995426001.

[128] F. Nicoud et al. *Using singular values to build a subgrid-scale model for large eddy simulations*. In: *Physics of Fluids* 23.8 (2011). DOI: 10.1063/1.3623274.

[129] M. Rieth et al. *Comparison of the Sigma and Smagorinsky LES models for grid generated turbulence and a channel flow*. In: *Computers & Fluids* 99 (2014), pp. 172–181. DOI: 10.1016/j.compfluid.2014.04.018.

[130] A. Travin et al. *Physical and Numerical Upgrades in the Detached-Eddy Simulation of Complex Turbulent Flows*. In: *Advances in LES of Complex Flows*. Ed. by R. Friedrich and W. Rodi. Vol. 65. Fluid Mechanics and Its Applications. Springer, 2004, pp. 239–254. ISBN: 978-1-4020-0486-5. DOI: 10.1007/0-306-48383-1_16.

[131] F. Menter. *Two-equation eddy-viscosity turbulence models for engineering applications*. In: *AIAA journal* (1994), pp. 1598–1605.

[132] F. Menter and M. Kuntz. *The Aerodynamics of Heavy Vehicles: Trucks, Buses, and Trains*. In: ed. by Rose McCallen, Fred Browand, and James Ross. Berlin, Heidelberg: Springer Berlin Heidelberg, 2004. Chap. Adaptation of Eddy-Viscosity Turbulence Models to Unsteady Separated Flow Behind Vehicles, pp. 339–352. DOI: 10.1007/978-3-540-44419-0_30.

[133] F. Menter and Y. Egorov. *The Scale-Adaptive Simulation Method for Unsteady Turbulent Flow Predictions. Part 1: Theory and Model Description*. In: *Flow, Turbulence and Combustion* 85.1 (2010), pp. 113–138. DOI: 10.1007/s10494-010-9264-5.

[134] Y. Egorov et al. *The Scale-Adaptive Simulation Method for Unsteady Turbulent Flow Predictions. Part 2: Application to Complex Flows*. In: *Flow, Turbulence and Combustion* 85 (2010), pp. 139–165. DOI: 10.1007/s10494-010-9265-4.

[135] P. Schaefer et al. *Testing of Model Equations for the Mean Dissipation using Kolmogorov Flows*. In: *Flow Turbulence and Combustion* 85.2 (2010), pp. 225–243. DOI: 10.1007/s10494-010-9273-4.

[136] A. Lucius and G. Brenner. *Unsteady CFD simulations of a pump in part load conditions using scale-adaptive simulation*. In: *International Journal of Heat and Fluid Flow* 31 (2010), pp. 1113–1118. DOI: 10.1016/j.ijheatfluidflow.2010.06.005.

[137] S. Buhl, F. Hartmann, and C. Hasse. *Identification of Large-Scale Structure Fluctuations in IC Engines using POD-Based Conditional Averaging*. In: *Oil & Gas Science and Technology - Revue d'IFP Energie Nouvelles* 71.1 (2016), p. 1. DOI: 10.2516/ogst/2015021.

[138] S. Buhl et al. *A Combined Numerical and Experimental Study of the 3D Tumble Structure and Piston Boundary Layer Development During the Intake Stroke of a Gasoline Engine*. In: *Flow, Turbulence and Combustion* 98.2 (2016), pp. 579–600. DOI: 10.1007/s10494-016-9754-1.

[139] G. Raithby and G. Schneider. *Numerical solution of problems in incompressible fluid flow: Treatment of the velocity-pressure coupling*. In: *Numerical Heat Transfer, Part A: Applications* 2.4 (1979), pp. 417–440. DOI: 10.1080/10407787908913423.

[140] J. van Doormaal and G. Raithby. *Enhancement of the SIMPLE method for predicting incompressible fluid flow*. In: *Numer. Heat Transfer* 7.2 (1984), pp. 147–163. DOI: 10.1080/01495728408961817.

[141] M. Raw. *Robustness of coupled algebraic multigrid for the Navier-Stokes equations*. In: *AIAA paper* 96 (1996), p. 0297. DOI: 10.2514/6.1996-297.

[142] C. Rhie and W. Chow. *Numerical study of the turbulent flow past an airfoil with trailing edge separation*. In: *AIAA journal* 21.11 (1983), pp. 1525–1532. DOI: 10.2514/3.8284.

[143] *IC Engine Simulations with ANSYS CFX and ANSYS ICEM CFD*. Release 14.0. ANSYS. 2012.

[144] S. Buhl et al. *A comparative study of intake and exhaust port modeling strategies for scale-resolving engine simulations*. In: *IJER* 11.1 (2017). DOI: 10.1177/1468087417707452.

[145] L. Davidson. *Using Isotropic Synthetic Fluctuations as Inlet Boundary Conditions for Unsteady Simulations*. In: *Advances and Applications in Fluid Mechanics* 1 (2007), pp. 1–35.

[146] M. Schmitt et al. *Investigation of cycle-to-cycle variations in an engine-like geometry*. In: *Physics of Fluids* 26.12 (2014), p. 125104. DOI: 10.1063/1.4903930.

[147] M. Schmitt et al. *Direct numerical simulation of the effect of compression on the flow, temperature and composition under engine-like conditions*. In: *Proceedings of the Combustion Institute* 35.3 (2015), pp. 3069–3077. DOI: 10.1016/j.proci.2014.06.097.

[148] J. Lumley and G. Newman. *The return to isotropy of homogeneous turbulence*. In: *Journal of Fluid Mechanics* 82.1 (1977), pp. 161–178. DOI: 10.1017/S0022112077000585.

[149] S. Buhl et al. *Comparative Study of Turbulence Models for Scale-Resolving Simulations of Internal Combustion Engine Flows*. In: *Computers & Fluids* 156 (2017), pp. 66–80. DOI: 10.1016/j.compfluid.2017.06.023.

[150] L. Graftieaux, M. Michard, and N. Grosjean. *Combining PIV, POD and vortex identification algorithms for the study of unsteady turbulent swirling flows*. In: *Measurement Science and Technology* 12.9 (2001), p. 1422.

[151] S. Buhl et al. *Investigation of an IC Engine Intake Flow Based on Highly Resolved LES and PIV*. In: *Oil & Gas Science and Technology - Revue d'IFP Energie Nouvelles* 72.3 (2017), p. 15. DOI: 10.2516/ogst/2017012.

[152] A. Chatterjee. *An introduction to the proper orthogonal decomposition*. In: *Current Science* 78.7 (2000), pp. 808–817.

[153] V. Sick et al. *A Common Engine Platform for Engine LES Development and Validation*. In: *International Conference on Large-Eddy Simulation for Internal Combustion Engine Flows (LES4ICE), Rueil-Maimaison, France, November*. 2010, pp. 18–19.

[154] J. Hunt, A. Wray, and P. Moin. *Eddies, streams, and convergence zones in turbulent flows*. Tech. rep. NASA, 1988.

[155] L. Davidson. *Evaluation of the SST-SAS model: channel flow, asymmetric diffuser and axi-symmetric hill*. In: *ECCOMAS CFD 2006: Proceedings of the European Conference on Computational Fluid Dynamics, Egmond aan Zee, The Netherlands, September 5-8, 2006*. Delft University of Technology; European Community on Computational Methods in Applied Sciences (ECCOMAS). 2006.

[156] M. Michard and T. Favelier. *Développement d'un critère d'identification de structures tourbillonnaires adapté aux mesures de vitesse par PIV*. In: *9ème Congrès Francophone de Vélocimétrie Laser*. 2004, pp. 14–17.

[157] M. Gohlke et al. *Thorough analysis of vortical structures in the flow around a yawed bluff body*. In: *Journal of Turbulence* 9 (2008), N15. DOI: 10.1080/14685240802010657.

[158] A. Berson, M. Michard, and P. Blanc-Benon. *Vortex identification and tracking in unsteady flows*. In: *Comptes Rendus Mécanique* 337.2 (2009), pp. 61–67. DOI: 10.1016/j.crme.2009.03.006.